Miguel António Felizardo da Costa

Mestre

Advanced Instrumentation for Superheated Liquid Detectors in Dark Matter Searches

Dissertação para obtenção do Grau de Doutor em
Engenharia Física

Orientador: Doutor Thomas Abbott Girard
Co-orientador: Doutora Maria Adelaide de Almeida Pedro de Jesus

Júri:

Presidente: Prof. Doutor Fernando Jorge da Silva Pina

Arguentes: Prof. Doutora Maria Isabel Silva Ferreira Lopes
Prof. Doutor Sérgio Eduardo de Campos Costa Ramos

Vogais: Prof. Doutora Maria Adelaide de Almeida Pedro de Jesus
Prof. Doutor José Joaquim Gonçalves Marques
Prof. Doutor Thomas Abbott Girard

**FCt FACULDADE DE CIÊNCIAS E TECNOLOGIA
UNIVERSIDADE NOVA DE LISBOA**

Janeiro 2013

Title: Advanced Instrumentation for Superheated Liquid Detectors in Dark Matter Searches
Name: Miguel António Felizardo da Costa
Faculdade de Ciências e Tecnologia e a Universidade Nova de Lisboa

Copyright

ACKNOWLEDGEMENTS

Title: Advanced Instrumentation for Superheated Liquid Detectors in Dark Matter Searches
Name: Miguel António Felizardo da Costa
Dissertation for doctoral in Physics Engineering
Supervisor: Doctor Thomas Abbott Girard
Co-Supervisor: Doctor Maria Adelaide de Almeida Pedro de Jesus

ABSTRACT

The initial goal of the thesis work was to improve the performance of the instrumentation used in the SIMPLE dark matter search. Consequently, the ultimate objective is to find a possible candidate for Dark Matter or improve the knowledge of its nature. Upon a brief description of Dark Matter and the status of its search, the fundamentals of Superheated Liquid Detectors are presented.

This thesis presents a robust acoustic instrumentation together with a new method for the identification of bubble nucleations in Superheated Droplet Detectors. This is accomplished through straightforward signal processing techniques applied to the acoustical recording of the nucleation events, which consists of pulse shape identification procedures. A set of tests are presented to evaluate the performance of the proposed algorithms, as well as the new and more reliable instrumentation. An effort to locate a bubble nucleation in the SDDs is accomplished through some elaborated signal processing techniques applied to the acoustical recording of the nucleation events. These include the application of wavelets, the chirp-z transform and pulse shape identification procedures to locate temporally and validate the nucleation for its spatial localization. Acoustic and SDD associated backgrounds are completely discriminated with the developed signal processing techniques.

Results from systematic studies are presented for the instrumentation and SDD response, which are used in the SIMPLE dark matter search experiment and possibly in neutron dosimetry.

A new bubble nucleation efficiency is drawn out, together with particle discrimination confirmation determined throughout α-n calibrations.

SIMPLE's Phase-II Dark Matter results are presented with the implementation of the complete instrumentation in operation for SDDs. These results are simultaneously presented with the full characterization of the local background scenario and gained knowledge of SDD characteristics and dynamics. Interpretations of these results are laid out.

The direct future is given through the R&D of a rejuvenation superheated liquid detector, the Big Droplet Chamber. A prototype of this new Bubble Chamber is shown together with its first results of a more prevailing ultrasound acoustic system. Which can possibly reveal in the near future, unseen aspects such as the bubble formation stage in superheated liquids up to now.

Key-words: Instrumentation, Superheated Liquid Detectors, Nucleation, Discrimination, Dark Matter

Título: Advanced Instrumentation for Superheated Liquid Detectors in Dark Matter Searches
Nome: Miguel António Felizardo da Costa
Dissertação de Doutoramento em Engenharia Física
Orientador: Doutor Thomas Abbott Girard
Co-Orientador: Doutora Maria Adelaide de Almeida Pedro de Jesus

RESUMO

O objectivo inicial da tese é o de melhorar o desempenho da instrumentação da experiência SIMPLE existente de procura de matéria escura. Consequentemente, o objectivo final é encontrar um possível candidato para a matéria escura ou melhorar o conhecimento da sua natureza. Após uma breve descrição da matéria escura e o status da sua pesquisa, os fundamentos dos detectores de líquidos superaquecidos são apresentados.

Esta tese apresenta uma robusta instrumentação acústica, juntamente com um novo método de identificação de nucleações em Detectores de Gotículas Sobreaquecidas. Isto é realizado através de técnicas de processamento de sinal aplicadas aos eventos de nucleações adquiridos acusticamente, que consistem em procedimentos de identificação da forma do impulso. Uma panóplia de testes são apresentados para avaliar o desempenho dos algoritmos apresentados, bem como a fiabilidade da nova instrumentação desenvolvida. Um esforço para localizar uma nucleação nestes detectores é realizada através de técnicas elaboradas de processamento de sinal aplicadas à gravação acústica das nucleações. Dentro destas técnicas são aplicadas as ondulas, a transformada chirp-z e a identificação da forma do pulso para localizar temporariamente e validar a nucleação, para a sua localização espacial. O ruído acústico de fundo e dos próprios detectores são totalmente discriminados com as técnicas de processamento de sinal desenvolvidos.

São apresentados resultados de estudos sistemáticos para a instrumentação e para a resposta dos detectores, que são utilizados na experiência de pesquisa da matéria escura e possivelmente em dosimetria de neutrões.

Uma nova eficiência de nucleação das bolhas é mostrada e a discriminação de partículas é determinada e confirmada durante calibrações α-n.

Os resultados da Fase II do SIMPLE para a busca da matéria escura são apresentados com a total implementação da instrumentação posta em ação para os SDD e, simultaneamente, com a total caracterização de todo o ruído de fundo local com todo o conhecimento dos SDDs já obtidos. As interpretações destes resultados são definidos.

O futuro próximo é dado através do desenvolvimento de um detector de líquido superaquecido rejuvenecido, a câmara de bolha SIMPLE. Um protótipo desta nova câmara de bolha é mostrado em conjunto com os seus primeiros resultados de um sistema de ultra-som acusticamente mais prevalecente. Esta abordagem pode num futuro próximo revelar aspectos dos líquidos superaquecidos que até agora, têm permanecido invisíveis.

Temas-chave: Instrumentação, Detectores de Liquidos Superaquecidos, Nucleação, Descriminação, Matéria Escura

x

List of Figures

_____

List of Tables

_____

_____

- A - amplitude

- $a_{p,n}$ - effective couplings of WIMP-proton and WIMP-neutron interaction

- B - gel bulk modulus

- C - capacitance

- d - distance

- Ω_{DM} - DM mass density

- $\rho(r)$ - local halo mass density

- ρ_V - vapour density

- LET - linear energy transfer

- E_m - minimum energy required for bubble formation

- E_{wall} - kinetic energy imparted to the liquid by the motion of the vapour wall

- $E_{thr,}$ - threshold energy, for WIMP recoils

- dR/dE - rate per unit target mass and recoil energy

- ψ - thermodynamic factor

- $\varepsilon(E)$ - detection efficiency

- F - energy imparted to the liquid during the growth of the bubble by viscous forces

- FFT - Fast Fourier Transform

- f(v) - halo velocity distribution relative to the detector

- $f_{p,n}$ - effective couplings to protons and neutrons

- GF - Fermi coupling constant

- GCC - generalized cross-correlation

- h - Hubble constant

- H - vaporization energy

- $|H(x(t))|$ - Hilbert transform

- h_{fg} - latent heat of vaporisation

- $\gamma(T)$ - surface tension of the liquid at temperature

- J - total angular momentum of the nucleus

- k - wave number

- L - length

- MACHO - Massive Astrophysical Compact Halo Object

- M_w - WIMP mass

- M(r) - mass inside the orbit

- Λ - nucleation parameter of the refrigerant

- η - bubble nucleation efficiency

- P - pressure
- P_w - power
- PSD - Power Spectral Density
- Q - charge
- r_c - critical radius
- *r* - radius
- S - reduced superheat
- $S_{p,n}$ - expectation values for the spin content for protons and neutrons in the nucleus
- σ - zero momentum transfer cross section
- T - temperature
- T_b -boiling temperature
- T_c - critical temperature
- τ - decay time constant
- *t* - time
- TDOA - time delays of arrival
- *v* - velocity
- v_{gel} - sound velocity in the gel
- V - Voltage
- v_{min} - minimum velocity an incident WIMP needs to have in order to produce a recoil of energy
- v_{max} - local galactic escape velocity relative to the detector (maximum WIMP velocity in the halo)
- W - work
- Z - number of protons

Chapter 1   Introduction

_____

The composition of the Universe is one of the most challenging issues facing modern physics, given that no understandable answer of what the Universe is made of is yet clear. Twenty three percent of "missing" Universe is a bit too much to be left unknown. A competitive hunt is underway to discover the composition of dark matter, a large part of which is devoted to its direct detection through interactions with detectors in underground laboratories.

One of these direct detection experiments is SIMPLE (Superheated Instrument for Massive ParticLe Experiments). SIMPLE is located 500 m below ground in the Laboratoire Souterrain à Bas Bruit (LSBB) in southern France. It utilizes superheated liquid detectors and in 2005, SIMPLE completed its Phase I, reporting results [1] from a four detector array, which – apart from setting the benchmark in such searches for the superheated liquid technique at the time, identified several areas requiring a significant improvement, not the least of which was its instrumentation.

The instrumentation of all superheated liquid efforts is mainly acoustic. This dissertation describes the R&D of an advanced, microphone-based, SIMPLE acoustic instrumentation, and its implementation in a Phase II search for evidence of a particle dark matter. The majority of the R&D activity for the instrumentation was carried-out at Instituto Tecnológico e Nuclear (ITN), following the SIMPLE Phase II measurements at LSBB, conducted in two Stages: Stage 1 between 27 October 2009 – 5 February 2010 and, Stage 2 between 12 April - 22 July 2010.

Chapter 2 provides a brief description of the Dark Matter scenario; Chapter 3, the Superheated Liquid Detectors involved. The development and testing of the new acoustic instrumentation, based at ITN near Lisbon, is presented in Chapter 4 and includes a new method for the identification (pulse shape identification procedures) of a bubble nucleation in superheated droplet detectors, and a description on a way of localizing the bubble nucleation in the detectors. Chapter 5 reviews observations of the SDD response using the instrumentation with regard to various production and intrinsic noise issues. The following chapter, 6, presents the SDD sensitivities, as well as particle discrimination through alpha and neutron calibrations.

Chapter 7 describes the implementation of the new instrumentation in Phase II of the SIMPLE Dark Matter search experiment. The results of the search measurements are shown in Chapter 8, together with the interpretations of these results in both spin-dependent and spin-independent sectors.

Chapter 9 describes the new direction for SIMPLE based on these results, and the design and implementation of a "Big Droplet Chamber", in particular preliminary tests of a new high frequency instrumentation.

The final Chapter 10 summarizes the conclusions of this thesis. In the course of the research, many new questions emerged as the original ones were being answered: some of these ideas for future research and development, proposals and experiments to be performed, are included.

In the course of my PhD many issues were addressed that were not part of the thesis work *per se,* but are considerably valuable, for instance: logistics and entrepreneurship*.*

Chapter 2   Dark Matter

_____

2.1 Evidence of Dark Matter

The evidence of Dark Matter (DM) has been established and recognized [2,3]. The oldest evidence for the existence of DM comes from the measurement of galactic rotation curves. The rotational velocity v of an object on a stable orbit with radius r around a galaxy scales as $v(r) \propto \sqrt{M(r)/r}$, where $M(r)$ is the mass inside the orbit. If the radius lies outside the visible part of the galaxy, $v(r) \propto 1/\sqrt{r}$. In most of the observed galaxies, v tends to become constant for the largest values of r where the rotation curve can be determined.

The main explanation is the existence of a non-luminous halo, with mass density $\rho(r) \propto 1/r^2$, at some point the mass will be proportional to the radius implying a decrease in mass density in order to keep the total mass of the galaxy finite. This leads to a lower level on the DM mass density, $\Omega_{DM} \geq 0.1$, where $\Omega_X \equiv \rho_X / \rho_{critical}$, $\rho_{critical}$ being the critical mass density, so $[\Omega_{total} = 1]$ corresponds basically to a flat Universe. With the observation of such clusters of galaxies the tendency is to have larger values, $\Omega_{DM} \approx 0.2$.

To date, the most accurate determination of Ω_{DM} comes from global fits of cosmological parameters to a variety of observations, including measurements of the anisotropy of the cosmic microwave background (CMB) and of the spatial distribution of galaxies. The density of cold, non-baryonic matter is found to be:

$$\Omega_{nbm} h^2 = 0.112 \pm 0.006 ,$$

(1.1)

where h is the Hubble constant.

The baryonic matter density,

$$\Omega_{bm} h^2 = 0.022 \pm 0.001 ,$$

(1.2)

may contribute to (baryonic) DM, like MACHOs [4] or gas clouds [5].

Nowadays, detailed measurements of anisotropies in the CMB radiation, galactic lenses and comparisons of large scale structures with simulation of the structure development of the universe, when combined into a standard cosmological model, have suggested a universe composed of 4% of ordinary matter, 1% associated with electrons, neutrinos and photons, about 23% of DM, and 72% of Dark Energy (DE).

2.2 Possible Candidates

Analyses of the Universe and its structure formation indicate that most DM should be cold (slow moving) and should have been non-relativistic during formation of the galaxy [2]. This agrees well with the contribution of light neutrinos to Eq. (1.1),

$$\Omega_\nu h^2 \leq 0.0062 \qquad 95\% \, CL \qquad (1.3)$$

Candidates for non-baryonic DM in Eq. (1.1) must satisfy several conditions: first, they must be stable on cosmological time scales (otherwise they would have decayed by now or at least have a lifetime long compared to the present age of the universe), they must interact very weakly with electromagnetic radiation, and they must have the correct relic density. Numerous candidates have been proposed; some of the more prominent candidates include MACHOs, axions, neutrinos, neutralinos and weakly interacting massive particles (WIMPs).

These candidates in principle will be detectable with present or near-future technology. But there are also particle physics DM candidates which currently seem almost impossible to detect, unless they decay. These include the gravitino and the axino, to give two examples.

2.2.1 MACHOs

One of the simplest candidates for dark matter is a Massive Astrophysical Compact Halo Object (MACHO). MACHOs are objects that not directly observed, are made of ordinary matter. These could be compact objects such as cold white dwarfs or black holes. Astronomical searches have found such objects through microlensing, but the total amount of these objects is not enough to make up all of the missing matter [5].

2.2.2 Neutrinos

An experimentally verified dark matter candidate is the neutrino [2,5]. Neutrinos have been considered excellent dark matter candidates because it is proved that neutrinos have small but non-zero masses by neutrino oscillation detection, as seen from Eq. (1.3). However, neutrinos are relativistic particles which large scale structure constrains to make up only a few percent of the total non-ordinary dark matter. Hence, neutrinos cannot be a major constituent of the halo dark matter.

2.2.3 Axions

These hypothetical light pseudo-scalar particles have often been discussed as DM candidates. Laboratory experiments [6] limit axions to be very light (taking account all recognized uncertainties one arrives at a plausible range for the mass of dark-matter axions between a few μeV and a few meV) and to have an extremely small coupling to ordinary matter and therefore an

extremely long lifetime (many orders of magnitude larger than the age of the Universe). Axions that would have been produced in the Big Bang were never in thermal equilibrium and were always non-relativistic (i.e. they are "cold" Dark Matter). The calculation of axion relic density depends on the assumption made regarding the production mechanism. Nevertheless it is possible to find in the range mentioned above, where axions satisfy all present constraints to represent a possible Dark Matter candidate.

2.2.4 Neutralinos

The Neutralino is a high-quality dark matter candidate in the framework of the Supersymmetry theory.

Supersymmetry (SUSY) was proposed as an expansion of the particle physics standard model to combine the four fundamental forces of nature (electromagnetic, weak, strong and gravitational). Each standard model particle has a superpartner in SUSY, which differ by half a unit of spin. The neutralino is the lightest Supersymmetric particles (LSP), which is stable in SUSY models where R parity (R-parity conservation implies that LSP cannot decay) is conserved.

There is a large parameter space left to be probed by current technologies. The Neutralino is one the most well-liked dark matter candidates that is explored by on-going direct detection experiments via its elastic scattering from a nucleon of the detector material. Indirect Neutralino searches, via their annihilation products, such as high energy neutrinos, antiprotons, positrons and gamma rays are also pursued.

Although particle physics experiments place some constrains on the SUSY parameter space, a clear signal from a laboratory discovery of a dark matter particle will significantly constrain the mechanisms, the calculation of the relic density and the Neutralino candidates in the MSSM (Minimal Supersymmetric Model).

The lightest Supersymmetric particle (LSP) can be referred in the context of cold dark matter as a WIMP, or Weakly Interacting Massive Particle, which refers to a general class of unidentified particles postulated by Supersymmetry. By definition, they interact only via the weak interaction and gravity.

2.2.5 WIMPs

WIMPs are particles with mass roughly between a few GeV and a few TeV, and with weak cross sections of approximately the same strength.

The WIMP mean velocity is expected to be a few hundred kms^{-1}. As such, WIMPs interact with ordinary matter through elastic scattering on nuclei and so with the expected WIMP masses varying in the range mentioned above, the typical nuclear recoil energies are of order of 1 to 100 keV.

Hence, the expected interaction rate depends on two quantities: the mass and cross section of the WIMP. The cross section depends on the nature of the couplings.

The calculated event rates are lower than common radioactive backgrounds, on the order of << 1 event per kilogram of detector per day. This implies the need for additional protection against induce cosmic rays backgrounds, thus all projects "hide" themselves in underground laboratories. The sensitivity (of any detector) is best for WIMP masses near the mass of the recoiling nucleus.

2.3 Dark Matter Detection

The interaction of a WIMP with the detector material can be either elastic or inelastic, and either spin-dependent or spin-independent.

- Elastic and inelastic scattering: Elastic scattering involves the interaction of a WIMP with the nucleus as a whole, causing the nucleus to recoil. In inelastic scattering all of the energy does not go into nuclear recoil; instead the nucleus is excited to a higher energy state which then decays by photon emission.

- Spin-dependent and spin-independent scattering: Spin-dependent (axial-vector) scattering results from the coupling of a WIMP's spin with the spin of a nucleon. Spin-independent (scalar) does not depend on spin, and has the advantage of higher cross sections with larger nuclei (because of coherence where the WIMP interacts with the nucleus as a whole, scaling as A^2).

Energy lost by a recoiling nucleus is converted to electrons, photons, phonons, and ion pairs. The detection of DM can be summarized in three forms:

- Phonon/Thermal: A vibration (detected as a rise in temperature) in the crystal lattice of the detector, caused by the slight movement of a nucleus which has recoiled. An extremely sensitive temperature system is located around the detector, allowing any temperature variation to be recorded.

- Ionization: A recoil nucleus gives an electron in the detector enough energy to escape its nucleus. A small electric field is set up in the detector to push the new charge to a detector wall where it can be registered as an ionization event.

- Scintillation: Occurs when an electron absorbs enough energy from a recoil event to reach to a higher energy state. After a short time, the electron will lose this energy by emitting a photon, which is then recorded by photomultipliers and converted to an electric signal for analysis.

2.3.1 Direct Detection

The majority of present experiments use these detector technologies:

- Scintillation: (DAMA/LIBRA[7], KIMS[8])
- Cryogenic: (CDMS[9], EDELWEISS [10], CRESST[11])
- Ionization: (CoGeNT[12])
- Noble Liquids: (XENON[13], ZEPLIN[14])
- Superheated Liquids: (COUPP[15], PICASSO[16], SIMPLE[17])

In general detecting only one of these channels is insufficient for particle discrimination. Hence, the majority of experiments use the detection of two of these channels permitting a discrimination between recoil and background particle interaction.

The DAMA collaboration has reported results from a total of 6 years exposure, with its new phase called LIBRA involving 250 kg of detectors. With addition of their earlier exposure of the original DAMA/NaI experiment with 100 kg of detectors [18], the total exposure sums up to 1.17 ton.year. They observe an annual modulation of the signal in the 2 to 6 keVee bin,), at 8.9 sigma level. If interpreted within the standard halo model, a couple of possible explanations have been considered: a WIMP with $m_\chi \sim 50$ GeV and $\sigma_{\chi p} \sim 7 \cdot 10^{-6}$ pb, or at low WIMP mass region, between 6 to 10 GeV with $\sigma_{\chi p} \sim 10^{-3}$ pb.

The KIMS Collaboration [8], is an experiment operating 12 crystals of CsI(Tl) with a total mass of 104.4 kg in the Yang Yang laboratory in Korea. It has been running several years of continuous operation and data acquisition. They should soon be able to confirm or not the DAMA value at 3 sigma. They have recently presented a new result at TAUP 2011 [19].

At low temperature in the orders of mK, the simultaneous measurement of the ionization and phonon signals in semiconductor detectors permits event discrimination between nuclear and electronic recoils down to 5 to 10 keV recoil energy.

At the Soudan Underground Laboratory, the CoGeNT collaboration [12] has operated a 440 g Germanium detector with an effective threshold of 400 eV for ~60 days [20]. After analysing the physics data and removing the surface interactions known from incomplete charge events, the result was an excess of events from the spectrum below 4 keV, agreeable with a low mass WIMP in the range of 7 to 11 GeV, and a cross section around 10^{-4} pb.

CDMS, after operating 19 Germanium cryogenic detectors at the Soudan mine with a total exposure of ~ 600 kg.d (~ 300 kg.d fiducial) [21] presented two events in the defined signal region, while only 0.9 background events were expected. No observation of a signal was claimed. The combined data from this run and previous provided an improved upper limit on the spin-independent cross section at 70 GeV/c^2 WIMP on a nucleon of 3.8×10^{-8} pb, with a 90% CL.

EDELWEISS has operated for one year ten Germanium detectors with 400 g each and are equipped with different thermal sensors, at the Laboratoire Souterrain de Modane [22]. A total of 5 events were observed in the signal region for a fiducial exposure of 384 kg.d, while 3 events were expected from backgrounds. No WIMP signal was claimed.

Having similar sensitivities, CDMS and EDELWEISS combined their data sets. This merging resulted in a gain of 1.6 relative to the best limit for WIMPs at masses larger than 700 GeV, and an improved limit of 3.3×10^{-8} pb for a 90 GeV WIMP mass [23].

The cryogenic experiment CRESST uses the scintillation of $CaWO_4$ as second variable for background discrimination. CRESST has recently presented a result [24] of the analysis of 730 kg.day exposure performed with 8 detectors. The observation of 67 events in the signal region is above the 40 expected background events. The event excess has been considered compatible with WIMPs.

The XENON collaboration [13] has operated the 161 kg XENON100 setup at Gran Sasso laboratory during a 100 day data acquiring. This resulted in a fiducial mass of 48 kg, originating 3 events observed in the signal region, while only 1.8 were expected, out of which 1.2 originate from contamination of Krypton 85 in the liquid [25]. This has allowed to set the best limits at all masses on spin-independent interactions of WIMPs, with a minimum of cross section at 7.0×10^{-9} pb for a mass of 50 GeV.

ZEPLIN III [26], with an active mass of 12 kg of Xenon, operated in the Boulby mine, was upgraded for a lower background, acquiring new data, and is now unfortunately finished. It delivered competitive limits and pioneered the use of a high electric fields to improve the electron-nuclear recoil discrimination.

The detectors using ^{19}F nuclei setting limits mainly on the spin dependent sector of WIMPs are: the bubble chamber like detector, from COUPP [15], that provided a new limit [27] for spin dependent proton coupling WIMPs for masses above 20 GeV, PICASSO [16], a superheated droplet detector run at SNOLAB, obtained a better limit below 20 GeV on the same type of WIMPs [28], and SIMPLE [17], running in France at the Laboratoire Souterrain à Bas Bruit, that has provided the currently best limit on the spin-dependent WIMP-proton cross section for all WIMP masses [29].

There is also the possibility of dark matter production in accelerators. Producing and detecting dark matter particles in an accelerator would be a huge step toward confirming the existence of dark matter, although direct detection has to be confirmed. Attempts in the near future should confirm if this is feasible or not.

2.3.2 Indirect Detection

WIMPs are capable of annihilation, and their products: neutrinos, gamma rays, positrons, etc, can be detected. Indirect measurements complement the direct detections, and are able to reach higher masses and different coupling interactions.

WIMPs can be slowed down, captured, and can stay in celestial objects such as planets or stars, thus enhancing their density and their annihilation probability. This is a source of muon

neutrinos which can interact in the Earth. These muons can then be detected in large neutrino telescopes such as, SuperKamiokande [30], AMANDA [31], ANTARES [32], and the large sensitive area of IceCube [33]. The best limit comes from muons with energy above ~2 GeV from SuperKamiokande. For slightly more energetic muons, the most stringent limit has been set by IceCube.

2.4 Challenges of Direct Dark Matter Searches

There are several difficulties associated with dark matter search experiments:

- Logistics.
- Radioactive contamination from the detector itself.
- The cross section is very small: $<10^{-6}$ pb, implying the need for large mass, sensitive detector material.
- The expected recoil energy of nucleus is also very small: 10 ~ 100 keV.
- The background rate due to neutrons, alpha-particles, gamma-rays, cosmic-rays, etc is much larger than the expected WIMP rate. This implies the need for an underground laboratory and careful selection of shielding and detector material and particle discrimination by the detector in an event-by-event basis.

Direct detection experiments typically operate in deep underground laboratories to reduce the background from cosmic rays. These include: the Laboratoire Souterrain a Bas Bruit, Rustrel (France); the Soudan mine (USA); the SNOLAB underground laboratory at Sudbury, Ontario (Canada); the Gran Sasso National Laboratory (Italy); the Boulby Underground Laboratory (UK); and the Deep Underground Science and Engineering Laboratory (USA), to name a few.

Chapter 3   Superheated Liquids

_____

3.1 Scope

The SIMPLE experiment is based on the use of superheated liquids, mainly Superheated Droplet Detectors (SDDs), in which an interaction of radiation generates the phase transition of a superheated liquid droplet, producing a detectable bubble.

A fluid is superheated when it is in liquid form at temperature and pressure values corresponding to the vapour region in its phase diagram. This metastable state is fragile and short-lived due to the high number of microscopic particles and/or gas pockets normally present at the interface with container surfaces. These act as seeds for the phase transitions and are called "heterogeneous" nucleation sites.

In order to achieve a steady state, the liquid must be moderately superheated, i.e., possess a relatively small difference between its operating temperature and boiling point. Halocarbons with a moderate degree of superheating can be used for particle detection since they are nucleated by energetic heavy ions, such as those produced by fast neutrons [34]. Halocarbons operated near their boiling point can be used in the detection of minimum ionising radiations, such as photons and electrons [35,36].

Two types of detectors utilize this technique; the Superheated Droplet Detector (SDD) and the Bubble Chamber (BC).

3.2 Superheated Liquid Physics

Radiation-induced nucleation is explained within the framework of the Seitz "thermal spike" model [37], which states that when a heavy charged particle slows down in moving through a liquid, kinetic energy is transferred as thermal energy to extremely small regions (as temperature spikes). The intense heating induces localized boiling, creating trails of sub microscopic vapour seeds of different sizes. Only a vapour seed which reaches critical size will grow into a macroscopic observable vapour bubble. Although the process is extremely complex, involving aspects of atomic and nuclear physics as well as fluid thermodynamics, in Seitz's approach these are avoided under the assumption of a static, equilibrium phase transition of the superheated fluid.

Following the Seitz's model, the minimum work (W) required to create a spherical bubble of radius r from classic thermodynamics [38] is:

$$W = 4\pi r^2 \gamma(T) - \frac{4}{3}\pi r^3 \Delta P ,$$

(3.1)

where $\gamma(T)$ is the surface tension of the liquid at temperature T; ΔP is the difference between the equilibrium vapour pressure and the externally applied pressure.

The minimum work increases with the size of the bubble, reaching a maximum and then decreasing. The maximum constitutes an energy barrier, which must be overcome in order for bubble nucleation to occur. The bubble radius corresponding to this maximum is called the critical radius (r_c) and is given by:

$$r_c = 2\gamma(T) \Big/ \Delta P ,$$

(3.2)

Substituting equation (3.2) into equation (3.1) the minimum reversible work needed to form a critical size bubble is then:

$$W = \left(16\pi \Big/ 3\right)\left(\gamma^3(T) \Big/ (\Delta P)^2\right).$$

(3.3)

This equation implies that as the temperature increases, W decreases and less energy is required for vapour nucleation. When dissipative forces are considered (viscosity, etc.), the minimum energy E_m required for bubble formation is given by [39]:

$$E_m = W + H + E_{wall} + F ,$$

(3.4)

where H is the vaporization energy, E_{wall} is the kinetic energy imparted to the liquid by the motion of the vapour wall and F is the energy imparted to the liquid during the growth of the bubble by viscous forces. H is given by:

$$H = \frac{4}{3}\pi r_c^3 \rho_v h_{fg},$$

(3.5)

where ρ_V is the vapour density and h_{fg} the latent heat of vaporisation.

Radiation-induced thermodynamics is a dynamic process involving the fluid thermodynamics of the growth of the bubble. This is not included in the static equilibrium thermodynamic approach and therefore the Seitz model does not provide a complete description. An attempt at a complete dynamical model for bubble nucleation in a superheated liquid by ionising radiation was proposed using a numerical technique [40]. However, the required amount of computational time prohibits its general use; models [41] and even semi-empirical approaches [42] to understand the mechanism are used for practical purposes.

In the case of neutrons, the energy deposition occurs through the secondary ionising particles produced during interaction with the nuclei of the liquid. When a neutron of energy E_n interacts with a nucleus of atomic weight A, the maximum kinetic energy that can be transferred to the nucleus from the neutron is through an elastic head-on collision and is given by:

$$E_A = \frac{4A}{(A+1)^2} E_n .$$

(3.6)

The minimum energy to produce a bubble event will be:

$$E_c = W\left(1 + \frac{\rho_v h_{fg}}{\Delta P}\right). \tag{3.7}$$

After receiving the energy, the nucleus is scattered and moves through the liquid losing its energy via Coulombic interactions until it comes to rest. For a given neutron energy, different nuclei of the liquid will receive different amounts of energy, depending on their atomic weight. The ion with the highest value of linear energy transfer (LET) or (dE/dx) in the liquid will play the major role in vapour nucleation. The energy deposited by the charged particle within a distance L along the radiation particle track, E_c, must be larger than the energy required for bubble formation and is given by:

$$E_c = L\left(\frac{dE}{dx}\right) = \Lambda r_c\left(\frac{dE}{dx}\right). \tag{3.8}$$

Equation (3.8) associates the length L with the critical bubble radius by a numerical constant Λ. Hence, the nucleation requirement is satisfied if:

$$\left(\frac{dE}{dx}\right) \geq \frac{Ec}{\Lambda r_c} = \left(\frac{W}{\psi \Lambda r_c}\right). \tag{3.9}$$

By considering that the energy deposited along that part of the ion's range corresponding to twice the critical radius contributes significantly to bubble formation, Apfel et al. [41] found that the Gibbs energy W, given by equation (3.3), corresponds to only 3-5% of the energy deposited in the critical diameter $E_c=2r_c(dE/dx)$.

The thermodynamic factor $\psi=W/E_c$ (accounts for the conversion efficiency of heat to work) has been utilized to calculate the threshold neutron energy for a given liquid and temperature [41]. Because of the differing thermodynamic properties of the various available refrigerants employed in SDD fabrications, their response characteristics differ both with temperature and pressure. Recently [42], it has been observed that by introducing a non-dimensional quantity, "reduced superheat", defined as:

$$S = \frac{(T - T_b)}{(T_c - T_b)}, \tag{3.8}$$

where T_b and T_c are the boiling and critical temperatures of the liquid, respectively, the device responses all occur on a "universal" curve. For example, operated at $S \leq 0.5$, the SDD is insensitive to electrons, muons, gammas and other minimum-ionizing radiation, independent of its refrigerant basis (although this threshold occurs at different temperatures for different refrigerants). This indicates that the SDDs in particular thermodynamic conditions are capable of a self-background reduction.

The response of a detector depends both on its operating temperature and pressure. Figure 3.1 shows a simulation of the recoil energy threshold of each nucleus with increasing temperature for a C_2ClF_5 (R-115) SDD, at 1 and 2 bar [58,59]. At 2 bar, the device must be operated at a higher temperature or else the recoil energy of the nucleus (F, C and Cl) lower than 250 keV, will not allow detection of events up to 35°C, because the temperature equivalent to the threshold energy of each recoil nucleus (F and C) is shifted to near the sol–gel transition temperature at which the gel is liquid. The threshold neutron energy-temperature relation given in Figure 3.1 can be adopted to convert the temperature ramping scale (T=5°C and T=~35°C) for the SDDs at 1 bar, since at that temperature

interval it should elicit a response. The nucleation parameter used was $\Lambda = 1.4$ from reference [79], instead of the approximated value (2) for the majority of liquid refrigerants [41]. The results are in good agreement with the thermodynamic calculations and confirm the energy response as a function of temperature.
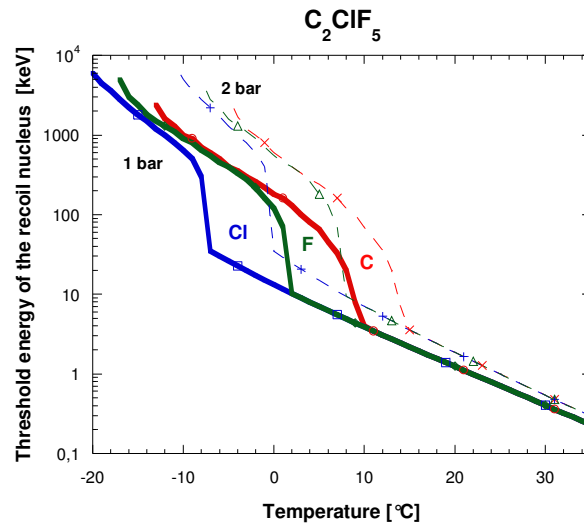
Figure 3.1: variation in threshold energy of the recoil nucleus with temperature for a C_2ClF_5 SDD at 1 and 2 bar.

3.3 Applications of Superheated Liquid Detectors

Superheated liquid detectors are used as dosimeters for neutrons because of their unique sensitivity response [43], which was in fact the origin of their introduction [44]. They have more recently been used in heavy-ion detection [45], and also in the direct search for particle dark matter [1,46].

3.3.1 Neutron Dosimetry and Spectrometry

SDDs have been pursued for applications in neutron dosimetry [43,44] and spectrometry [47,48,49] for almost two decades. They have been shown to comply with ICRP 60 recommendations for accuracy of measurement, real-time response, low minimum detection threshold and, most importantly, a nearly dose equivalent response [50].

More recent developments include position-sensitive neutron spectrometers/dosimeters for application in radiotherapy [51], in energy and angle-differential neutron fluence measurements [52], and in response enhancement to high energy neutrons [53]. In fact, the differential angle and energy double distributions of the fluence constitute the most complete description of a neutron field. The knowledge of angle and energy-differential fluence distributions permits correlating physical quantities

(kerma, absorbed dose) and non-isotropic protection quantities (organ doses, effective dose) or operational quantities (personal dose equivalent, directional dose equivalent).

3.3.2 Heavy-ion Detection

SDDs have been demonstrated to be good detectors for registration of high and intermediate energy heavy ions [54]. The ion tracks are visible by the naked eye and can be stored for months or years without losing their sensitivity. These detectors are also a type of threshold detector for identifying heavy ions. Based on these properties, bubble detectors are expected to have applications in heavy ion physics, cosmic ray physics, exotic particle detection and imaging of cancer therapy [55,56].

3.3.3 Dark Matter Searches

WIMPs are theoretically similar to that of elastic scattering slow neutrons. The fact that their interaction is weak implies that the event rates are extremely low – sufficiently so in fact as to be masked by common low-level radioactive backgrounds (such as cosmic rays, electrons and gamma rays) unless the search experiments are constructed of radio-pure materials and conducted deep underground. The insensitivity of the superheated liquid technique to the majority of these background complications is the driving force behind their application in this area.

SIMPLE (Superheated Instrument for Massive Particle Experiments) is one of only two experiments to search for evidence of spin dependent WIMPs using C_2ClF_5-based SDDs [17], the other being PICASSO using C_4F_{10} [16]. Given the weakness of the interaction, and that the rate scales with target mass, significant efforts have been made to increase the refrigerant concentration, resulting in 1-2% active mass devices (v-a-v their 0.1% dosimetry progenitors).

COUPP, although using the same technique, is based on a CF_3I bubble chamber [15].

3.4 Superheated Droplet Detectors

Superheated Droplet Detectors (SDDs) are a type of "superheated emulsion", which is the denomination adopted by the International Commission on Radiation Units and Measurements (ICRU) and International Organization for Standardization (ISO) for detectors consisting of uniform dispersions of superheated halocarbon droplets suspended in a compliant material such as a polymeric or aqueous gel [57].

Each droplet in the emulsion behaves like a bubble chamber. However, the liquid must be fractionated into droplets and dispersed in an immiscible host fluid, a process called emulsification. This procedure creates perfectly smooth spherical surfaces, free of nucleating impurities or irregularities. The emulsifier material must be clean and de-gassed, i.e., free of heterogeneous nucleation sites. Number, size and composition of the droplets can be varied in the fabrication of the detectors, as well as the ingredients of the gel too, permitting a wide range of applications.

3.4.1 SDD Fabrication

Protocols for detector fabrication are widespread and well developed [128]. Generally, these involve the use of polyacrylamide-based gels, with the addition of heavy element salts (which introduces radio-impurities) in order to density-match the gel with the refrigerant towards the production of a homogeneous droplet distribution. SIMPLE in contrast relies exclusively on the use of food-based gels, and viscosity-matching where necessary.

All fabrications generally involve three essential phases:

1. The fabrication of the gel;
2. The gel outgassing; that removes air bubbles trapped in the gel during the fabrication;
3. The suspension fabrication, in which the liquid is homogeneously dispersed in the gel in the form of micrometric droplets.

In the SIMPLE project, the SDDs are fabricated in-house [58] from C_2ClF_5 (R-115) with a 1-2% loading. The refrigerant is selected because of its low solubility (reducing the probability of unchecked bubble growth by permeation) and large molecular size. Liquid droplets (radius 5–150 µm) are fractionated by rapid stirring and dispersed in an elastic, viscous gel as shown in Figure 3.2.
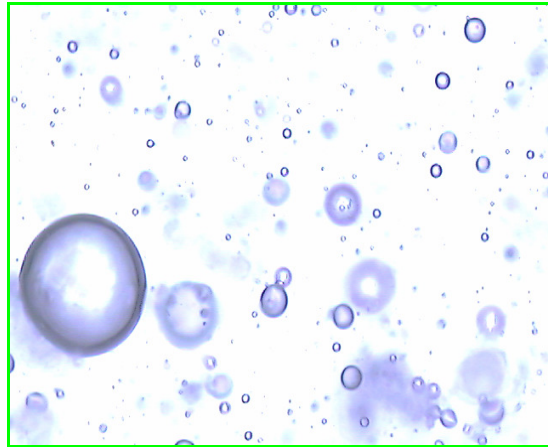
Figure 3.2: droplet microscopic picture.

A homogeneous droplet suspension is produced by adjusting the gel composition in order to obtain a uniform density, equal to that of liquid freon. The resulting mixture is out-gassed and maintained above its gelatine temperature before placing it in a hyperbaric chamber. The pressure is raised well above the freon vapour pressure to avoid boiling during the vigorous stirring that follows. After a uniform droplet dispersion has been obtained, cooling, setting and stepwise adiabatic decompression yield the SDD, as seen in the process diagrammed in Figure 3.3.
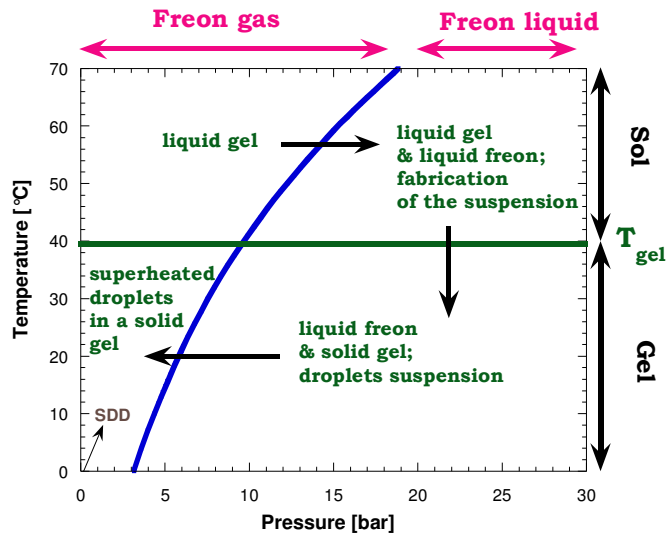
Figure 3.3: simultaneous creation of two metastable systems.

Some important precautions are strictly necessary for producing stable modules. For example, the stepwise decompression procedure used is identical to that employed by scuba divers returning to the surface, in order to minimize the cavitations of dissolved gas bubbles which, in SDDs, can act as inhomogeneous nucleation centers. In general, the size distribution of the droplets depends on the amount and speed of the stirring. As Figure 3.4 shows, the droplet size can vary from 5 to 150 μm in diameter [59].
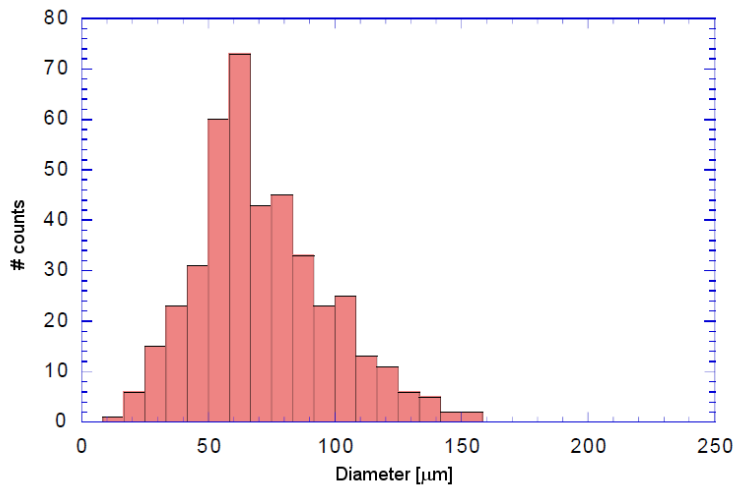
Figure 3.4: diameter size distribution within the SDDs [79].

The fabrication of a SDD detector takes approximately two days. Figure 3.5 shows one of the fabrication facilities, with its pressure chamber and accompanying pressure control, the temperature and stirring control that is used in the suspension fabrication and finally the refrigerant injection valve.
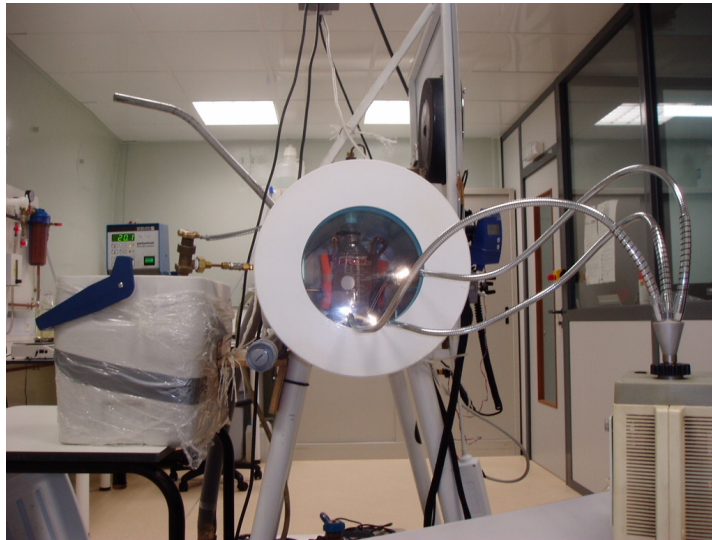
Figure 3.5: larger volume hyperbaric chamber of the project in the LSBB clean room.

In Figure 3.6, three sizes of SDDs are presented: (900 ml), (150 ml) and (80 ml).

Figure 3.6: three sizes of SDDs: from left to right, 900 ml, 150 ml and 80 ml.

The SIMPLE collaboration fabricates detectors with 6 different refrigerants: C_2ClF_5, CCl_2F_2, C_4F_{10}, C_3F_8, C_4F_8 and CF_3I.

3.4.1 SDD Instrumentation

The registration of a radiation-induced bubble nucleation event can be effected in three basic ways, as illustrated in Figure 3.7. The initial instrumentation of such devices was visual (bubble counters): at the end of the measurement, the numbers of bubbles were simply counted manually or automatically quantified using an optical scanner.
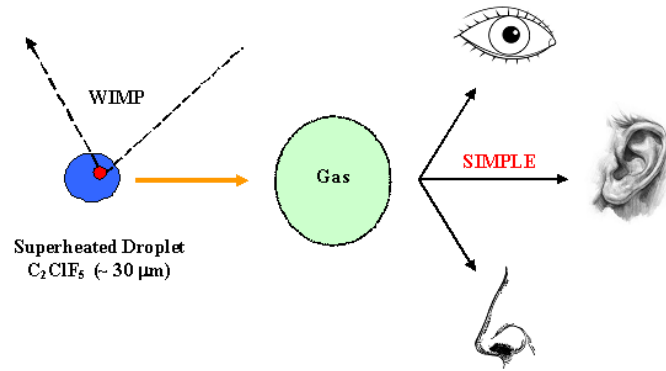
Figure 3.7: SDD instrumentation.

Volumetric measurements are also possible, in which the number of bubbles is inferred from the volume of the gel that they displace into a graduate vial or pipette.

Finally, the shock wave produced by the bubble nucleation and expansion can be recorded by an acoustic sensor and converted into an electrical pulse. This pulse tends to be a damped sinusoid with a typical duration of several milliseconds. An external impact, vibration or a microleak (nitrogen bubbles released through the plastic cap of the detector into the temperature control water bath) can however easily produce acoustical signals and potentially cause acoustic backgrounds.

The SIMPLE project pioneered the use of acoustic signal pickup, which gave the possibility to operate these devices in an active mode. This was however initially based on a poor response piezoelectric sensor, the response of which was essentially independent of the source. A significant problem in the early experiments was the presence of microleaks originating from the detector capping, which the piezoelectric sensor could not discriminate.

Other SDD experiments such as PICASSO [16] report the same principle of detection of a bubble nucleation in their superheated droplet detectors, although with different microphones and a different suspension gel.

Besides the acoustic pick up of each signal, the instrumentation is complemented with temperature and pressure readings of each device, both of which guarantee the conditions needed for the response of the detector in specific conditions for DM searches.

3.4.3 SDD Limitations

SDDs are promising detectors for personal and area neutron dosimetry. Currently, only two commercial manufacturers exist (Apfel Enterprises and Bubble Technology Inc.), offering several dosimeters and spectrometer devices. However, the weak points of bubble detectors are related to their problematic temperature dependence, the poor reproducibility and uniformity of the operational characteristics, and the dependence of the response on storage time. Another factor hindering SDD development is that many of the refrigerants are chlorofluorocarbons, which are controlled substances

under the Montreal Protocol due to their ozone depletion capabilities. Given the restrictions on their use, certain halocarbons are increasingly difficult to purchase.

3.5 Bubble Chambers

The bubble chamber was invented in 1952 by D.A. Glaser [61] when he discovered that ionizing radiation from a gamma-ray source could initiate boiling in a container of superheated solution, and had success in photographing a string of bubbles along the track of a cosmic ray.

The bubble chamber was used extensively during the following decades and several elementary particles were first detected by this technique. A variety of liquids have been used in bubble chambers, including hydrogen, deuterium, helium, propane, freon, and xenon.

The application and principle of a bubble chamber is similar to a cloud chamber. It is normally a large cylinder filled with a liquid heated to just below its boiling point. As particles pass through the chamber, its pressure increases, and the liquid enters into a superheated state. As charged particles pass through, they create an ionisation track, around which the liquid vaporises, forming microscopic bubbles. Bubble density around a track is proportional to a particle's energy loss.

Bubbles grow in size until they are large enough to be acoustically recorded or photographed. Several cameras can be mounted around the chamber, allowing a three-dimensional image of an event to be captured. Bubble chambers can have resolutions down to a few µm.

In any bubble chamber, the pressure must be reduced below a threshold pressure in order for bubbles to first appear along the track. While a bubble is growing, the liquid is cooling because of the evaporation that is taking place, and also due to the thermal diffusion from the heated region. It should be possible to analyze the early bubble formation process from which numerical simulations give some indications, by means of instrumentation for high frequency acoustics.

As mentioned before, COUPP is the experiment using bubble chambers in DM research [15] that does not have the problem of the SDDs in matching densities between refrigerant and gel.

3.5.1 BC Fabrication

The fabrication of a bubble chamber in principle is much easier than a SDD. Initially it is "only" the vessel and the superheated liquid. But the main problem has been to find the best possible container. In DM searches one must avoid as much as possible all metal parts, because of radio-contaminate backgrounds. It should be transparent, so that one can capture visually an event. It must have smooth walls to prevent spontaneous nucleations. And finally it is required to withstand a rapid increase of pressure.

3.5.2 BC Instrumentation

The instrumentation of a bubble chamber is similar to the SDDs, and must be attached directly to the bubble chamber. It basically consists of :

- Temperature transducers, conventional Resistance Temperature Detectors (RTD) devices or similar.
- Pressure sensors, for measuring the inner vessel and afterwards control of its recompression.
- An acoustic system, with one or more ultrasound microphones.
- One or two video cameras, for high resolution photography.

All signals are acquired and controlled via a suitable DAQ system.

The main advantage of the bubble chamber, besides the obvious gain in active mass, is the possible ability to pick up the embryonic phase of bubble formation with the use of high frequency acoustics [15].

3.5.3 BC Limitations

Although bubble chambers were very successful in the past, and have been recovered for DM searches in the last decade, there are some drawbacks:

- As with the SDDs, their temperature dependence. Since the frequent way to maintain these devices at an operational required temperature is by means of a large water bath.
- They become more expensive, since the high quality chamber, video cameras and ultrasound acoustics are expensive.
- The need for a photographic readout rather than just acoustics data makes it less convenient, especially in experiments which are underground (poor light), heavily shielded (immersed in water) and must be reset, repeated (mechanical stress) and analyzed many times.
- The superheated phase must be ready at the precise moment of collision, and the recompression system must work as rapidly and precisely as set by the experiment requirements. All of these steps have to be reproducible for long term cycles.
- Bubble chambers up to now are still neither large nor massive enough to compete with the leading DM experiments, especially in the spin-independent sector.

Chapter 4   SDD Instrumentation

_____

4.1 Introduction

The shock wave produced by the bubble nucleation and expansion can be recorded by an acoustic sensor and converted into an electrical pulse. This pulse tends to be a damped sinusoid with a typical duration of several milliseconds.

The SIMPLE project pioneered the use of acoustic signal pickup, which gave the possibility to operate these devices in an active mode. This was however initially based on a poor response from the sensor, and the response was essentially independent of the source.

4.2 Definition and selection of the microphone

To improve the discrimination capabilities of the SDD instrumentation, a new acoustic transducer is introduced. Since the frequency spectrum of a bubble nucleation is predominately in the audible range [62], a microphone with a range up to 16 kHz is chosen, with the hope that frequency-discrimination will also provide a means of identifying and rejecting spurious events.

A microphone is an acoustic-to-electric transducer that converts sound into an electrical signal. Microphones are used in many applications such as telephones, tape recorders, hearing aids, motion picture production, live and recorded audio engineering, in radio and television broadcasting and in computers for recording voice and furthermore for non-acoustic purposes like ultrasonic checking.

The most common method to translate these mechanical vibrations into an electrical signal is via a thin membrane producing some proportional electrical signal. Most audio microphones today use electromagnetic generation (dynamic microphones), capacitance change (condenser microphones) or piezoelectric generation to produce the signal from mechanical vibration.

In a condenser microphone, also known as a capacitor microphone, the diaphragm acts as one plate of a capacitor, and the vibrations produce changes in the distance between the plates. Since the plates are biased with a fixed charge (Q), the voltage maintained across the capacitor plates changes with the vibrations in the air, according to the capacitance equation

$$Q = C \times V \quad ,$$

(4.1)

where Q is the charge in Coulombs, C, the capacitance in Farads and V, the potential difference in Volts. For a parallel-plate capacitor, the capacitance of the plates is inversely proportional to the distance between them $C \propto 1/(d_2 - d_1)$.

The charge in the capacitor is not maintained perfectly constant. As the capacitance changes, the charge in the capacitor changes to make the voltage drop across the capacitor equal to the bias voltage. However, the rate of this change is kept slow by using a series resistor of order 10 MΩ.

Within the time-frame of the capacitance change (order 100 µs), the charge thus appears practically constant and the voltage across the capacitor adjusts itself instantaneously to reflect the change in capacitance. The voltage difference between the bias and the capacitor is seen across the series resistor. The voltage across the resistor is amplified and reproduced to audio or recording.

Condenser microphones range from cheap to expensive. They generally produce a high-quality audio signal and are now the popular choice in laboratory applications. They require a power source, provided either from microphone inputs as phantom power or from a power supply. Power is necessary to establish the capacitor plate voltage, and is also needed for internal amplification of the signal to a useful output level. Condenser microphones are also available with two diaphragms, the signals from which can be electrically connected to provide a range of polar patterns, such as cardioid and omnidirectional.

The electret microphone is a relatively new type of capacitor microphone, and is often simply called an electret microphone. An electret is a dielectric material that has been permanently electrically charged or polarized. The name comes from electrostatic and magnet; a static charge is embedded in an electret by alignment of the static charges in the material, much the way a magnet is made by aligning the magnetic domains in a piece of iron. They are used in many applications, from high-quality recording and dynamic use to built-in microphones in small sound recording devices. Though electret microphones were once low-cost and considered low quality, the best ones can now rival capacitor microphones in every respect and can even have the long-term stability and ultra-flat response needed for a measuring microphone. Unlike other capacitor microphones, they require no polarizing voltage, but normally contain an integrated preamplifier which does require power (often incorrectly called polarizing power or bias). This preamp is frequently phantom-powered in sound reinforcement and studio applications. While few electret microphones rival the best DC-polarized units in terms of noise level, this is not due to any inherent limitation of the electret; rather, mass production techniques needed to produce electrets cheaply don't lend themselves to the precision needed to produce the highest quality microphones. The final choice was on an electret microphone which delivers accurate frequency response and low distortion, operates on low voltages, resists the effects of vibration, shocks, and is practically indestructible. Hence, the new instrumentation selected for application in the identification and discrimination of spurious events for the superheated droplet detectors is based on a PANASONIC (omnidirectional) for PCB mounting, high quality electret microphone cartridge (MCE-200), shown in Figure 4.1, with a frequency range of 20 Hz – 16 kHz (3 dB), signal-to-noise ratio (SNR) of 58 dB and a sensitivity of 7.9 mV/Pa at 1 kHz [63].

Figure 4.1: a MCE-200 high quality electret microphone of about 5 mm^3.

4.2.1 Acoustic Electronic Circuit

The microphone is supported with a Texas Instruments PGA2500, a digitally- controlled, analog microphone preamplifier designed for use as a front end for high performance audio analog-to-digital converters [64]. Its characteristics include low noise, a wide dynamic gain range of 1-65 dB (1dB/step), and low harmonic distortion. DC offset is minimized by an on-chip DC servo-loop; common-mode rejection is increased via a common-mode servo function. The preamplifier is programmed using a 16-bit control word, loaded using a serial port interface. External switching of input pads, phantom power, high pass filters, and polarity reversal functions are controlled via four programmable digital outputs. The main functions of the PGA2500 are shown in Figure 4.2. Configurable input and output circuitry provide convenient prototype options, while the buffered host interface supports the supplied applications software and alternate host configurations.
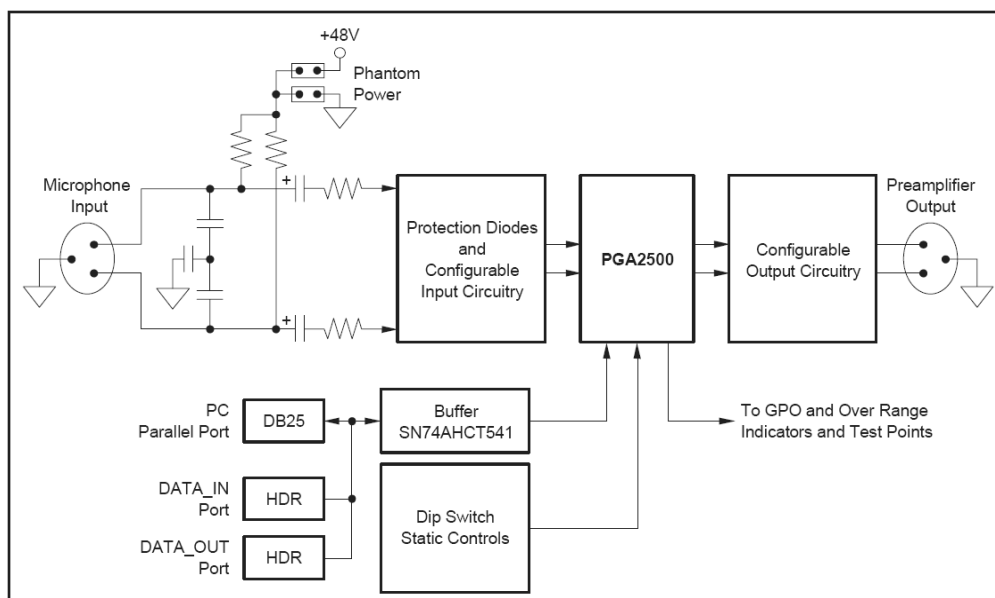
Figure 4.2: functional block diagram for the PGA2500EVM [64].

The suggested basic circuit configuration [64] was initially employed, with phantom power disconnected but with both +5 V and -5 V power supplies. Minor modifications of several capacitances and resistances were required in the course of testing for better stability. During testing however, it was found that the voltage regulators made the circuit unstable, and that the protective diodes

introduced noise into the system. In consequence, the configurable output circuitry was not used: the final electrical circuit for the PGA2500 /microphone system is shown in Figure 4.3.
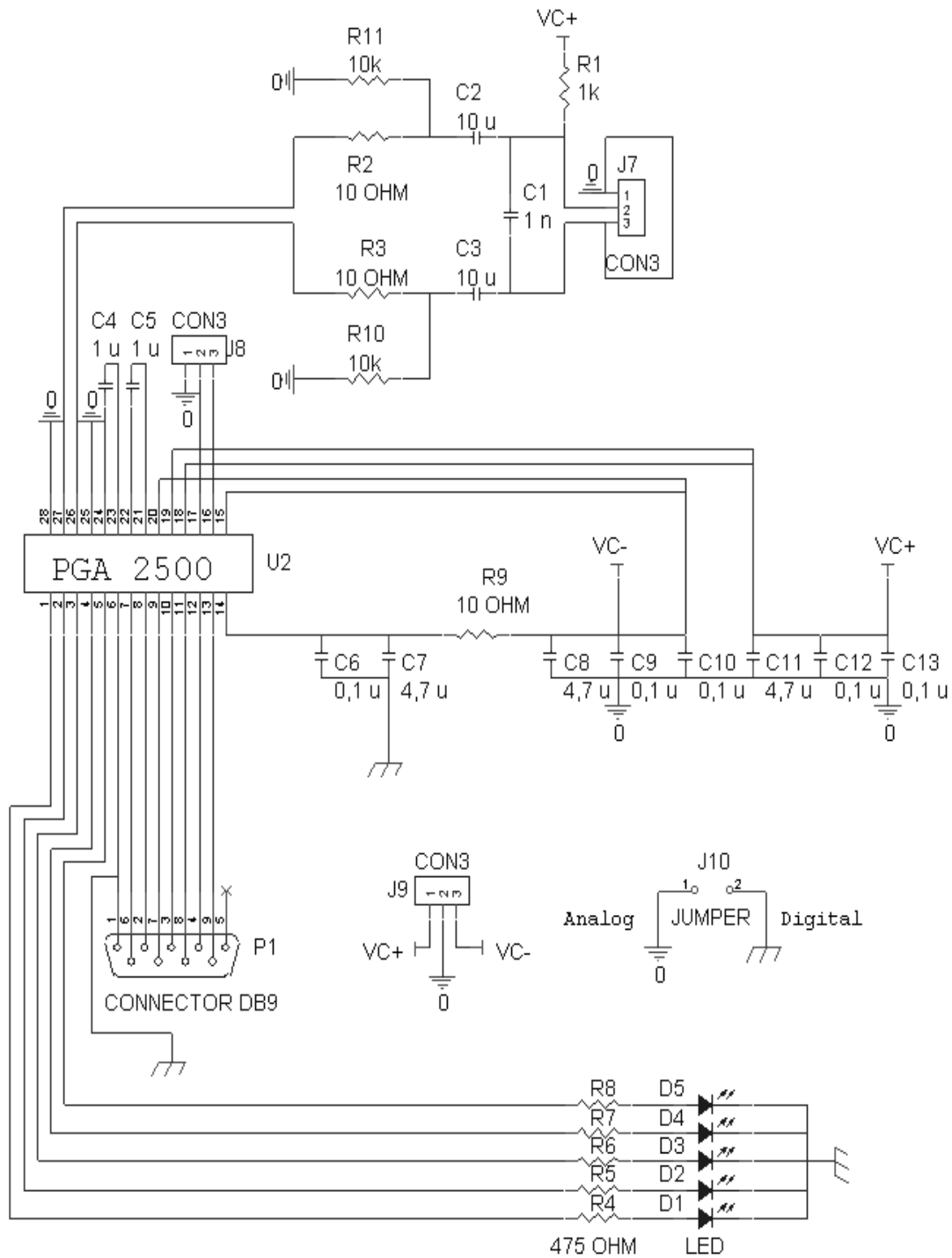
Figure 4.3: final electronic circuit for the PGA2500-microphone system.

The circuit was assembled on a two-layer printed circuit board using both through-holes and surface-mount components. The top and bottom layer plots employed from the circuit of Figure 4.3 are shown in Figure 4.4.
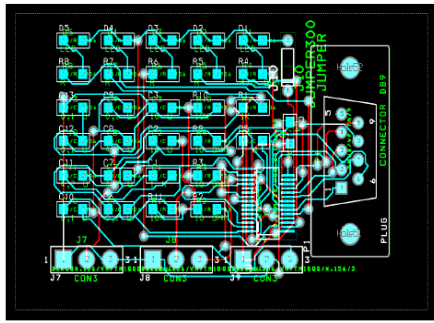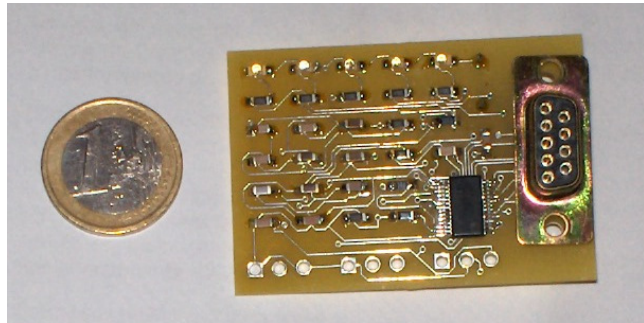
(a)   (b)

Figure 4.4: blueprint (a) and photo (b) of the assembled Surface Mount Display (SMD) electronics.

4.2.2 Pressure Electronic Circuit

The pressure transducer (PTI-S-AG4-15-AQ from Swagelok) is ideal for general use in a wide variety of industrial applications such as machine control, process control, test equipment and laboratory measurements.

These pressure transducers allow for electronic monitoring of system pressures in a variety of industrial or scientific applications. The products feature an accuracy of 0.5 % limit point calibration (0.25 % best straight line fit), and temperature compensation to ensure accuracy and long term stability when exposed to temperature variations. The transducers are zero and span adjustable, and to fulfil the SDDs requirements the one chosen had: a voltage output signal, 3 wires; an output from 0 to 10 V; the Supply V dc+ could range from 14 to 30 V and the minimum Load $R_L > 10$ kΩ. As seen from Figure 4.5, the acquired signal was taken from the positive output signal S+ and S- went to the common, ground.
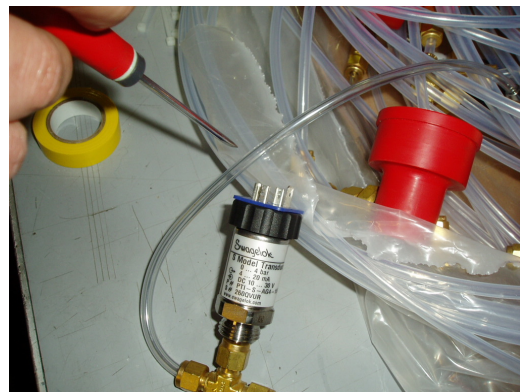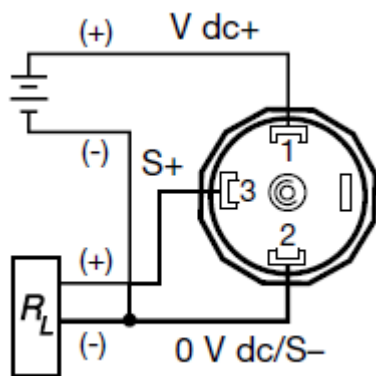
Figure 4.5: left, wiring diagram of the pressure transducer and right, a photo of it coupled to the tubing.

4.3 Instrumentation Robustness

A SDD is operated under a variety of noise, signal sampling, frequencies, temperature and pressure conditions, depending on its refrigerant and mission. All of these conditions may have adverse mechanical effects on the microphone, and require examination.

4.3.1 Noise Evaluation

At ITN several boards were constructed according to Figure 4.3 using standard SMD components, and tested with respect to noise. As seen in Figure 4.6, until 30 dB the noise level is ~ 1 mV, but the amplification might be insufficient for the observation of a nucleation event. Between 40 - 60 dB, there is no major difference, as all boards had the best noise level among themselves (13.02 ± 0.19 mV). The maximum gain (65 dB) was rejected, since the ~ 400 mV noise level prevents a clear identification of nucleation events. No significant difference in performance was registered among the five boards.
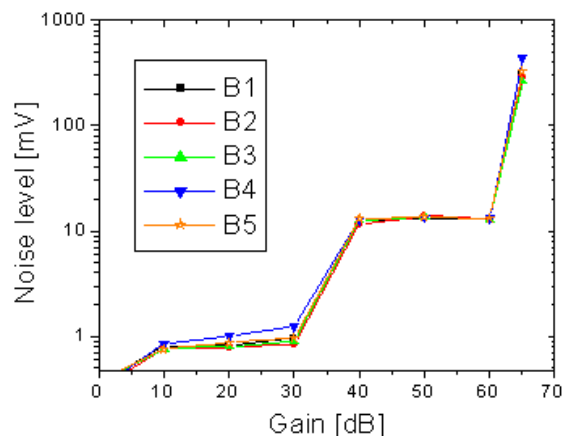
Figure 4.6: noise levels of five amplifier boards.

4.3.2 Frequency Evaluation

All boards were tested at unit gain, with the microphone coupled to a function generator, which as shown in Figure 4.7(a) was set to produce a sine wave with amplitude of 1.5 V and a frequency of 3 kHz. All boards produced a well defined peak around 3 kHz, as shown in Figure 4.7 (b).
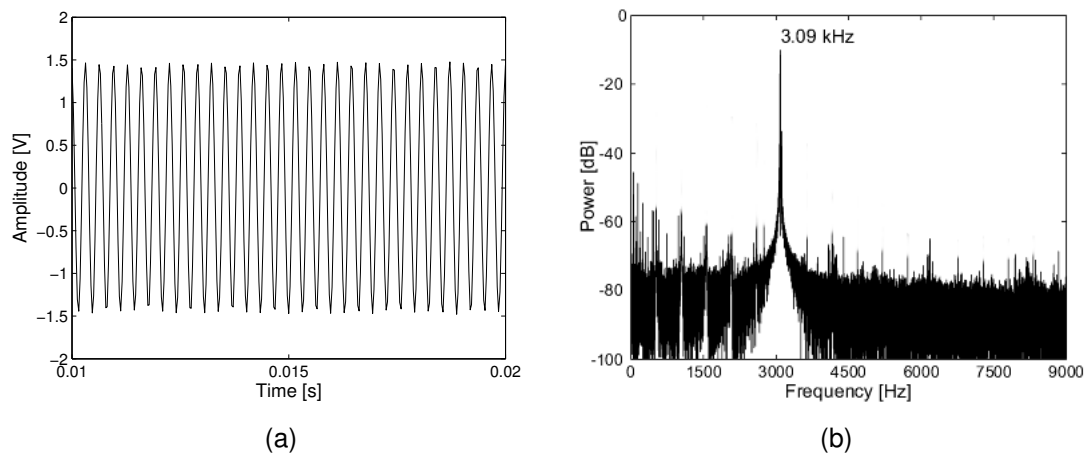
Figure 4.7: (a) signal output of the microphone + electronics against a 3 kHz function generator, and (b) its FFT.

4.3.3 Acquisition Evaluation

Several electronic events around 600 Hz were locally produced using the function generator and then analysed to show that the frequency response is independent of the acquisition sampling rate set in the acquisition program for the DAQ I/O digitizer. As seen from the events of Figure 4.8, acquiring the data at 8, 32 or 100 kSps, the response in frequency of the events is maintained within 5%.
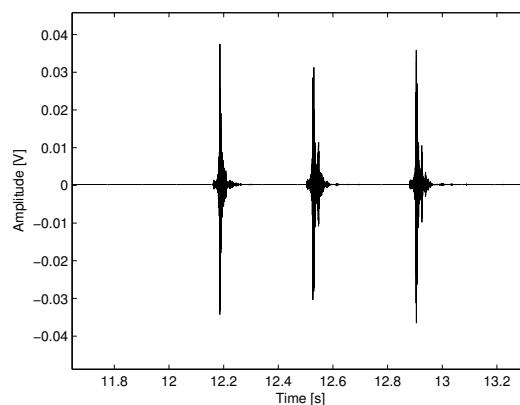
Figure 4.8: forced events for sampling evaluation.

Figure 4.9 shows the three events with a primary response around 600 Hz.
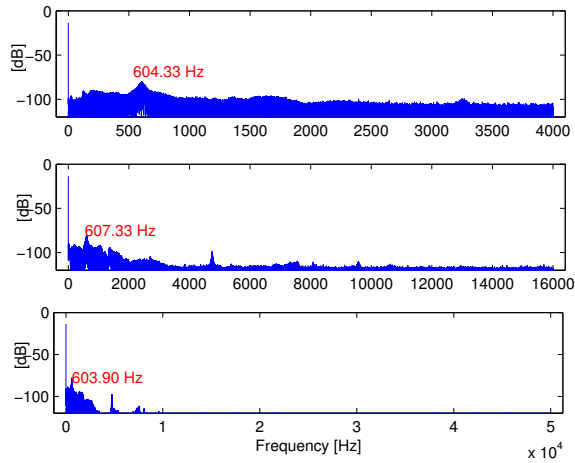
Figure 4.9: frequency response at three different acquisition sampling rates, 8, 32, 100 kSps.

4.3.4 Pressure Evaluation

Several electronic events were again locally produced and then analysed to show that the microphone pick-up response was independent of the acquisition pressure operation. As seen from the events in Figure 4.10, there is no absence of signal acquiring data up to 4 bar pressure.
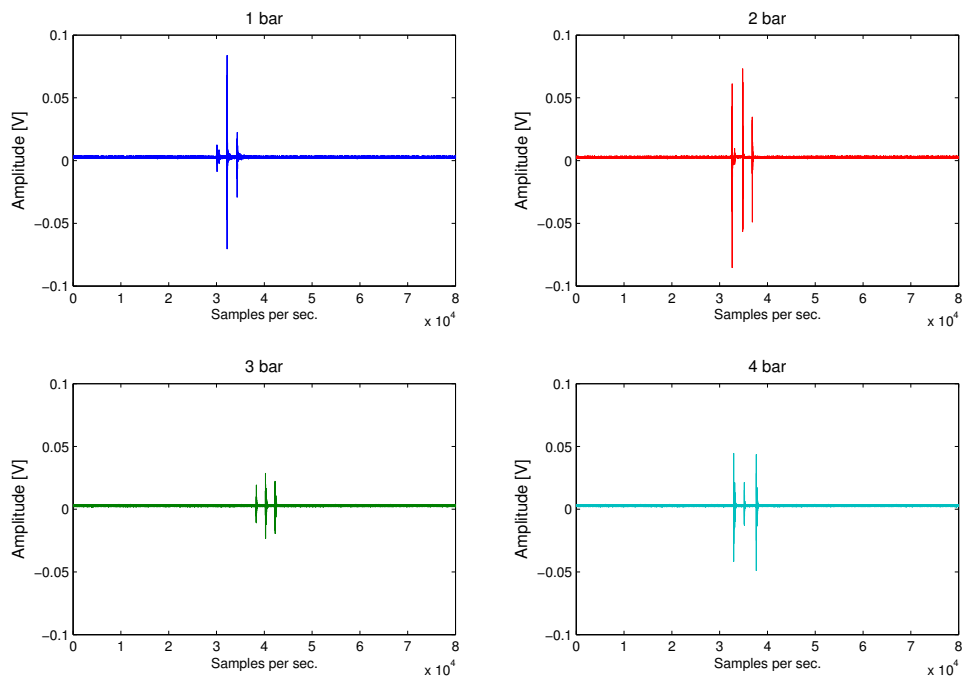
Figure 4.10: several events at pressures from 1 to 4 bars.

The differences in amplitudes are only a poor control of the induced events. To guarantee that events would be recorded even at a 4 bar pressure inside the vessel, all of these tests were performed with unit gain.

4.3.5 Temperature Evaluation

One of the microphones was cooled down in a normal cooler, to study its temperature behaviour over the operation range of SDDs. It was then "glued" to a hot plate and controlled by a PT100. Several events were recorded from 0 to 50ºC in steps of 5ºC. As seen from Figure 4.11, no significant changes are observed in the microphone pick-up of the signals and only at the two highest temperatures, above 40ºC, is the noise level raised 40%. This does not constitute a problem since these temperatures are above the SDDs normal operating temperature.
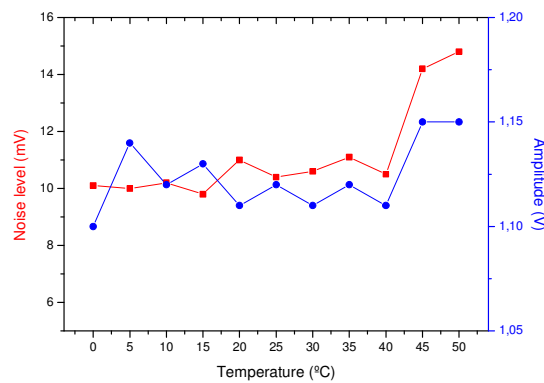
Figure 4.11: noise and several amplitude events for temperatures from 0 to 50ºC.

4.3.6 Comparison with previous transducer

The new microphone-based instrumentation was then tested against the previous piezoelectric transducer system [65]. The intent was to compare the efficiency in event counting. For this, both transducer and microphone were set side-by-side in a water bath, through which N_2 gas was bubbled at a constant rate. The result is shown in Figure 4.12: both systems recorded the same number of events, although the microphone signals show larger amplitudes and richer pulse structure, as expected. The main difference is in the information that one can extract from the new microphone, since the previous transducer can only record events, with no possibility of any source discrimination, all events produced a ~5 kHz frequency response [65].
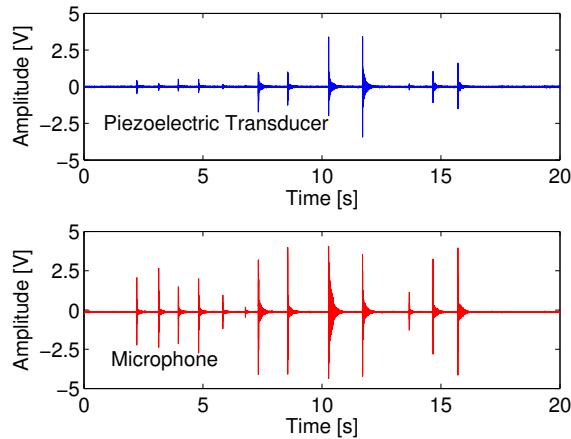
Figure 4.12: signal outputs for the piezoelectric (upper) and microphone (lower).

4.4 Identification and Validation of a Nucleation Event

The entire experiment was performed in a low noise environment. The SDD was warmed to 35ºC. Figure 4.13 shows the output from a 150 ml standard (2.5 g of CCl_2F_2) SDD warmed to 35ºC. A simple setting of an amplitude threshold does not guarantee that an observed spike corresponds to a nucleation; correspondence with spurious noise from microleaks or external noise is also possible.
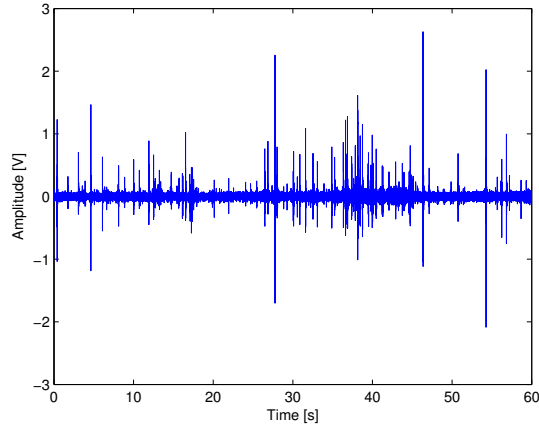
Figure 4.13: output from the microphone for a detector warmed to 35ºC.

Figure 4.14 shows the typical shape of a bubble nucleation (which corresponds to the first spike of Figure 4.13), in which can be seen both the oscillating pressure (resonant frequency) and the rise/fall envelope. The mechanical (acoustic) energy associated with a bubble nucleation must convey much more energy than a spurious noise spike, which is equivalent to the time constant of the decaying envelope being much larger for the nucleating bubble event than for spurious noise.
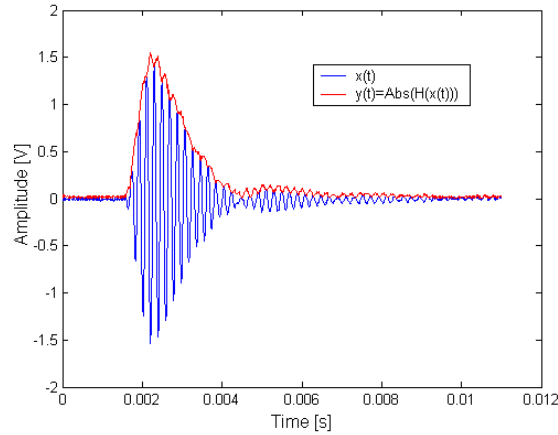
Figure 4.14: temporal evolution (pulse shape) of a typical bubble nucleation, corresponding to a zoom of a spike in Figure 4.13.

The result suggested the development of a simple pulse shape validation routine in which each pulse is first amplitude demodulated, and the decay constant then determined through an exponential fit. The event counting and validation routine executes the following steps:

- Sets an amplitude threshold;

- Identifies the beginning and ending of each spike, based on the previous threshold;

- Amplitude-demodulates the time evolution of the spike;

- Measures the decay time constant (τ) of the pulse;

- Suppresses the pulses which exhibit an τ below a given threshold.

The choice of the amplitude threshold usually is an interactive procedure, but can be set very low for the rejection of spurious noise. The amplitude demodulation is achieved simply by performing the modulus of the Hilbert transform of the pulse waveform,

$$y(t) = \left| \mathrm{H}\{x(t)\} \right|,$$ (4.2)

as shown in red in Figure 4.14 for the pulse of Figure 4.13.

Once the amplitude envelope has been obtained, the maximum and the minimum of the pulse shape are defined to set the time window of the pulse used for evaluating τ. The decaying part of the amplitude envelope is then fit to an exponential,

$$h(t) = Ae^{\tau.t},$$ (4.3)

by means of a linear regression after linearizing the envelope,

$$\ln(y(t)) = \ln(A) + \tau.t + er(t),$$ (4.4)

where *er(t)* corresponds to the residual of the fit. Figure 4.15 shows both the decay interval of an envelope, and its exponential fit.
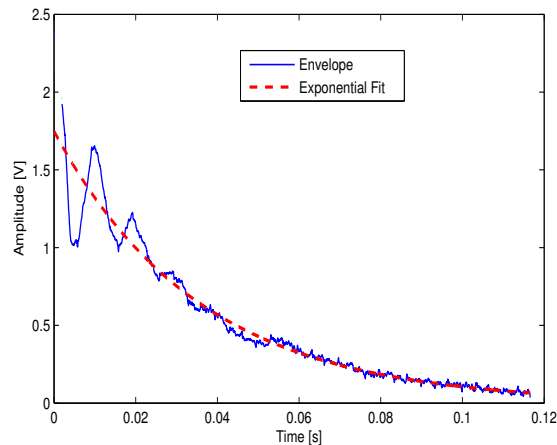
Figure 4.15: best fit of the exponential in Eq. 4.3 to the amplitude envelope of the pulse shown in Figure 4.14.

After isolating a single nucleation event as in Figure 4.14 and making a best fit of the amplitude envelope, the principle Power Spectral Density (PSD) response is found at ~640 Hz, as shown in Figure 4.16, with some lower power harmonics near 2 and 4 kHz. This is the typical frequency spectrum of bubble nucleation signals.
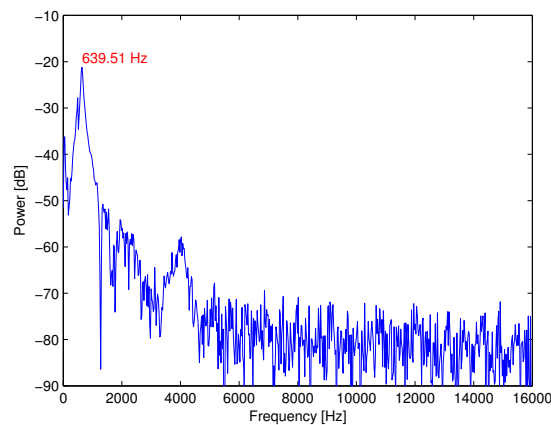
Figure 4.16: PSD for the nucleation event shown in Figure 4.14.

The SIMPLE SDD is generally operated at temperatures and pressures which provide a minimum nuclear recoil threshold energy while remaining below threshold for α's, β's and γ's [66,67]. In the case of a standard C_2ClF_5 SIMPLE SDD, these are generally 2 bar at 9ºC as seen in Chapter 3. In general, pressure increase raises the threshold recoil energy curve and shifts it to higher temperatures, as shown in Figure 4.17 for CCl_2F_2. These thresholds depend on the critical temperatures of the refrigerant (T_b (ºC) = -29.76 and T_c(ºC) = 111.8), and vary significantly between superheated liquids: different devices may be operated at higher temperatures or pressures, both of which may have adverse mechanical effects on the microphone.

34
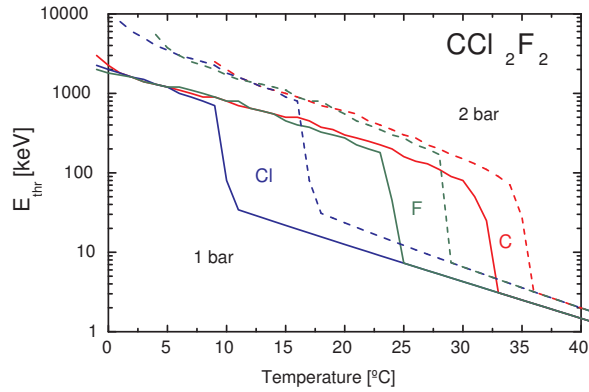
Figure 4.17: variation of threshold recoil energy curves for CCl₂F₂ with temperature, at 1 (solid) and 2 (dashed) bar.

Identification of bubble nucleation events was accomplished through a straightforward pulse-shape validation routine, which with the previous transducer instrumentation was not entirely possible. The frequency of a nucleation event was found to be ~ 640 Hz for a standard (CCl_2F_2) SDD made at the ITN facility.

4.5 SSD Response

4.5.1 Temperature Evaluation

A standard detector (2.5 g of CCl_2F_2), at atmospheric pressure, was ramped in temperature between 15 (~20 keV recoil threshold) and 35ºC, the latter set by SIMPLE's use of food gels for which melting begins. Given the (T,P)-dependent SDD threshold, the sensitivity varied over the experiments: for 35ºC, the reduced superheat factor [34] for CCl_2F_2 is 0.46, slightly below the s = 0.5 threshold for β,γ and μ sensitivity [67, 68], and the device was generally sensitive to only environmental neutrons and alphas. Figures 4.18(a) and 4.18(b) display the variation of noise level and recorded events, respectively, with detector temperature, normalized with respect to detector freon mass. Within experimental uncertainties, the noise level was basically independent of temperature. The number of nucleations increases abruptly above 20ºC, corresponding [67] to a minimum incident neutron energy of ~ 150 keV (~10 keV in recoil), as shown in Figure 4.18(b). Although usually indicative of a threshold crossing, the CCl_2F_2 is generally insensitive to minimum ionizing radiation below ~41ºC [34].

Figure 4.18(c) and 4.18(d) similarly display the variation with temperature of the signal amplitude and time constant, respectively.
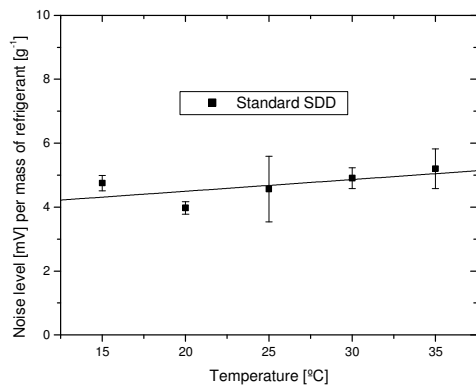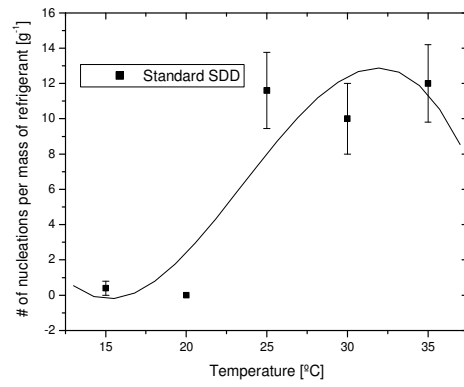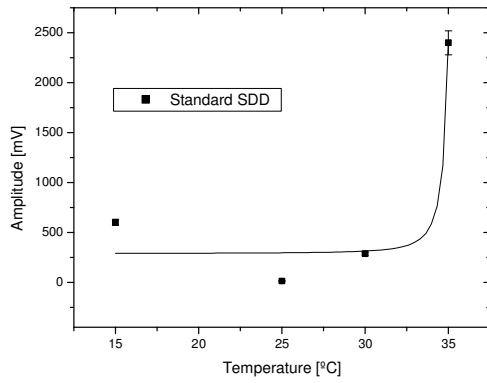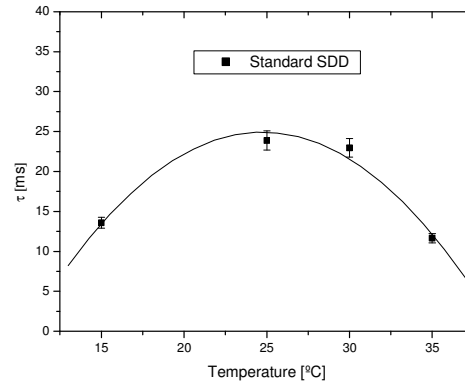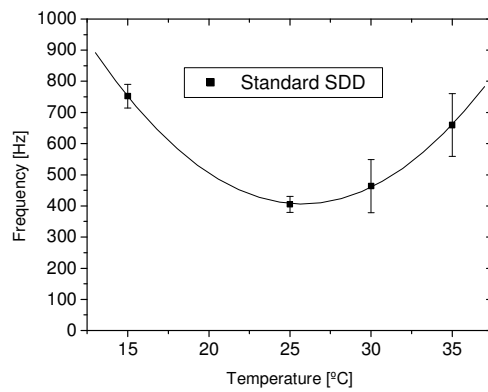
Figure 4.18: variation of signal (a) noise level, (b) event number, (c) amplitude, (d) time constant, and (e) frequency with temperature, for a CCl_2F_2 SDD at 1 bar pressure.

The amplitudes generally remain unchanged until the gel medium enters the pre-melting phase at 35°C, and the large signal increase is likely the result of multiple events coincident in time.

The time constants indicate ~ factor 2 variation over the temperature range, which surprisingly is parabolic with maximum in the midrange temperature. The variation of the frequency response with temperature is shown in Fig. 4.18(e), which also exhibits a parabolic behaviour with minimum at about the same temperature as the maximum of the signal time constants. Only a single principal frequency ranging between 450 – 750 Hz is observed at each temperature.

4.5.2 Pressure Evaluation

The SIMPLE C_2ClF_5 SDDs are generally operated at 2 bar in order to increase their insensitivity to common background radiations; they have been over-pressured to as much as 4 bar for transportation without damage to the construction. Since the CCl_2F_2 SDD sensitivity at higher pressures is shifted nearer the 35°C gel melting temperature, SDDs based on C_3F_8 were utilized for which the sensitivity is essentially the same in the 15-35°C range. The response of a standard (3.1 g) SDD at 2 bar is shown below in comparison with a similar C_3F_8 device at 1 bar. The 2 bar device suffered a gel meltdown at 30°C.

The temperature variation of the noise levels and recorded events are shown in Figure 4.19 (a) and (b), respectively. The noise level is essentially unchanged with temperature increase, rising only slightly as the gel melting temperature is approached and remaining identical with the 2 bar device.

The number of nucleation signals (see Figure 4.19 (b)) at 2 bar in the temperature midrange is ~ 4x less than at 1 bar, with the 2 bar results shifted to higher temperatures as anticipated. This is consistent with the signal amplitudes shown in Figure 4.19 (c), which at 2 bar are significantly lower than those at 1 bar, and most likely result from the compression of the microphone's diaphragm. In contrast, the time constants (see Figure 4.19 (d)) are essentially independent of the device pressuring, and show no evidence of a parabolic variation with temperature at either pressure.

Figure 4.19 (e) shows the recorded signal frequencies for both devices. The 1 bar results are uniform and with the same value to those of the CCl_2F_2 device at 25°C and 1 bar (Figure 4.18 (e)). At 2 bar, the frequency is a factor 2-3 higher than at 1 bar, consistent with the compression of the gel and stiffening of the propagation medium.

In all cases, microphone performance characteristics at 1 bar were restored following the 2 bar tests, indicating no physical damage to the microphone functioning at the elevated pressure.
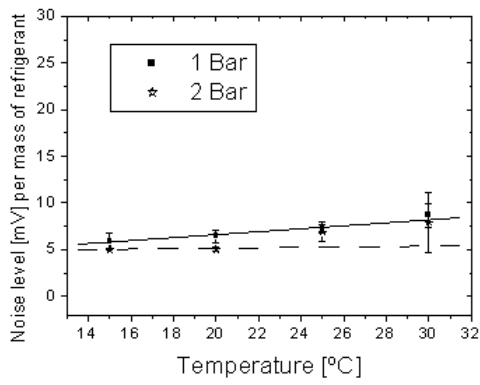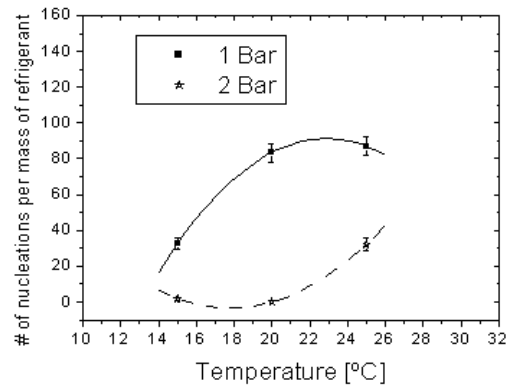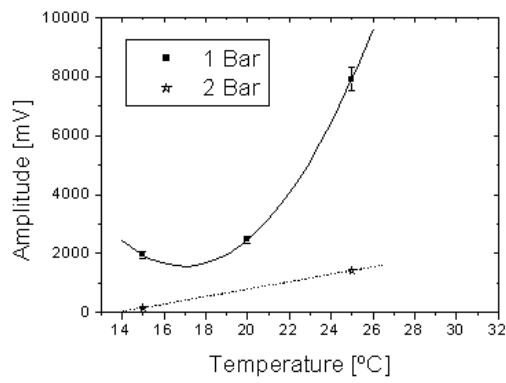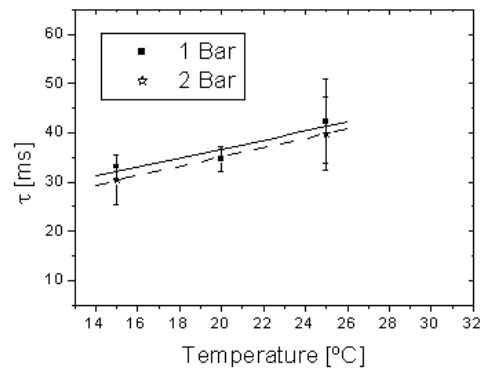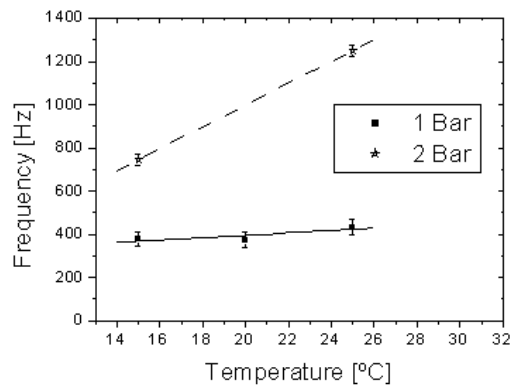
Figure 4.19: variation of signal (a) noise level, (b) event number, (c) amplitude, (d) time constant, and (e) frequency of a C_3F_8 SDD at 1 and standard SDD at 2 bar.

4.5.3 Glycerin Layer Evaluation

The previous instrumentation design mounted the transducer in a glycerin layer above the gel/refrigerant, shielded from direct contact by a latex sheath, in principle to amplify the transmitted acoustic wave from the gel [65]. The influence of the glycerin layer on a similarly–mounted microphone performance was examined using two almost identical, standard (150 ml), CCl_2F_2 (~2.5 g) SDDs, one without the glycerin layer. The devices were mounted in a water bath, as in the previous tests.

The temperature variations of the noise and recorded events, normalized to freon mass, are shown in Figure 4.20 (a) and (b), respectively. The noise levels are basically the same in both detectors, and flat with temperature, although the noise level is slightly less in the detector without the glycerin layer. As seen in Figure 4.20(b), the number of nucleation signals for the standard SDD increases with increasing temperature; without the glycerin layer, the microphone is in air and fails to record the majority of the nucleation events – which were confirmed visually afterwards.

This is further evidenced in the temperature variations of the signal amplitudes and time constants of Figure 4.20 (c) and (d), respectively. Except at the highest temperature, the few nucleation signals from the "no glycerin layer" detector have amplitudes that are consistent with the standard SDD. The associated time constants are essentially the same for both.

Figure 4.20 (e) shows the frequency variation of the two detector outputs with temperature. Apart from the one 1.5 kHz nucleation signal at 20ºC, the detector without the glycerin layer generally produced signals with frequencies around 30 Hz, in contrast to the standard SDD response with frequencies in the vicinity of 600 Hz.
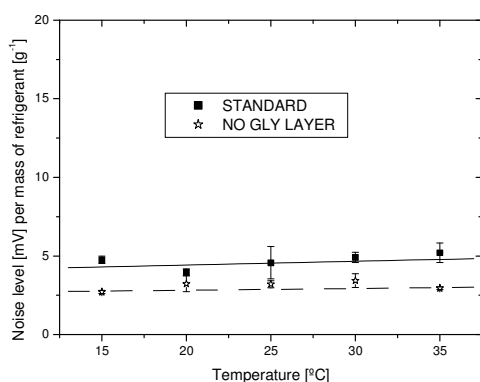
(a)
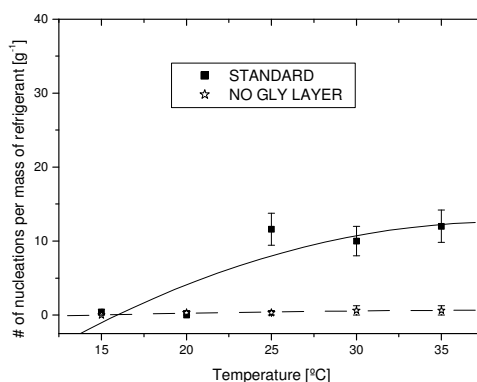
(b)
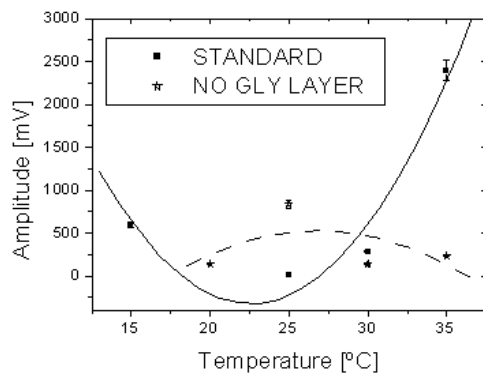
(c)
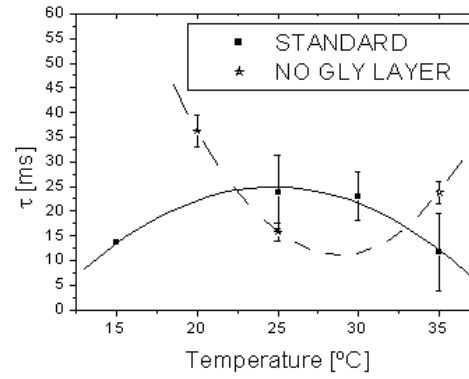
(d)
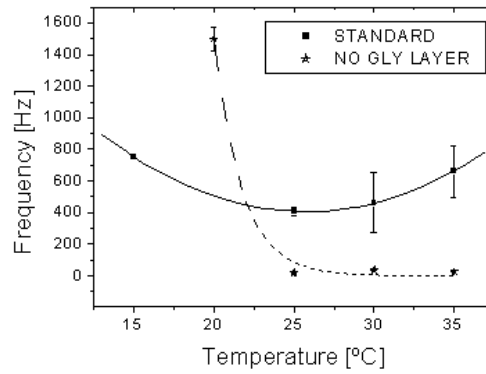
(e)

Figure 4.20: variation in signal (a) noise level, (b) event rate, (c) amplitude, (d) time constant, and (e) frequency for CCl_2F_2 detectors with and without the glycerin layer.

The overall performance demonstrates better than a factor 10 reduction in noise compared with the previous transducer instrumentation, with signal amplitudes increased a factor 2-10. No significant variation in the instrumentation response was observed in testing at different temperatures and pressures, beyond signal frequency shifts that may be related to the gel as its melting temperature is approached. The use of a glycerin layer surrounding the microphone and above the SDD is shown to provide a superior response.

The response of the new instrumentation, examined under a range of temperature and pressure conditions in which the SDDs are applied, yields no significant variations in the instrumentation output beyond signal frequency shifts that may be related to the gel as its melting temperature is approached.

The low noise and signal amplitudes of the new instrumentation in principle permit a capability of discriminating nucleation events from acoustic backgrounds common to SDDs, including micro-leaks, fractures, trapped nitrogen gas, etc.

4.6 Spatial Localization

An important concern is the radon contamination of the detector glass itself, which diffusing into the gel may produce α-decay initiated nucleation events up to ~ 1 mm (short-range interaction) from the interface.

One way to reject these events is by locating them spatially within the detector. The methodology behind this approach is based on the generalized cross-correlation (GCC) method for assessing time delays of arrival (TDOA) [69] between pairs of microphones within a microphone array. From the combinatorial TDOAs of the microphone array, a maximum likelihood estimator [70] is used to determine the most probable volume element for a bubble nucleation event.

The basic approach is a hybrid of triangulation. As shown in Figure 4.21, in addition to the normal single microphone (#5) mounted inside the SDD vessel, several additional microphones are positioned on the outside detector walls (#1-3) and bottom (#4).
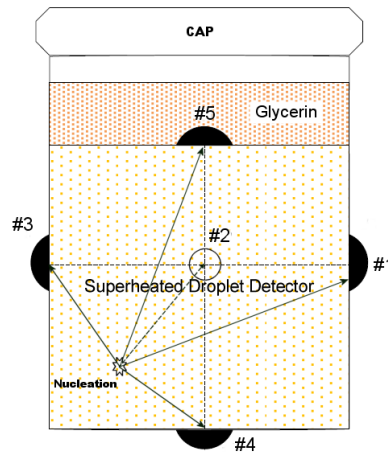
Figure 4.21: positioning of the microphones for the detector.

Given a bubble nucleation event, its relative distances, d_i, from each microphone are determined by taking into account the time delays of arrival, t_i, and the velocity, v, of the acoustic wave traveling through the gel:

$$d_i = v \times t_i \tag{4.5}$$

The signal analysis consisted of a 2 step procedure: event validation and then the spatial localization. In the initial step, for each of the data vectors, the identification of a true nucleation event is achieved through three measures. This process starts with the use of a continuous wavelet Morlet-based transform [71] as shown in Figure 4.22 (a), which is the wavelet transform most closely approximating the true nucleation event signal shown in Figure 4.22 (b); the choice is a result of a maximum likelihood study between a typical nucleation event and the several common wavelet bases, using the crest factor (ratio of the waveform peak amplitude and RMS value) as the cost function. The crest factor provides a quick idea of what is occurring in the time waveform. The scale at which the transform is analyzed depends on the gel, the pressure, temperature and whether the microphone is

inside or outside the detector. One major advantage afforded by wavelets is the ability to perform local analysis - that is, to analyze a localized area of a larger signal, and wavelet analysis is capable of revealing aspects of data that other signal analysis techniques miss, such as trends, breakdown points, discontinuities in higher derivatives, and self-similarity. In our application, this serves as a refinement for eliminating electromagnetic noise through pattern recognition.

(a)   (b)
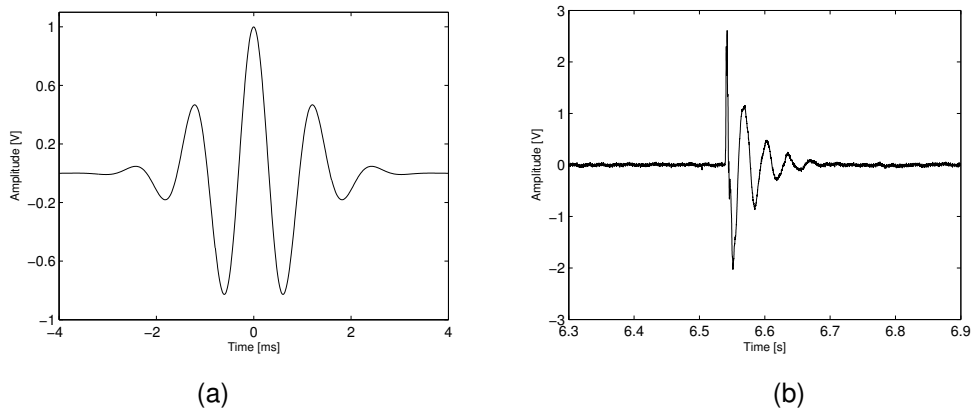
Figure 4.22: (a) Morlet based transform; (b) true nucleation signal.

From the output of the wavelet transform analysis, the selection of the possible candidates for nucleation events is carried out by threshold analysis, with the threshold set at ~5% above noise level.

Each of the possible candidates then separately undergoes a time and frequency analysis for distinguishing true nucleation events from acoustic backgrounds. This is accomplished through the validation routine which:

(i)   sets an amplitude threshold;

(ii)   identifies the beginning and end of each spike, based on the previous threshold;

(iii)   amplitude-demodulates the time evolution of the spike;

(iv)   measures the decay time constant (τ) of the pulse;

(v)   suppresses the pulses which exhibit τ's below a given threshold.

The frequency analysis was carried out for each candidate window using the Chirp-Z transform [72] and analysis of the spectrum in a 450 - 750 Hz window within which the oscillations of the nucleation signal are expected to be found. Power spectrum (PS) analysis using fast Fourier transforms (FFTs) is a powerful technique for signal analyses; the Chirp-Z transform is adapted for signals with low signal-to-noise ratio, and serves to improve the frequency resolution.

A final cut is applied to all surviving candidates: a true nucleation signal must be present, nearly simultaneously, on all channels.

The spatial identification step, since the geometry of the problem is well known, consists of mapping the detector volume with a regular, dense, hexahedron mesh, with each element of volume ~5 mm^3 (the voxel). For each voxel, the TDOAs of all the combinatorial pairs of the microphone array for events taking place at each voxel are computed and stored in a multidimensional matrix. The

matching of the voxel with each event is carried out by a Least Mean Square algorithm which compares the experimental TDOAs of pairs of the microphones with the those previously calculated and stored for each of the voxels.

The positioning of microphones outside the detector containment vessel raises the concern as to the effect of the gel-glass interface on the signal detection/analysis. While the gel-glycerin interface of the standard glycerin-immersed microphone is not an issue, since the main constitution of the gel is glycerin; the gel-glass is an issue, since one might suspect that the signals suffer a wavelength shift in transmission.

4.6.1 Measurement of the Sound Velocity Wave in the Gel

Three types of measurements were performed: the velocity of sound in the gel, a study of the signals recorded by the external microphones relative to the internal, and spatial localization using a "hot probe" at known positions.

The sound velocity (v) within the media needs to be accurately known since it directly relates to the spatial resolution of the system; for mm resolution, this requires an accuracy of about 2-3%. The velocity of sound at ~10ºC in the detector gel has been previously estimated as ~1800 ms^{-1} [73]. Since the velocity varies considerably with the gel consistency and temperature, measurements were made using the standard gel of the SIMPLE detector.

A cylinder 2 m long with a 5 cm radius was lined with acoustic shielding to prevent reflections from the walls, and filled with gel. For the acquisition, a National Instruments PXI-5105 high-speed digitizer was used, generating a short Gaussian pulse signal through the gel via a piezoelectric ceramic underwater speaker (SPS-4640-UW-01 from SONITRON). The signal was received by a waterproof microphone (MR28406 from Knowles Acoustics). The measurement procedure consisted of the sound emission, with central frequency at 1 kHz and 100 Hz bandwidth, and its reception; the time delay was assessed through correlation between emission (E) and reception (R), as shown in Figure 4.23.
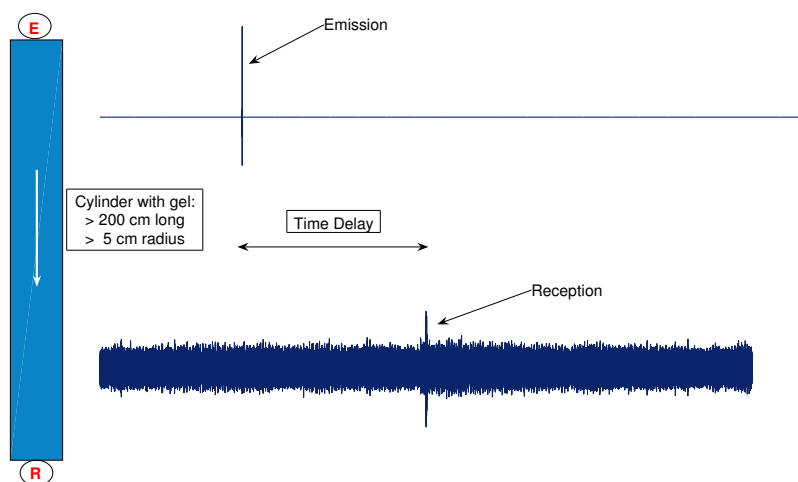
Figure 4.23: experimental set-up for the measurements of the velocity of sound in gel.

The system was calibrated in both air and water, at ambient conditions, with the receiver positioned at distances between x and y in 25 cm steps, yielding 325.6 ± 7.4 ms^{-1} and 1429.2 ± 36.3 ms^{-1}, respectively. Identical measurements, with the gel installed in the tube, are shown in Figure 4.24. A simple linear regression of the data gives $v_{gel} = 1654.4 \pm 40.2$ ms^{-1} at 18ºC and 72% relative humidity. At operational temperatures the gel is much closer to being a solid than a liquid. The increase of temperature promotes the transition from the solid to liquid state; therefore a decrease of sound velocity is expected [73].
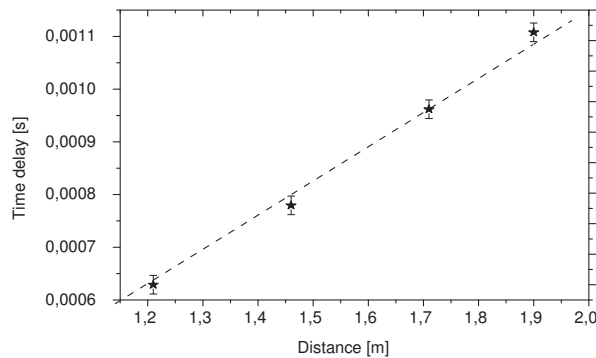
Figure 4.24: velocity of a sound wave through the gel.

4.6.2 Gel-glass barrier

Four external microphones were glued to the outside of the vial using epoxy; a thin (1mm) outer perimeter rubber layer was used between the microphone and the glass to avoid mechanical acoustic coupling. The fifth (standard) microphone, encased in a latex sheath, was installed inside the detector within the protective glycerin layer above the gel matrix, as in a standard detector construction. The disposition of the 5 microphones is shown schematically in Figure 4.25.
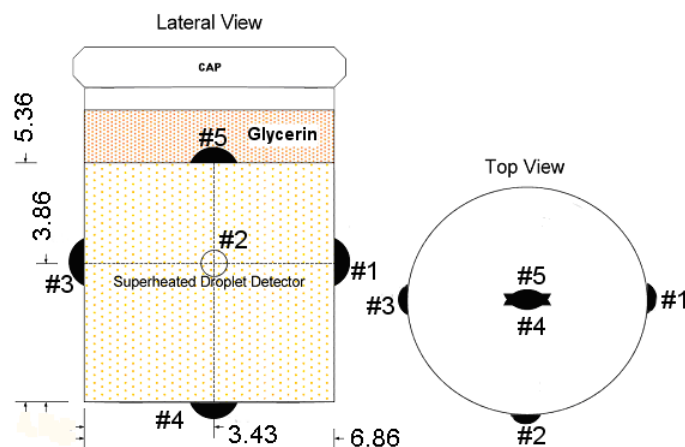
Figure 4.25: schematic of the disposition for the 5 microphones. Dimensions are in cm and # denotes the microphone number.

The detector itself contained ~ 2.5 g of the refrigerant (CCl_2F_2) in a uniform droplet (30±10 µm diameter) [78] dispersion, produced according to the standard protocol for a 150 ml device. It was placed in a water bath for temperature control and shielding. Measurements were made at 15ºC and 30ºC well below the gel melting, and at 45ºC to ensure rapid surface events. The temperature was measured with a type k thermocouple [RS 219-4450]. Each temperature change required ~15 min stabilization time for the SDD. Data was acquired at a constant rate of 32 kSps for a period of 5 minutes and with a gain of 60 dB, using a Matlab platform.

Events were stimulated by environmental radiation while heating up the detector in the water bath, and were cross-checked against nucleation events generated by irradiating the detectors using a quasi-monochromatic 54 keV neutron beam obtained with a Si + S passive filter at the Portuguese Research Reactor - ITN [74].

Figure 4.26 shows typical results of a measurement run. The noise level is ~ 7 mV for all 5 microphones for all temperatures. As expected, the signal amplitudes of the microphone inside the detector are higher than those attached to the sides and bottom of the detector, although at 30ºC all are the same within experimental uncertainty. At 45ºC all outside microphones recorded nucleations with amplitudes below 500 mV; the inside microphone ~ 800 mV. The lines presented in the figures are the best fits to the data, without benefit of theoretical prejudice.

(a)   (b)
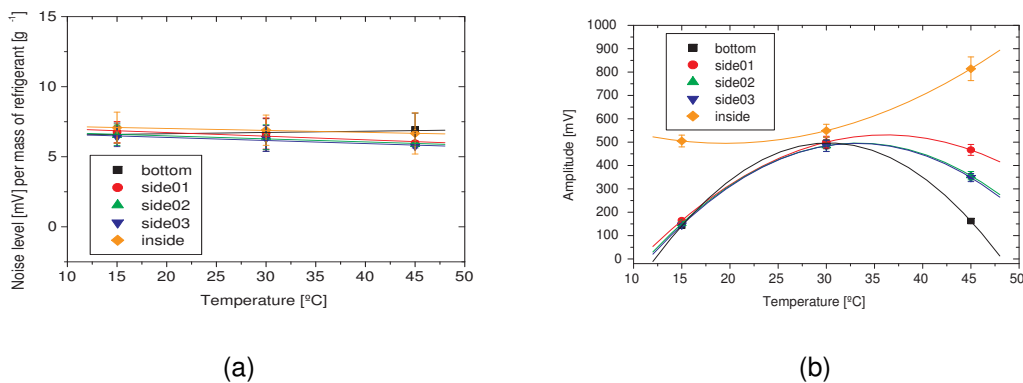
Figure 4.26: variation in (a) noise level and (b) signal amplitude for the 5 microphones with a standard CCl_2F_2 SDD as described.

The time constants of the recorded events are presented in Figure 4.27 (a). Those of all 4 microphones outside the detector are low, due to the wavelength shift in crossing the gel-glass interface of the detector. With the exception of microphone "side03", all τ's seem approximately constant and factor ~4 lower than that of the microphone inside the SDD, which τ decreases slightly (40 → 30 ms) as the temperature of the detector rises and the gel becomes less stiff. This shift, although significant, is not critical to the validation process since the time constants remain within the 5-40 ms acceptance window for true events.
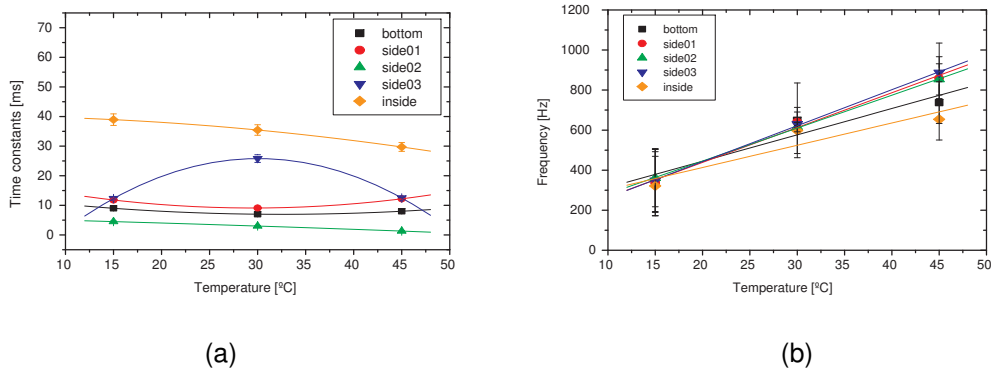
Figure 4.27: variation of signal (a) time constants and (b) frequencies for the 5 microphones.

All microphones yield the same frequency for the same events within experimental errors. As shown in Figure 4.27 (b), only at 45ºC are the recorded frequencies of the outside microphones 10-50% higher than inside, which is most likely related to the gel's melting from the exterior towards the center due to its placement within the temperature-regulating water bath.

4.6.3 Spatial Identification

The microphone disposition was identical to the previous tests, with the internal microphone removed to admit the entrance of a hot probe. The electronic setup was connected to the microphones using long shielded cable (~ 5 m). The electronic setup was itself also shielded to minimize electromagnetic noise.

The detector contained ~ 2.8 g of CCl_2F_2 in an uniform droplet dispersion and was produced according to the standard 150 ml device protocol. It was maintained at room temperature: since a hot probe was used to stimulate nucleation events, there were no temperature variations in the experiment. The entire set-up was placed inside an acoustic foam cage constructed for the purpose of ambient noise reduction.

The hot probe consisted of a 2 mm diameter platinum rod heated by electrical resistance. The probe was inserted 1 cm deep inside the detector's gel, and roughly between microphone "side01" and "side02" (see Figure 4.25). A typical transducer output is shown in Figure 4.28. One can see that the three side microphones register approximately equal amplitudes for the nucleation event. The microphone placed under the detector barely recorded a signal, which is most likely due to the ~ factor 2 greater probe-microphone distance than the side microphones. The differences in waveforms between the "side01/side02", and "side03" signals, the latter of which was about the same distance from the event, bears further study since they may contain additional information beyond the simple event occurrence.
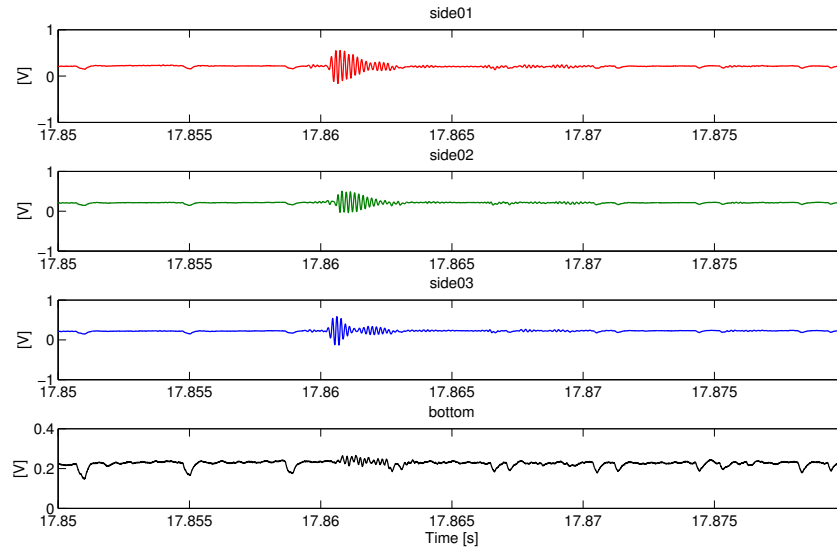
Figure 4.28: temporal evolution (pulse shape) of a typical nucleation signal, for each of the four sensors.

The noise level was (5.33 ± 0.03) mV for all 4 microphones. The nucleation signals all have roughly the same frequency, (0.98 ± 0.16) kHz, shifted upwards from 0.6 kHz. This increase is most likely due to the increased gel temperature of the hot probe stimulation.

The heating probe was next inserted at five angular positions at the top of the detector to depths of up to 2 cm, and heated for 20 seconds. Data was acquired at a constant rate of 500 kSps with a gain of 60 dB, using a Matlab platform. In this case a Keithley KUSB-3100 Series USB data acquisition hardware module was used.

The signals were processed as described earlier (see Sec. 4.4): assessing the occurrence of the events was made using the continuous Morlet waveform transform, with a larger range of 0.2 – 1.3 kHz for the Chirp-Z step, setting the time envelope for time constants between 5 and 40 ms and finally requiring a simultaneous occurrence in all channels. Once the time validation was accomplished, the spatial localization was performed by generating all delay combinations between the microphones for each of the voxels that make up the detector space. These were compared with the pre-determined delays in the multi-dimensional matrix, and the voxel best satisfying all delay constraints determined. Since the probe heated the emulsion along its entire length, the voxel was only truly characterized in the horizontal plane.
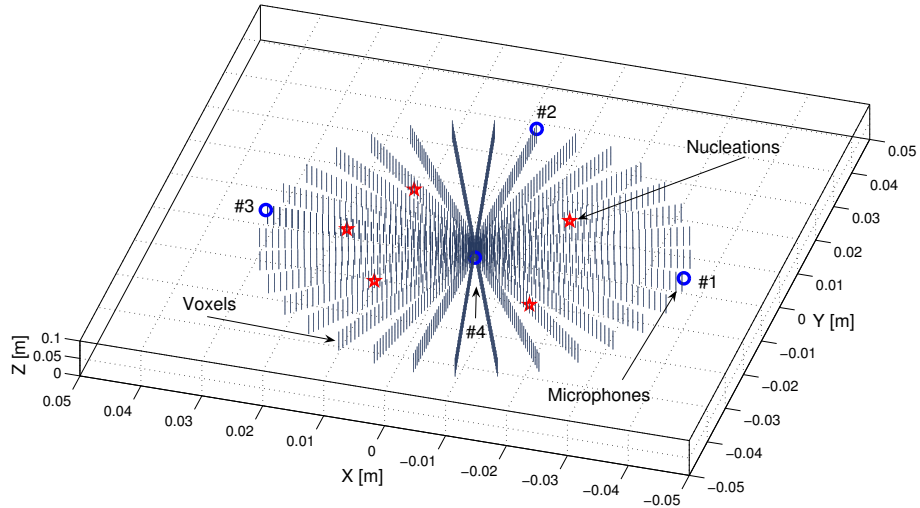
Figure 4.29: bubble nucleation map when inserting heating probes at five angular positions (π/4, 3π/4, 5π/4, 7π/4, 0) and radius 1.71 cm at depths of 0 cm to 2 cm from the device top. The microphones identify the limits.

Figure 4.29 shows a nucleation map resulting from the measurements. From these, at 1 bar pressure and room temperature (~20ºC), the resolution was 1.46 mm^2 with a 90% confidence level. The resolution was poorest along the centre of the detector, especially in its middle.

The determination of the time constant of a nucleation event signal and its frequency is usually enough to discriminate real from background signals. The microphones placed on the outside of the detector presented variations in the signal amplitudes, time constants and frequencies. These variations, although different, continue to permit discrimination through these parameters.

The spatial localization so far obtained is obviously crude in resolution, since it is not yet taken into account the sound dispersion in the gel with a given bubble concentration, nor the reflections of the sound wave from the walls of the detector. The dependency of the gel condition on temperature also contributes to larger errors, since the velocity was used in all calculations was 1654.4 ms^{-1} determined at 18ºC; the 2ºC increase in the gel temperature reduces the sound velocity. Assuming that this decrease is linear, at 20ºC the sound velocity is ~1508.8 ms^{-1}, and consequently the resolution is 1.21 mm^2 at a 90% confidence level.

The results also establish that the use of three microphones is the minimum needed to locate the voxel in a plane. As seen in Table 4.1, there are no major improvements when one of the microphones is not used, although the resolutions are slightly lower when the bottom (#4) and side01 microphones are not used; this is explained by the hot probe being closer to the remaining microphones.

Table 4.1: Acoustic spatial localization errors for different combinations of microphones.

Microphones				Resolution [mm^2]
Bottom(#4)	Side01	Side02	Side03	90% Confidence level
x	x	x	x	1.21
x	x	x	out	2.28
x	x	out	x	2.02
x	out	x	x	1.08
out	x	x	x	1.25
out	out	x	x	131.80

These experiments indicate a 2D localization ability with resolution a factor ~2 larger than the mesh resolution (0.64 mm^2). The spatial localization tests are 2D only, since the hot probe generates a "hot line" within the gel larger than the 2 mm probe diameter, and likely produces simultaneous multiple bubble nucleations. This is likely the reason for the current resolution. A more accurate 3D testing requires development of a small diameter probe with active tip only.

4.7 SDD Tomography

Neutron radiography and tomography are efficient tools for inspecting the internal structure of materials. The neutron tomography system is installed at the reactor of ITN, in the horizontal access of the thermal column and provided a parallel beam having a 5 cm diameter at the sample irradiation position. This operational equipment in present conditions needs 90 seconds of irradiation time to obtain an image, with a spatial resolution of about 300 μm.

Imaging techniques can be classified according to the penetrating radiation type, such as X-rays, γ–rays, and neutrons; because of their attenuation characteristics, in many cases they are complementary [75]. Neutrons are strongly attenuated by H-rich substances even when wrapped by thick metal layers while for X-rays the inverse occurs. For neutron tomography it is necessary to obtain about 200 single 2D images over 180 degrees. The images are captured using a Peltier-cooled CCD camera.

Figure 4.30: CCD photograph of the SDD.
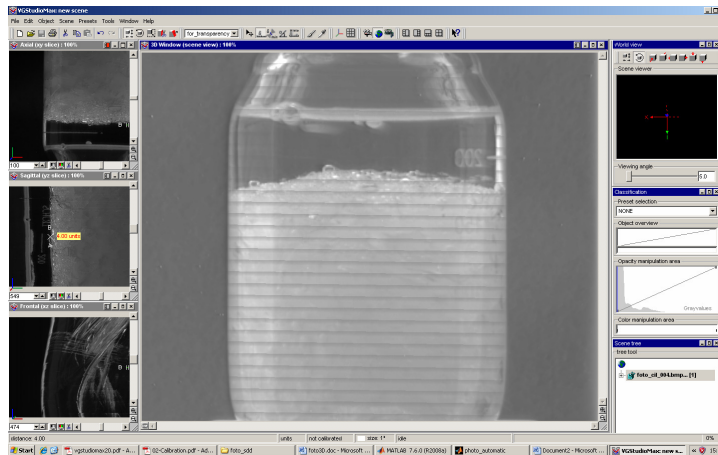
Figure 4.31: CAT scan of a SDD.

As seen in Figure 4.30, a photograph taken from the CCD camera of the SDD is of good quality: one can see bubble nucleations, fractures, etc. Once the tomography trial was performed, the immediate assessment was that little information can be added to what is already known (Figure 4.31). Since the SDDs are fabricated with H-rich elements, besides size and relative distances of bubbles at the surface of the gel (~4 mm), not much can be added, such as inner detector performance or bubble formation. If SDDs are to be utilized in applied tests with embedded samples inside the SDD, to provide solutions for measurements of alpha contamination in ultra-low activity materials, the results will probably be more motivating.

Chapter 5   SDD Characterizations

_____

5.1 SDD Dynamics

There are two types of background signals to be considered in any dark matter search with SDDs: those arising from acoustics associated with the SDD dynamics and search location, and those arising from background particle-induced events. The second is elaborated in Chapter 6. I here describe only the first.

The goal of a SDD instrumentation, apart from registration of true particle-induced nucleation events, is a capacity to discriminate signal events from a variety of general acoustic backgrounds common to SDD operation, which in an underground, low background environment constitute a significant contribution to the event record. The pulse shape validation routine is to be employed as a first stage filter, in order to reduce the amount of required signal analysis.

As seen in Chapter 4, a new microphone (MCE-200) was selected and a simple but efficient electronic circuit for the microphone was designed and built. Several of these electronic systems were tested and calibrated at ITN for the purpose of a new instrumentation applied to SDDs. The overall noise levels were reduced to acceptable values, ~ 10 mV with a 60 dB gain.

5.1.1 Microleaks

A microleak is a nitrogen bubble released into the water bath through the containment cap. These microleaks occur since the detectors are pressurized. Pressure microleaks were forced by simply not tightening the new cap. The new cap was developed and built with openings for several feedthroughs needed (microphone and pressure system) unlike the previous Phase I whose openings were handmade and glued. Typical results are shown in Figure 5.1 (a), where one observes a large number of water bubbles from the bath container of the SDD. Isolating and zooming in on one of the spikes (Figure 5.1 (b)), the pulse shape is seen to be not much different from a true bubble nucleation, although there might be some indication of discrimination capability if the frequency is somehow different from a true bubble nucleation.

(a)   (b)
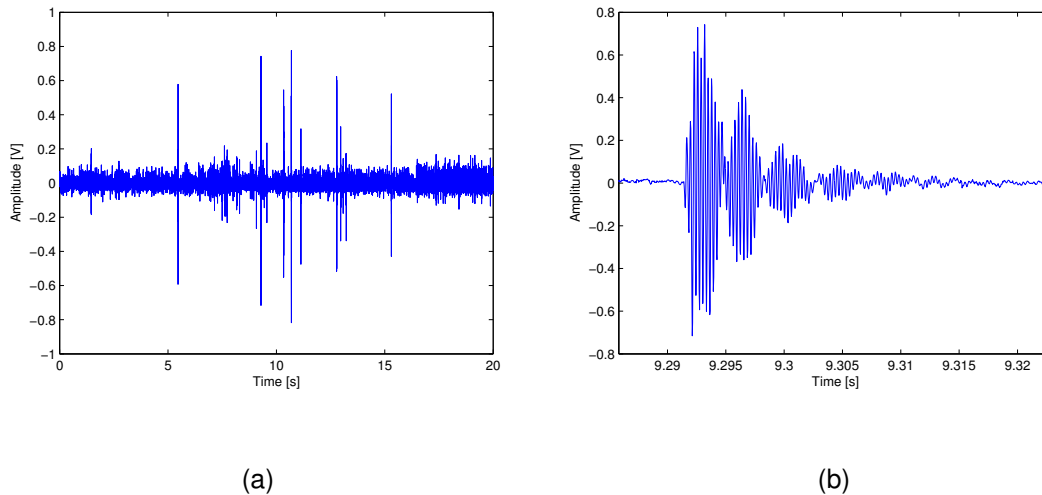
Figure 5.1: (a) output of the forced microleaks (b) zoom of one of the spikes in (a).

Applying the same pulse validation technique as for true bubble nucleations, a large variation in terms of frequency of the microleaks is observed. Since microleaks are nitrogen bubbles released into water, the frequency may vary in a wide range depending on their size and the release pressure. For the particular case of the pulse in Figure 5.1 (b), the recorded signal satisfies the pulse validation filter as for true bubble nucleations, with τ = 17.2 ms; its FFT is however observed to vary in frequency from 2.8 - 3.5 kHz, consistent with a dependence on the microleak size and release pressure, yielding a frequency of 3.43 kHz, as shown in Figure 5.2.
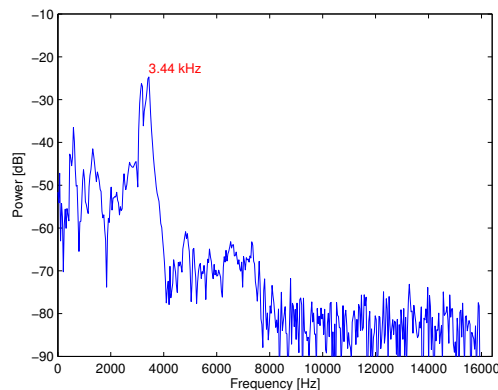
Figure 5.2: FFT of a microleak acquired from the microphone.

5.1.2 Fractures

Occasionally, SDDs exhibit fractures caused by deterioration of the gel (such as with an old detector), or by the nucleation of large droplets that trigger the nucleation of their surrounding neighbours. This was examined with the new instrumentation using SDDs which had been refrigerated at -36ºC over 4 years, and several more recent fabrications in which gel fracturing was deliberately enhanced using more soluble refrigerants such as CF_3I. As shown in Figure 5.3, when a fracture occurs, only one event is generally recorded; the majority of these again satisfied the pulse shape

validation routine, with τ's ~ 36.4 ms. As seen in Figure 5.4, the FFT of the entire fracture however indicates most of the power is at ~ 34.37 Hz, with several harmonics at ~ 400 Hz intervals and a spectrum clearly distinguishable from a true nucleation event.
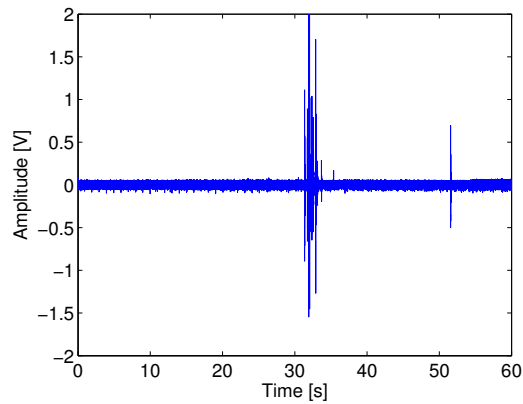
Figure 5.3: signal of a fracture in the gel of a SDD.
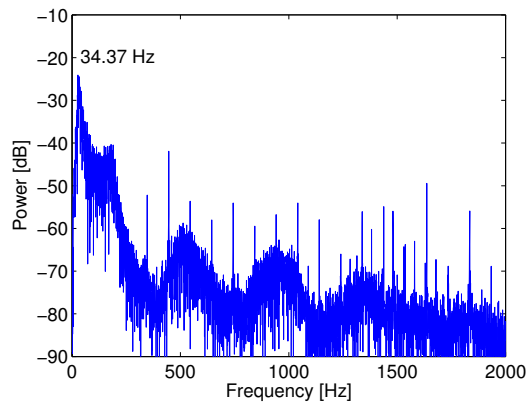
Figure 5.4: frequency spectrum of the fracture shown in Figure 5.3.

5.1.3 N$_2$ Release

Some nitrogen gas may remain trapped inside the gel after the SDD production at 20 bar in the hyperbaric chamber, and then be released to produce a signal when at normal operating conditions.

This was examined using a "refrigerant-less SDD", with no overpressure in order to avoid microleaks. Measurements were performed immediately within the first hour after the "detector" was removed from the hyperbaric chamber. This time, the events such as shown in Figure 5.5 (a) did not satisfy the pulse shape identification routine due to large τ = 90.9 ms; a typical FFT shown in Figure 5.5 (b) is furthermore clearly peaked at ~ 40 Hz with a power level ~ 50% of a true nucleation, and manifests a strongly different spectrum.
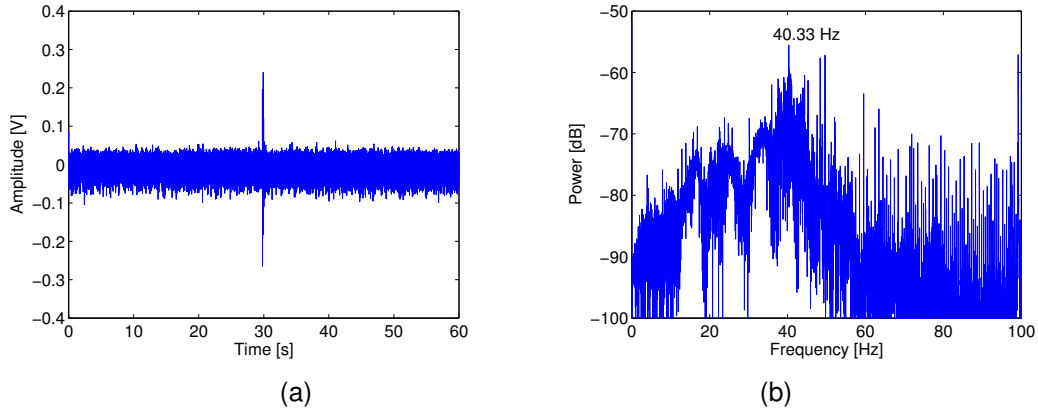
Figure 5.5: typical (a) nitrogen release event from the gel and (b) FFT of the event in (a).

5.1.4 Pressure Release

The search SDDs are normally pressurized up to 2 bar, raising the question of the signal if one of these devices loses its nitrogen overpressure via accident or tube failure.

The test employed a standard SIMPLE SDD, and the pressure was released from the system by de-tightening of the "Staubli" pressure connector. The noise level recorded was 7.0 mV. As seen in Figure 5.6 (a) , there is no resemblance in pulse shape to a true nucleation event; the signal has a sharp rise and rapid decay. Its FFT, in Figure 5.6 (b), has a primary peak at ~ 1 kHz with a time constant of 79.1 ms.
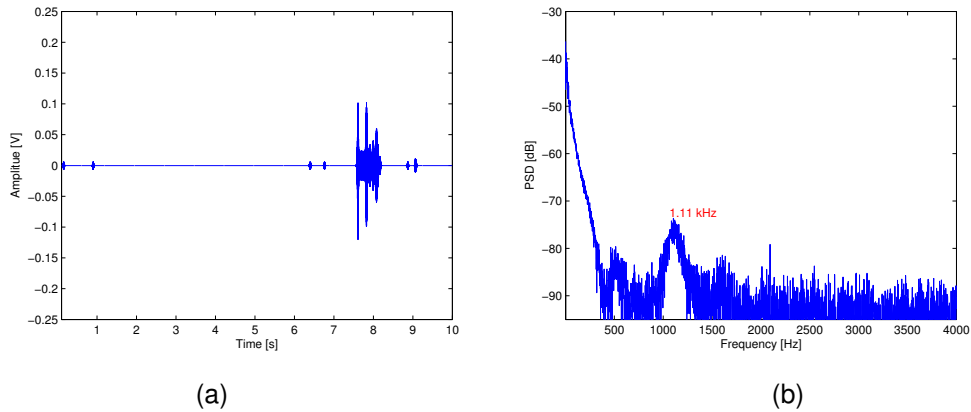
Figure 5.6: (a) event pressure release and (b) its FFT.

The overall results of the background discrimination tests are shown in Table 5.1. The results clearly demonstrate the capacity of the microphone-based instrumentation to distinguish internal acoustic backgrounds commonly associated with SDD operation. The principal frequency associated with each of the acoustic backgrounds presented is clearly different from a true bubble nucleation

event. Most of these background events pass the first stage filter (pulse shape routine), the trapped N_2 and pressure release being the exceptions.

Table 5.1: Comparison of true event characteristics from a CCl_2F_2 SDD with those of several common acoustic backgrounds.

Event type:	Time constants (ms)	frequencies (Hz)	Power level (dB)
True nucleation	5 - 40	450 - 750	- 20±6
Microleak	2 - 60	2800 - 3500	- 25±10
Fracture	2 - 40	10 - 100	- 25±8
Trapped N_2	40 - 100	10 - 440	- 55±3
Pres. release	50 - 100	1000 - 1200	- 70±10

The lower noise levels and higher signal amplitudes of the new instrumentation permits a capability of discriminating nucleation events from acoustic backgrounds common to SDDs.

It is also imperative to map all possible acoustic external noise inside, or in the vicinity of SIMPLE's room at the LSBB. It is expected that the noise levels reduce when the instrumentation for the SDDs is applied in a low noise environment such as LSBB. This is treated in Chapter 7.

5.2 Fabrication Variations

Given the new acoustic instrumentation described in Chapter 4 and its ability to reject acoustic backgrounds either from the detector itself, or from external noise, it is of interest to explore its capacities in observations of the detector response under variations common to its fabrication and operation.

Constructions of Superheated Droplet Detectors (SDDs) are easily (and sometimes unavoidably) altered in the fabrication process by small variations in the ingredient concentrations and fractionating of the superheated liquid. The devices were moreover initially stored at temperatures below 0ºC prior to usage in order to de-sensitize their response during transport. I report studies of the response differences of high concentration SDDs with respect to variations common to their fabrication, to include droplet size, ageing, concentration, gel stiffness and different refrigerants.

The "standard test detector" (150 ml) is a scaled down version of the ~1 liter SIMPLE dark matter SDD, with a uniform dispersion of a few grams of superheated droplets of R-12 (CCl_2F_2) instead of R-115 (C_2ClF_5). The droplets are suspended in a hydrogenated gel matrix composed of glycerin (78.52%), gelatin (1.76%), bi-distilled water (16.10%) and Polyvinylpyrrolidone-PVP (3.62%).

The gel itself is formed by combining powdered gelatin and bi-distilled water with slow agitation to homogenize the solution. Separately, PVP is added to bi-distilled water, and agitated at 60ºC. The glycerin solution is then slowly added to the gel in a detector bottle. Following outgassing

and foam aspiration, the solution is left overnight at 48$^\text{o}$C with slow agitation to prevent air bubble formation.

The detector bottle is then removed to a stirrer/hotplate within a hyperbaric chamber, and the pressure raised to just beyond the vapor pressure at 45$^\text{o}$C. After thermalization, the agitation is stopped and the refrigerant injected into the gel. The pressure is then quickly raised to 19 bar to prevent the droplets from rising to the surface, and a rapid agitation initiated to shear big droplets; simultaneously, the temperature is raised to 45$^\text{o}$C to create a temperature gradient inside the matrix and permit dispersion of the droplets. After 30 minutes, the temperature is slightly reduced for 5 hours (with pressure and agitation unchanged). The refrigerant, in liquid state, is divided into smaller droplets by the continued agitation. Finally, the heating is stopped: the temperature is decreased until the sol-gel transition is crossed, during which the stirring is reduced and finally stopped. The droplet suspension is quickly cooled to 15$^\text{o}$C and left to set for 40 minutes, then cooled to 5$^\text{o}$C where it is maintained for ~ 15 hours. The pressure is then slowly reduced to atmospheric pressure, and the detector removed to cold storage or utilization. The process results in approximately uniform and homogeneous (30±15 μm diameter) droplet distributions, as determined by optical microscopy. Longer fractionating times give smaller droplet diameters; shorter times, larger diameters.

Data on bubble nucleation was obtained acoustically, using the new instrumentation. Data was acquired in Matlab files of ~ 5 MB each at a constant rate of 32 kSps for periods of 5 minutes each.

The detectors were placed in a water bath with its temperature controlled by a stainless steel PT100 probe [H62IKA]. The bath was located inside an acoustic foam cage, constructed for the purpose of environmental noise reduction. Previous studies have shown the CCl_2F_2 device insensitive to γ's, cosmics and minimum ionizing radiations below a reduced superheating of s = $(T-T_b)/(T_c-T_b)$ ~ 0.5 [34], where T, T_b and T_c are the operating, boiling and critical temperatures at a given pressure, corresponding to 41ºC; the gel is observed to begin melting at ~35ºC. Since the SDD sensitivity increases with temperature, the measurements were performed over the range of 15-30ºC in steps of 5ºC. Each temperature measurement required a stabilization time of about 30 minutes. The temperature of each detector was measured with a type *k* thermocouple [RS 219-4450].

The nucleation events were stimulated by environmental radiations. These were once more cross-checked against events generated by irradiating the detectors using a quasi-monochromatic 54 keV neutron beam obtained with a Si+S passive filter at ITN.

The temperature was swept between 15ºC and 35ºC (with some exceptions that will be explained later). The studies were conducted to observe the signal variation with temperature, since these detectors are operated under different thermodynamic conditions, (temperature and pressure), in order to accommodate most of the applications enumerated in the introduction.

5.2.1 Droplet Size

The distribution of droplet sizes depends on the method of preparation of the SDDs [76]. In the process of emulsification of a standard device, where the sensitive liquid is stirred or sheared in the gel medium to form droplets and then superheated by decreasing the pressure to atmosphere, there is a distribution of diameters formed (40% of 30 μm, 5% of 10 μm and 5% of 60 μm). Given this, a study was made to see if the size of the droplets yields differences in the signal response.

Two SDDs were made for this study in addition to a standard. The first one, >DROP, had half the normal time (6 hours) of stirring and half (150 rpm) the normal shearing for a standard SDD, and therefore a distribution of larger diameter droplets (60 μm – 40%). The second, <DROP, had twice the normal stirring time (12 hours) and the same 300 rpm of the normal shearing for a standard SDD; it had a distribution of smaller droplets (10 μm – 40%). This was microscope confirmed for both detectors. All detectors otherwise had similar constructions: the <DROP detector had 4.6 g of CCl_2F_2; the >DROP, 4.0 g and the "standard normal", 2.5 g.

The noise levels for all detectors were similar at ~5 mV, with >DROP about 1.5 x larger than the others. The nucleation signal numbers, shown in Figure 5.7 (a), are similarly about the same despite that >DROP detector has more events at the beginning of the test at 15ºC.

(a)

(b)

(c)

(d)
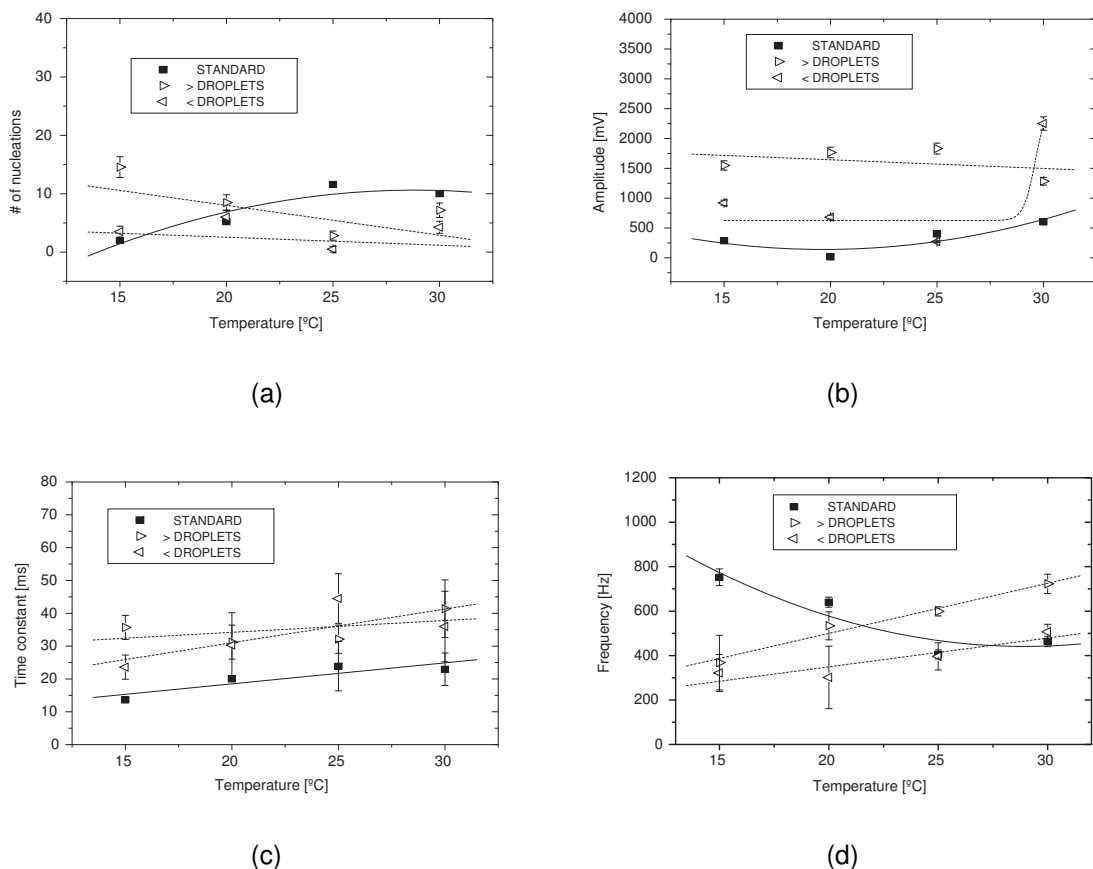
Figure 5.7: variation in signal (a) numbers, (b) amplitudes, (c) time constants, and (d) response frequencies for detectors with different droplet size.

As shown in Figure 5.7 (b), the signal amplitudes for >DROP detector are 1.5-3 larger than the others, which is possibly related to the ~50% larger size of the droplets. The <DROP and standard devices generally behave similarly.

The behaviour of the signal time constants for the three detectors (Figure 5.7 (c) is essentially the same throughout the measurements. Both SDDs with droplet size variations exhibit signals with time constants of 20-40 ms, whereas those of the standard SDD are always between 10-20 ms.

As seen in Figure 5.7 (d), both <DROP and >DROP detectors showed an approximately linear increase of signal frequency with temperature, whereas the standard signal appears to asymptotically decrease to ~500 Hz.

Larger droplets should expand more (order 10x) than smaller droplets, with an accompanying increase in the signal amplitudes. They also imply an increase in the probability of sympathetic nucleations, and further increase in the recorded signal amplitude. Given that the gel is for the most part unchanged however, the pulse dissipation should be relatively unchanged and the time constants more or less constant.

It might be expected that larger droplets scatter more the shock wave, which should lead to an amplitude loss and some frequency dispersion – neither of which is however observed.

Experimentally, the signal amplitudes associated with the large droplet device are uniformly ~ 4x those of the standard, while the small droplet amplitudes are ~2x. Both time constants are slightly larger than the standard device, with the larger droplet device larger than the smaller at lowest temperatures. The recorded frequencies are initially smaller than the standard, with the larger droplets larger than the smaller.

5.2.2 Device Ageing

Previously, the detectors were stored at temperatures below 0°C before they were used, in order to reduce their sensitivity during transport. This test was effectuated to explore the possible response difference between old and fresh devices, since the lifetime of a superheated droplet detector is limited by the fracture of the gel matrix due to the bubble growth in time because of Ostwald ripening [77].

Both SDDs were standard test devices, of a similar constitution: the "fresh" detector had 2.5 g of CCl_2F_2; the "old", 3.9 g of CCl_2F_2. The "old" SDD was kept 60 days in a freezer at –35°C; it was defrosted for 3 hours prior to measurement. Following defrosting, the "old" SDD gel exhibited a different color and consistency than that of the standard "fresh" one.

(a)

(b)

(c)

(d)
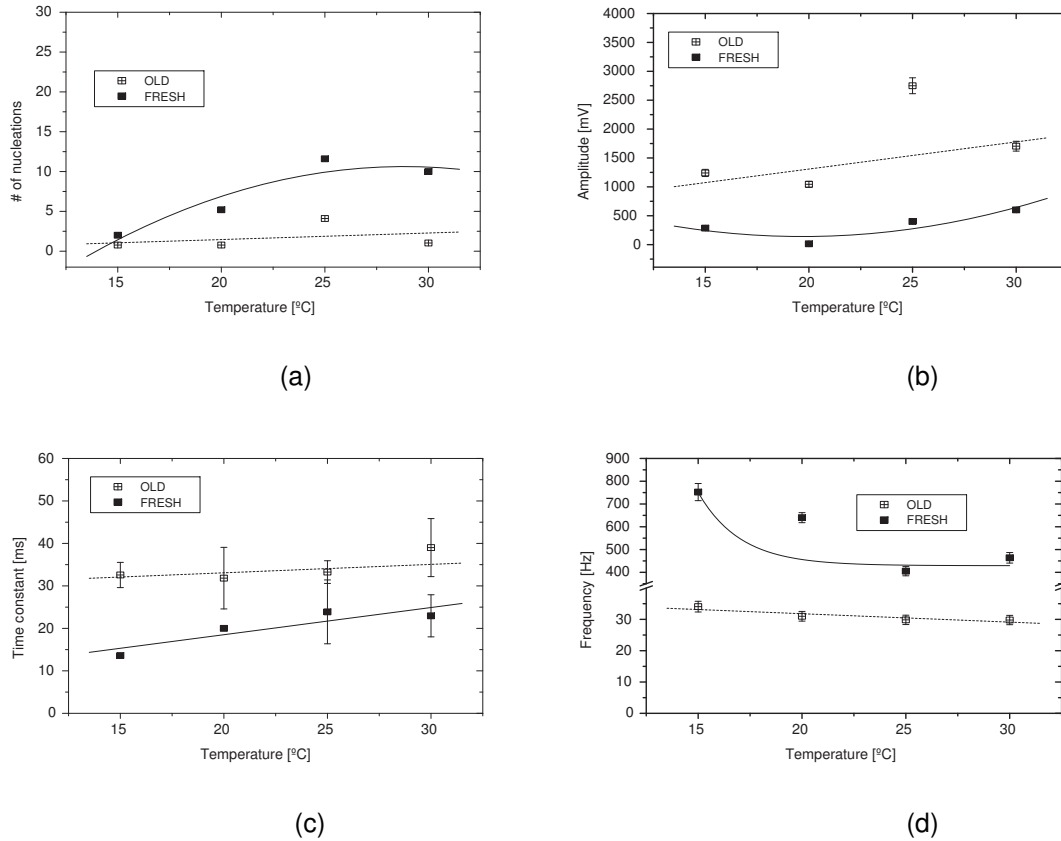
Figure 5.8: variation in signal (a) numbers, (b) amplitudes, (c) time constants, and (d) frequencies in terms of detector age and storage.

There was no significant difference between the two in terms of noise levels, which were generally on the order of 5 mV. The nucleation numbers are generally ~2 times higher with the "fresh" detector, as seen in Figure 5.8 (a), which is somewhat unexpected considering the higher refrigerant mass of the "old" device.

As shown in Figure 5.8 (b), the "old" detector produced larger signal amplitudes than the "fresh". The signal time constants, shown in Figure 5.8 (c), have a similar behavior with temperature, but are 40% larger for the "old" detector, with values characteristic of fractures. The time constants of the "fresh" device are, in contrast, within the range of true nucleation events (Table 5.1).

The frequency variation with temperature is shown in Figure 5.8 (d). The fresh detector response gave a single frequency between 450 and 750 Hz depending on the temperature, whereas the old detector produced a flat ~30 Hz throughout the entire temperature increase. The "old" detector frequency results are characteristic of fractures (Table 5.1), consistent with the observed time constants. This may explain the much larger amplitudes, since a rupture of the gel produces look-alike events but with much larger amplitude.

The gelatin gels at temperatures below 30°C by association of 3 polyelectrolyte chains into a triple helix conformation [78]. Frozen gel is not in an equilibrium state: for storage times > 12 hr, the lower temperature catalyzes the process of gelification and helices continue to be formed very slowly in time, increasing the viscoelasticity of the gel.

The freezing of the SDD also reduces the droplet size, as the Freon continues to dissolve into the gel [78]; the lower the temperature, the more soluble is the detector. The nucleation rate of the "old" detector shows indeed a lower rate than expected and moreover a flat response. In comparison, the curves from <DROPLET and the "old" detectors exhibit more or less the same low counting rate.

Following the measurements with the "old" SDD, optical microscopy of the stored "old" SDD identified a significant presence of clathrate hydrates at low temperature, which tend to "glitter" because of the ice crystal cages encrusting the droplets. Clathrate hydrates are crystalline, water-based solids physically resembling ice, in which small non-polar molecules (typically gases) are trapped inside "cages" of hydrogen bonded water molecules. Their formation and decomposition are first order phase transitions and not chemical reactions; they are not chemical compounds since the caged molecules aren't bonded to the lattice. The clathrate hydrates surrounding the droplets break the metastability as a mechanical action independent of temperature, as if the droplets are "pierced" by the clathrate hydrates and then nucleate.

By comparing the frequency curves of <DROPLET and "old" SDDs, it is seen that the signal frequencies are not the same. The clathrate hydrates surround the droplets like a cage, changing the frequency and producing fractures. The flat frequency and event rate curves with temperature increase evidence the mechanical effect of the clathrate hydrate presence. Their presence implies that the device cannot be stored in a stable liquid phase at temperatures below 0°C because clathrate hydrates provoke spontaneous nucleation locally on the droplet surfaces when warming to room temperature, altering significantly the event frequencies and eventually destroying the device.

It was on the basis of this study and its results that a clean room fabrication site was installed in the LSBB avoiding storage and long transportation.

As previously noted, an increased concentration also leads to an increase in the distribution of droplet size, so that the behavior of >DROPLET and higher concentration devices is similar.

5.2.3 Concentration

Two different detector volumes were employed: an 80 ml and a standard (150 ml). Both had a similar uniform dispersion (standard, 2.5 g; 80 ml, 3.0 g) of superheated CCl_2F_2 droplets suspended in an identical gel, corresponding to filling factors of 1.7 and 3.8 % respectively.

The noise levels of the two detectors were again of order 5 mV, with the noise slightly higher for the smaller SDD, and independent of temperature to within experimental uncertainties.

The number of nucleation events is seen in Figure 5.9 (a) to be slightly larger for the smaller volume detector at temperatures below 25°C, although their behavior is more or less the same with temperature increase. Differences might be the result of the concentration increase, since the small volume concentration is ~50% higher.

(a)

(b)

(c)

(d)
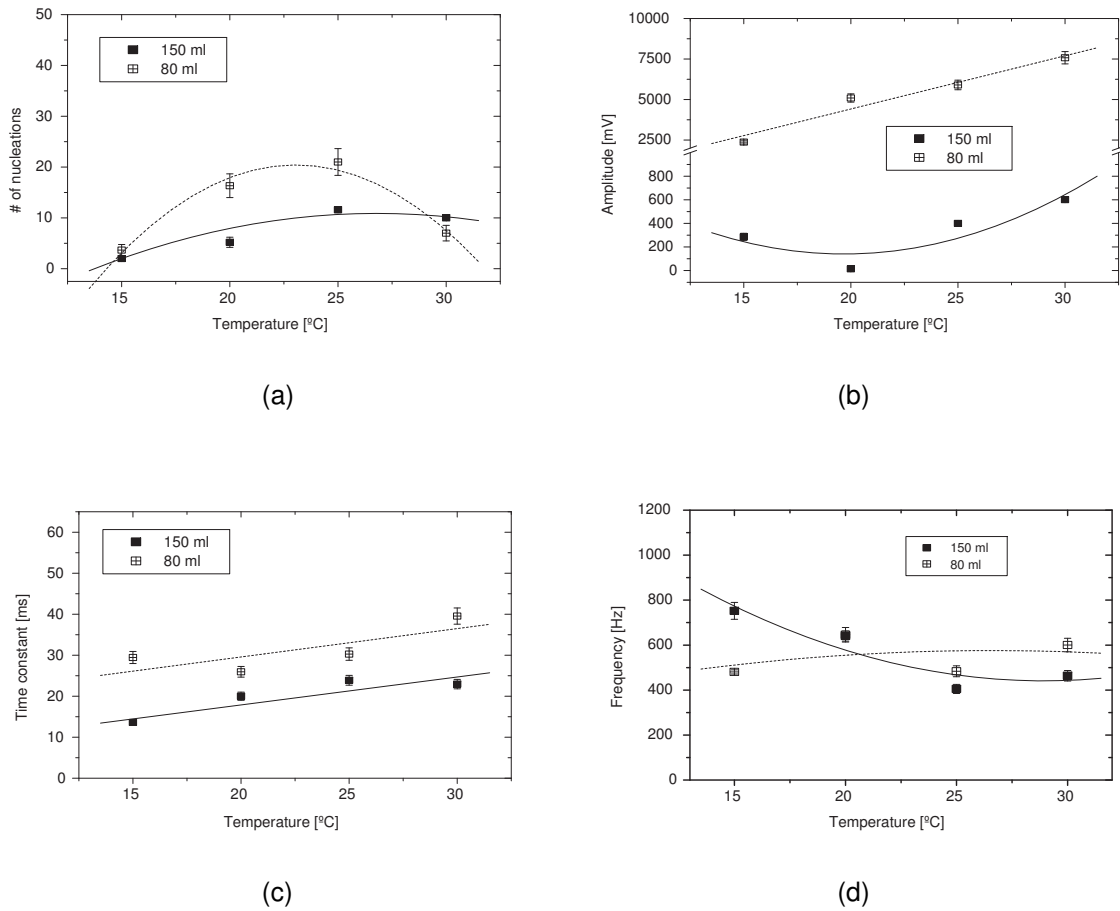
Figure 5.9: variation in signal (a) numbers, (b) amplitudes, (c) time constants, and (d) frequencies for the two detector concentrations.

In general the signal amplitudes, shown in Figure 5.9 (b), increase with temperature as expected for a gel medium increasingly less solid. As anticipated, the amplitudes are larger in the small volume detector than in the standard device. For the standard detector, the amplitudes are low and never rise above 1 V; for the smaller volume device, they begin around 2.5 V at 15ºC and continue to rise in a linear fashion up to ~7 V at 30ºC. This is likely due to less signal attenuation, since there was approximately half of the gel medium in the smaller device.

The time constants of the nucleation signals, shown in Figure 5.9 (c), appear slightly dependent on the volume of the SDD, with those of the smaller volume device around 10-15 ms larger.

The frequency response of the two detectors is shown in Figure 5.9 (d). Only a single principal frequency between 450 – 750 Hz is observed in the larger volume detector at each temperature. For the smaller volume device, the frequency is essentially constant at ~ 600 Hz.

A higher refrigerant concentration implies a decrease in the mean inter-droplet distance, and an increase in the probability of sympathetic nucleation of nearby droplet neighbors. In principle, this leads to a superposition of nucleations and an effective increase in the recorded amplitude. Beyond the increased density of acoustic scattering sites, there is no significant change in the medium and the signal propagation should result in essentially unchanged time constants and frequencies.

Experimentally, the signal amplitude of the higher concentration device is ~10x larger than that of a standard device, with a uniformly increased signal time constant and a generally constant frequency of ~ 600 Hz. The increased 3.8% concentration of the smaller device remains well-below the ~14% percolation threshold of SDDs [79].

The increased concentration also has an impact on the droplet size distribution, which increases, because the droplets coagulate as a result of the saturation of the liquid Freon in the liquid gel during SDD fabrication. Comparing the >DROPLET and 80 ml results, we have the same behavior for Figures 5.7 (b,d) and 5.9 (b,d). The event rate behavior seems the same with a decrease in temperature, due to the larger droplets initially having a higher vaporization probability.

5.2.4 Stiffness

These tests examined the acoustic response to changes in the medium stiffness. Two additional 150 ml detectors were produced for this study using the basic standard recipe, each having the same uniform dispersion of 3.0 g of superheated of CCl_2F_2 droplets, but differing in gelatine concentration: <STIFF had 50% less gelatine than a standard SDD; >STIFF, 50% more.

As seen in Figure 5.10 (a), there are significantly more nucleation signals in the >STIFF detector, suggesting a possible "sympathetic nucleation" of nearest neighbors; the device in fact was spontaneously bubbling on removal from the hyperbaric chamber.

At 25°C, due to the massive nucleation rate, the >STIFF detector was decomposing and no longer serviceable. In contrast, the <STIFF detector did not respond at the lowest temperature. The numbers of nucleation signals in the <STIFF detector are slightly less than the standard SDD.

The signal amplitudes of the three detectors (Figure 5.10 (b)) all display some increase with temperature. The higher amplitudes for the >STIFF detector are consistent with a stiffer gel medium absorbing the acoustic shock waves less.

As seen in Figure 5.10 (c), all time constants behave similarly, with the lowest value recorded for the >STIFF. As the <STIFF gel is more relaxed, the time constants are generally larger. All time constants generally increase with temperature.

Figure 5.10 (d) shows the recorded signal frequencies. All tend to decrease with increase in temperature, with the standard detector single frequency remaining more or less unchanged, except at the highest temperatures.
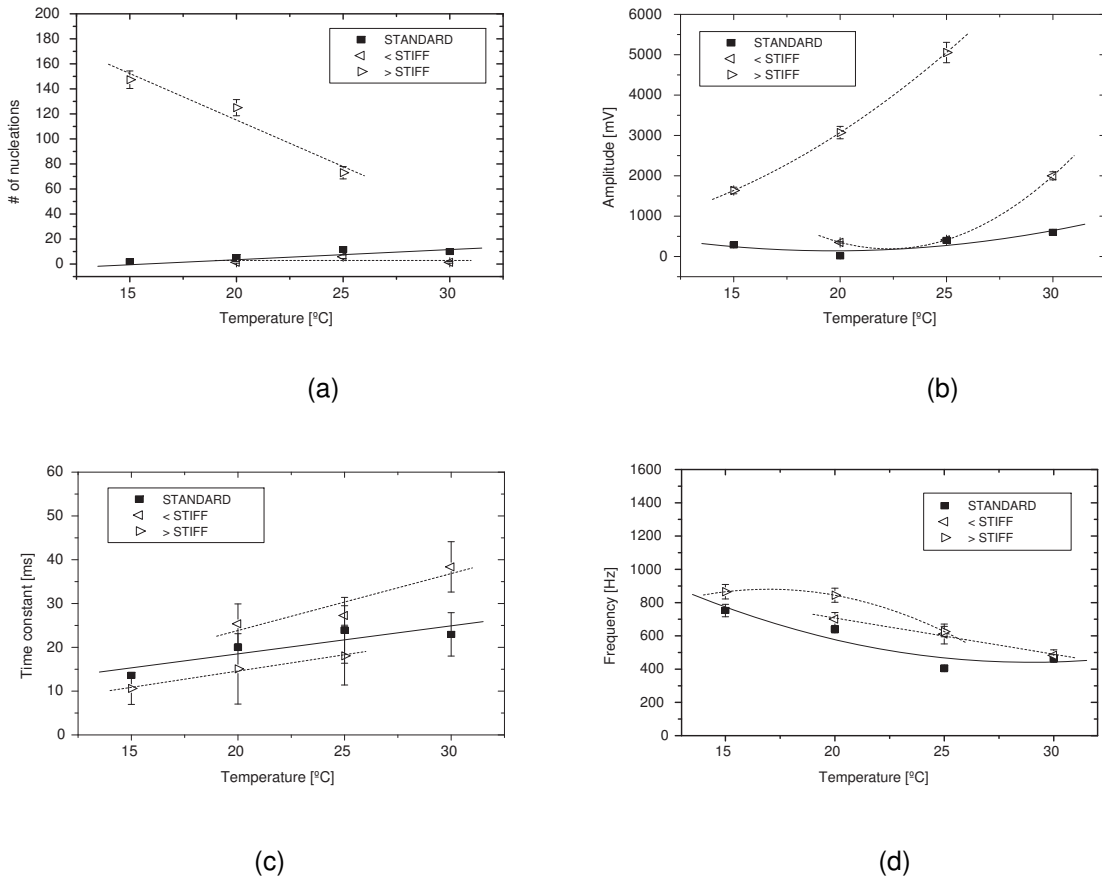
Figure 5.10: variation in signal (a) numbers, (b) amplitudes, (c) time constants, and (d) frequencies for the different detector gel stiffness.

A less elastic gel also implies an increase in the probability of sympathetic nucleations and an effective increase in the recorded signal amplitude, which is evidenced in the observed numbers of nucleation events prior its self-destruction at 30ºC.

From polarimetry measurements, the rate of helix formation $\chi = 0.55$ [77]. Since the helix concentration is $c_{helix} = \chi c_{gel}$ [78,80], we have for the standard gel $c_{helix} = 9.68 \times 10^{-3}$ gcm^{-2} and $c_{helix} = 1.94 \times 10^{-2}$ gcm^{-2} for the >STIFF. The modulus is given by $B = (2.1 \times 10^9)c_{helix}^2$ [77,81], so that the ratio is $B_{>STIFF}/B_{standard} = 121$: by adding 50% more gel (3.52% instead of 1.76%), the gel's stiffness was increased by a factor 100. The nucleation rate is high in the case of the >STIFF, since the droplets are compressed by the gel media: in consequence the radiation-induced nucleation event rate is masked by the stiffness effect. The nucleation rate of the >STIFF device decreases with temperature increase because the stiffness of the gel also decreases. Moreover, as the temperature increases, the viscoelasticity of the gel is lowered since there is a decrease in the helix amount and the gel is becoming more liquid: the droplets are less and less compressed and the event rate decreases, reaching a "normal" rate where the radiation-induced nucleations dominate.

An increased gel stiffness also implies less energy dissipation, and generally smaller signal time constants. Since the refrigerant gas bubble must encounter an increased resistance in expanding against the gel, it seems likely that a stiffer gel should yield slightly higher frequency signals.

Experimentally, the signal amplitudes of the >STIFF device are ~10x larger than those of a standard device, with time constants slightly lower and frequencies slightly larger at the lower temperatures than the standard. For the <STIFF device, the frequency and amplitude are generally those of the standard, with the time constant slightly higher than the standard.

5.3 Different Refrigerants

There are a variety of refrigerants which can be employed in SDDs. In Dark Matter experiments the refrigerants from SIMPLE (C_2ClF_5 and CF_3I) and PICASSO (C_4F_{10}). Since the Spin-Independent cross section generally scales with the squares of both the mass number and the WIMP-nucleus reduced mass, exploring this sector of WIMP interactions suggests a SDD composition with nuclei of a significantly higher mass number. The device construction generally consists of two parts: the gel and the refrigerant. The difficulty here is that device fabrications generally proceed on the basis of density-matching the refrigerant with the gel, and that heavier refrigerants are generally of higher density. The traditional addition of heavy salts such as CsCl to raise the gel density is here discouraged, given that this adds radioactive contaminants which must be later removed chemically. Thus, although several readily available "heavy" refrigerants exist, such as CF_3Br, CF_3I and XeF_4, the problem of fabricating a homogeneous dispersion of the refrigerant, without introducing additional radio-contaminants, has discouraged their development.

The variation of the refrigerant densities with temperature is shown in Figure 5.11. For the higher density refrigerants, the significant difference in gel and refrigerant densities would generally cause the refrigerant droplets to sink during fabrication, resulting in an inhomogeneous distribution of droplet sizes located near the detector bottom.
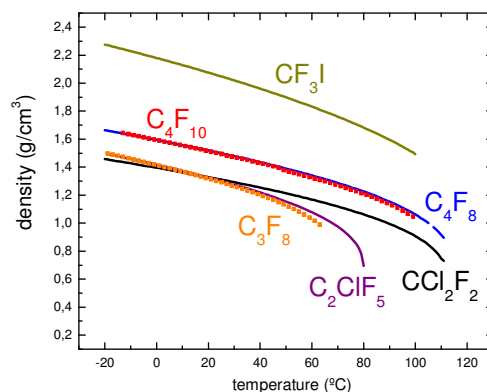
Figure 5.11: variation of refrigerant densities with temperature.

An alternative approach, at least in principle, is to match in viscosity rather than density, as reported for CF_3I [100].

As said before in Chapter 3, the SIMPLE dark matter SDD is generally operated at temperatures and pressures which provide a minimum neutron and α recoil threshold energy.

The basic SDD fabrication process has been described previously [Sec. 5.2]. Here, the detectors were placed in a water bath for temperature control, which was once more located inside an acoustic foam cage, constructed for the purpose of environmental noise reduction. Previous studies have shown the device**s** insensitive to γ's, cosmics and minimum ionizing radiations below a reduced superheating of s ~ 0.5 [86]**;** the gel is observed to begin melting at ~35°C. As the sensitivity increases with temperature, the measurements were performed in the range of 5-40°C in steps of 5°C. Each temperature required a stabilization time for each SDD of about 30 minutes. The temperature was measured with the type *k* thermocouple [RS 219-4450].

These were all cross-checked against events generated by irradiating the detectors using the quasi-monochromatic 54 keV neutron beam obtained with a Si+S passive filter as before at ITN. The results were filtered for acoustic backgrounds and subjected to a FFT analyses.

In general, pressure increase raises the threshold recoil energy curve and shifts it to higher temperatures, as already seen in Figures 3.1 and 4.17 for C_2ClF_5 and CCl_2F_2 respectively.

The threshold also depends on the nucleation parameter "Λ" of the refrigerant. The empirical $\Lambda = 4.3(\rho_V/\rho_l)^{1/3}$ where ρ_v is the vapour pressure and $\rho_l(T)$ is the saturated liquid density of the refrigerant, has been shown to be in agreement with experiment for C_2ClF_5 and CCl_2F_2. Interpretations of these results are being formulated with the following theoretical Harper Factors [78], shown in Figures 3.1, 4.17, 5.12, 5.13 and 5.14, for the several refrigerants.
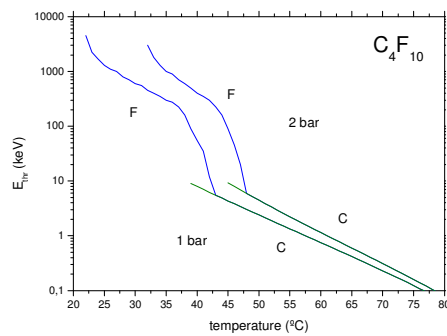
Figure 5.12: variation for the nuclear recoil energy thresholds with temperature for the refrigerant (C_4F_{10}) constituents for 1 and 2 bar response.
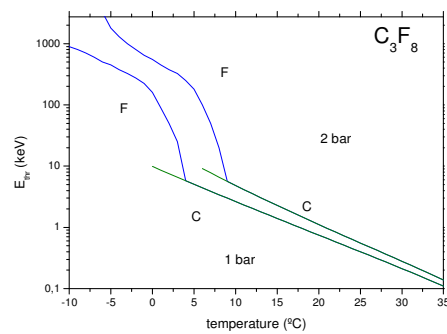
Figure 5.13: variation for the nuclear recoil energy thresholds with temperature for the refrigerant (C_3F_8) constituents for 1 and 2 bar response.
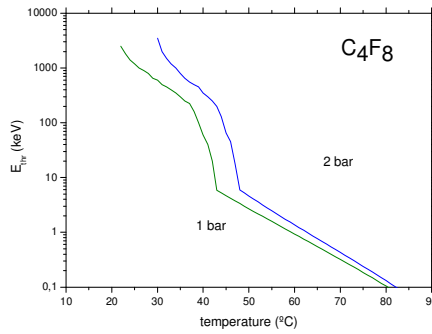
Figure 5.14: variation for the nuclear recoil energy thresholds with temperature for the refrigerant (C_4F_8) constituents for 1 and 2 bar response.

The response comparison of different refrigerants is not straightforward, as seen in previous figures, as a result of their different thermodynamic properties: over the same range of temperature, the response differs as a result of their differing degrees of meta-stability. This should be more obvious in the case of CCl_2F_2 vs C_2ClF_5, where the former is throughout s < 0.5 while the latter is > 0.5.

These thresholds depend on the boiling and critical temperatures of the refrigerant, which as shown in Table 5.2 vary significantly between the materials (refrigerants): different devices may be operated at higher temperatures or pressures.

Table 5.2: Refrigerant critical temperatures at 1 bar; T_b is the boiling temperature, T_c the critical.

Temp./Refrig.	C_2ClF_5	CCl_2F_2	C_4F_{10}	C_3F_8	C_4F_8
T_b (ºC)	-39.17	-29.76	-2.09	-36.65	-6,99
T_c (ºC)	79.90	111.80	113.18	71.95	115,22
S (5-35ºC)	0.37-0.62	0.25-0.46	0.06-0.32	0.38-0.66	0.10-0.34

Distinct types of calibrations have been performed to determine the target mass effectively monitored in the SIMPLE detectors and to check the calculation of the temperature and pressure dependent threshold energy, E_{thr}, above which WIMP recoils can induce nucleations as described in Section 3.2 of Chapter 3.

The response of the detectors with the refrigerants C_2ClF_5 (2.7g), C_4F_{10} (2.6g), C_3F_8 (3.1g), C_4F_8 (2.8g) was compared with the standard test detector CCl_2F_2 (2.5g). All of the refrigerant droplets were suspended in 150 ml of hydrogenated gel (standard size); preparation of each was roughly the same.

Given the variation in thermodynamic characteristics, the reduced superheat factor, S = [(T - T_b)/(T_c - T_b)] was introduced, with T_c, T_b the critical and boiling temperatures of the refrigerant at a given pressure, instead of temperature. This approach normalizes all refrigerants in terms of temperature and has been shown [90] to provide a "universal" curve for the nucleation onset of devices based on different refrigerants.

Table 5.3: Refrigerant reduced superheat factor S for operation temperatures.

T [ºC]	C_2ClF_5 s	CCl_2F_2 s	C_4F_{10} s	C_3F_8 s	C_4F_8 s
5	0,370958	0,245550	0,061508	0,383517	0,098110
10	0,412950	0,280870	0,104884	0,429558	0,139023
15	0,454942	0,316191	0,148261	0,475599	0,179936
20	0,496935	0,351512	0,191637	0,521639	0,220849
25	0,538927	0,386832	0,235013	0,567680	0,261763
30	0,580919	0,422153	0,278390	0,613720	0,302676
35	0,622911	0,457474	0,321766	0,659761	0,343589
40	0,664903	0,492795	0,365143	0,705801	0,384502

The noise levels are equally low among all the devices. For the C_3F_8 detector at 35ºC (S=0.66), however, the noise level was larger since the detector gel was at a point of meltdown and the SDD was sensitive (S > 0.5) to most forms of minimum ionizing radiation for S < 0.5. [90].

The signal amplitudes for all refrigerants, shown in Figure 5.15 (a,b), generally all increase with temperature; only for the CCl_2F_2 at 1 bar and C_4F_8 at 2 bar do they appear to slightly decrease. The signals were acquired with a 60 dB gain. At both operation pressures, the signals amplitudes for C_2ClF_5 and C_3F_8 show a factor 5 to 50 increase relative to the rest of the refrigerants, since they become very rapidly active to all types of radiation and consequently become more sensitive.
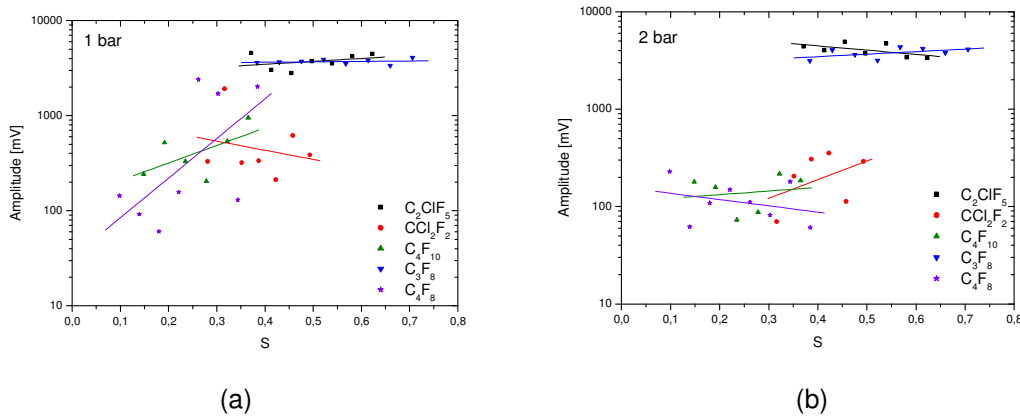
Figure 5.15: (a) 1 bar amplitude nucleation response for different refrigerants; (b) 2 bar response.

The signal time constants are presented in Figure 5.16 (a,b). Generally, all time constants are constant and in the accepted range with the temperature increase, due to a less stiff gel. All of the detectors presented values in the accepted range for true bubble nucleations [5-40] ms.
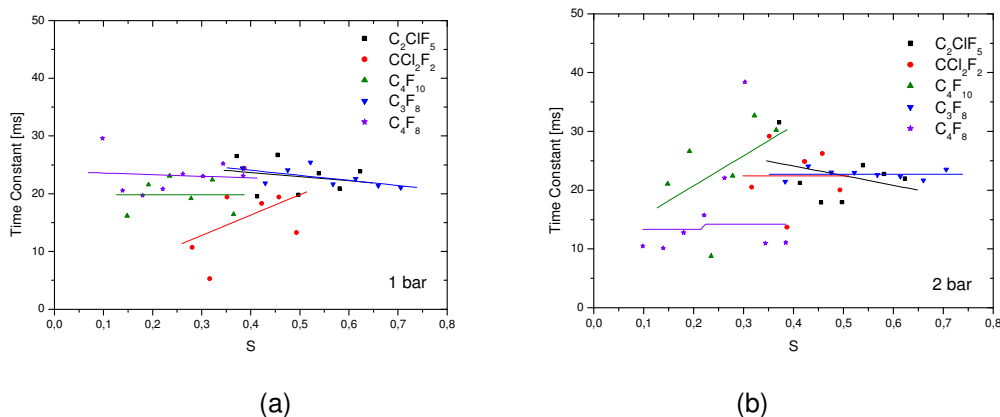
Figure 5.16: (a) 1 bar time constant response for different refrigerants; (b) 2 bar response.

As shown in Figure 5.17 (a,b), all frequencies lie within ~ 0.45 - 0.75 kHz. None of the frequencies are outside of the adopted range for true bubble nucleations.

The frequency of an event is defined by the medium, if any variations should be observed, they would primarily be due to the change of the gel with temperature increase. This was not observed, especially at the point of gel meltdown.
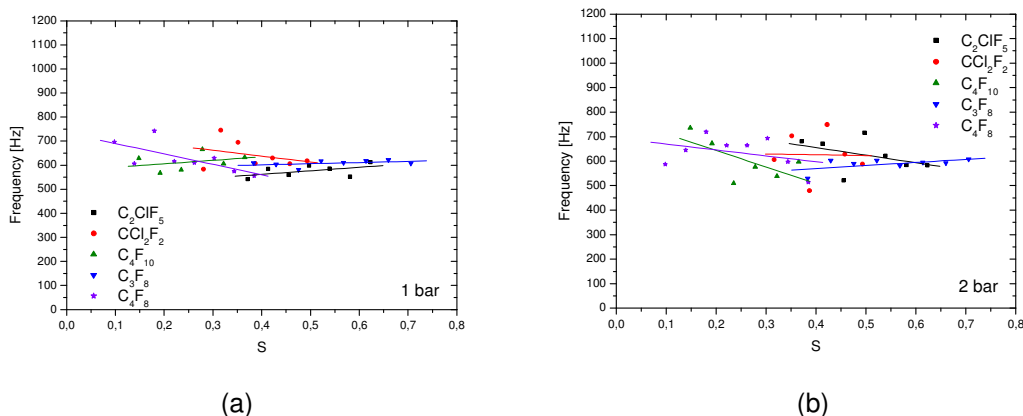
Figure 5.17: (a) 1 bar frequency response for different refrigerants; (b) 2 bar response.

The number of nucleations, as shown in Figure 5.18 (a,b), for the C_3F_8 detector, is significantly larger than the other devices; this is a result of its higher state of superheating for the same temperature. This effect does not appear in such evidence for the CCl_2F_2 device although its critical and boiling temperatures are not that distant from the C_3F_8 and C_2ClF_5 devices. The C_4F_8 and C_4F_{10} detectors, being in lower states of metastability, have fewer nucleation signals.
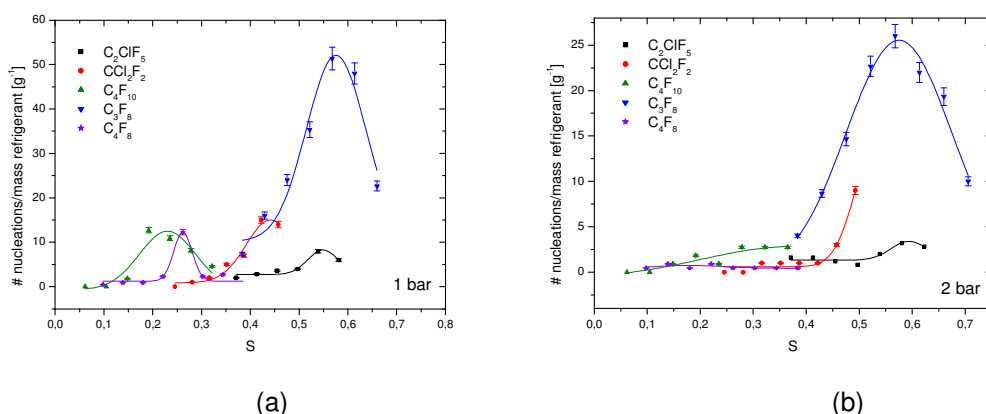
Figure 5.18: (a) 1 bar number of nucleation response for different refrigerants; (b) 2 bar response.

The response comparison of different refrigerants is not straightforward, as seen in Figure 5.18, as a result of their different thermodynamic properties: over the same range of temperature, the response differs as a result of their differing degrees of metastability. This is most obvious in the case of CCl_2F_2 vs. C_2ClF_5, where the former is throughout s < 0.5 while the latter is > 0.5 hence responsive to β and γ interactions.

5.4 Instrumentation and Backgrounds Assessments

The response of SDDs to variations in the standard chemistry of their fabrication which have impact on both the acoustic source and propagation medium, as well as the SDD lifetime has been examined. The results are in general agreement with what might be expected from considerations of both the bubble nucleation and gel medium properties, and show that normal small fabrication variations have a relatively small influence on detector performance.

The noise levels observed in all SDD trials are generally low (~5 mV), and reflect the use of the new microphone-based electronics. A complete power spectrum analysis of the experiment signals was performed, yielding the acoustic event percentages for each of the tests as indicated in Table 5.4. No microleaks were observed in the studies since most of the devices were not pressurized for a long time. The fracture percentage is insignificant for all detectors, with the exception of the "old" detector with ~100 % fractures due to the deterioration of the gel. In the majority of the detectors, less than 1% of the events were identified with trapped gas (N_2), the exception being the <STIFF.

Table 5.4: Acoustic background events in each of the experiments (percentage of total events).

Acoustic backgrounds	Standard	Old	80 ml (higher concentration)	<STIFF	>STIFF	<DROP	>DROP
Trapped N_2	0.8	1	0.3	3.4	0	1.1	1
Fractures	0	99	0	0	0.4	0.4	0.9

The signal frequency is source dependent, which in this case is determined by the pressure shock wave generated by the rapid expansion of the refrigerant gas phase against the gel. As the gel becomes "softer" with increasing temperature, hence less resistant to the expansion, a general decrease in frequency with increasing temperature is to be expected. The source however being a shock wave, there will be an associated disturbance of the gel in its immediate vicinity and effects on the initial wave propagation.

Experimentally, a virtually constant frequency of 450-750 Hz is observed throughout the various experiments, with a tendency to decrease with temperature which can be attributed to the gel softening. The exception is in the variations of droplet size, in which the reverse is seen.

Both the signal amplitudes and time constants are measures of the gel elasticity. The pressure amplitude (p) is given by $p = k\rho_0 v^2 A_m$, where k is the wave number, ρ_0 is the initial pressure, A_m is the maximum amplitude, and $v = [B/\rho_0]^{1/2}$, with B the gel bulk modulus. Although v decreases with temperature increase [82], the increasing gel softness with higher temperatures permits an increase in A_m. Accordingly, both in principle increase with increase of temperature as the gel tension relaxes. Experimentally, apart from small variations, the time constants are essentially constant or slightly increased throughout the study, indicating a virtually unchanged gel consistency over the temperature range of these measurements. The signal amplitudes of the various variations all tend to increase with temperature, as expected.

In general, the sensitivity (number of nucleations) of the SDDs also increases with temperature, since a temperature increase raises the degree of superheat, lowering the energy threshold required for bubble nucleation. The CCl_2F_2 reduced superheat at 30ºC and 1 bar is however 0.42, well below the S = 0.5 onset of SDD sensitivity to electrons, muons, γ's and other minimum ionizing radiations, so that the observed general increase in number of nucleation events cannot be a related result. Larger droplets might also produce a larger number of higher amplitude events due to their larger geometrical cross section.

In terms of detector design, a device providing a temperature-independent amplitude, fast-falling signal pulse with an essentially constant primary response frequency is to be desired. With these criteria, the results suggest that SDD fabrications using a fabrication protocol other than the "standard" are not to be preferred, although minor alterations can be consciously made in order to achieve certain particular results. For instance, the larger droplet results are of particular interest following the recent observation by PICASSO [83] of the possibility to discriminate α from neutron events on the basis of their differing pulse amplitudes, following an increase in their droplet sizes to ~200 μm diameters. The storage of detectors below 0ºC following fabrications is in all cases clearly to be avoided for long periods of time.

Chapter 6   SDD Calibrations and Particle Discrimination

_____

6.1 Bubble Nucleation Process

Until recently, only discrimination of acoustic from particle-induced nucleations has been employed by SIMPLE, given that the acoustical signals were critical for establishing the state of the detector over long-time measurements. PICASSO [83] reported a neutron-α discrimination capability on the basis of the respective signal amplitudes, which they attributed to the difference in proto-bubble formation by incident neutrons and α's to which their high frequency instrumentation was sensitive.

The thermodynamics of a SDD has been described in Chapter 3. The threshold also depends on the nucleation parameter "Λ" of the refrigerant. The empirical $\Lambda = 4.3(\rho_V/\rho_l)^{1/3}$ has been shown to be in agreement with experiment for C_2ClF_5 and CCl_2F_2 [41,79].

The bubble nucleation process can be described [127] in terms of four stages:

(i)   particle interaction with superheated liquid atoms,

(ii)   transition of energy, heating the region around the particle track,

(iii)   emergence of a gaseous phase nucleus (proto-bubble), and

(iv)   growth of the gas bubble.

The proto-bubble must reach a critical radius (r_c), otherwise it collapses back to its original state. If the proto-bubble formation is successful, it serves as an evaporation center for the remaining superheated liquid of the droplet, ultimately releasing its stored energy.

Generally, stage (iv) is observed at low frequency; stage (iii) occurs at significantly shorter time scales hence higher frequency, and is registered by experiments that have used ultrasonic acoustics such as PICASSO and COUPP.

In general, bubble growth starts as described by (a) an initial, surface tension controlled stage, followed by (b) an inertia controlled intermediate stage, which then leads to (c) a heat transfer dominated final phase. The first two stages happen within the first 10 ps before the bubble reaches its critical radius and correspond to stages (i) and (ii) above. During stage (c), the bubble becomes macroscopic in size and its radius increases with time as $R(t) \sim t^{1/2}$. The growth rates exceed several micrometers per microsecond during the first 10μs after nucleation. Since the acoustic pressure wave in the liquid is proportional to the acceleration with which the vapor phase grows [127], rapid bubble expansion contributes substantially to the acoustic signal during the first 50 μs and preserves a memory of the extension of the primary event with a resolution of tens of micrometers. Theory [128]

also predicts that the acceleration of the bubble wall is proportional to temperature, which is consistent with the observed increase in peak amplitude of the neutron- and alpha-induced signals.

6.2 SDD Sensitivity

The radiation response of SDDs has been studied extensively [37,79]. The threshold recoil energy (E*thr*) has a dependence on temperature and pressure.

The two bubble nucleation criteria are thermodynamic [37], so that variation of either temperature or pressure modifies the recoil threshold energy and thus the SDD sensitivity, as seen in Figure 6.1 where the expected variation in threshold recoil energies (E*thr*) of both neutron induced recoils and α's for several operating pressures is shown.

The following equations inflict two thresholds:

$$E > E_c = 4\pi r_c^2 \gamma / 3\psi \qquad (6.1)$$

$$dE/dx > E_c/\Lambda\, r_c \qquad (6.2)$$

The deposited energy E must be larger than the work for the formation of the critical bubble, E_c, and this energy must be delivered in a minimum distance, a minimum dE/dx is required. $r_c = 2\gamma/\Delta P$, where $\gamma(T)$ is the surface tension, $\Delta P = P_V - P$, $P_V(T)$ is the vapour pressure, P and T are, respectively, the operating pressure and temperature, ψ the thermodynamic factor that varies in the range [0.03 0.05] for different liquids [89]. The expression for Λ can accurately predict the observed incident particle at a given temperature for different refrigerants at $P = 1$ and 2 bar.

The α threshold curve shifts to higher temperatures with increasing pressure. Since the curves depend on Λ [37], comparison of experiment and theoretical predictions with varying Λ confirmed SIMPLE's measurements [79] of $\Lambda = 1.40 \pm 0.05$, yielding no α-sensitivity whatsoever above 2.30 bar as observed experimentally at 9ºC.
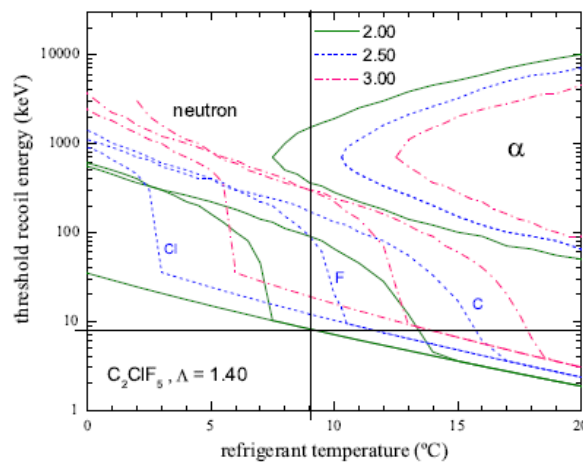
Figure 6.1: variation of the recoil and α energy thresholds with temperature for the three C_2ClF_5 constituents at 2.00 (solid), 2.50 (dash) and 3.00 (dash-dot) bar, with $\Lambda=1.40$. The freon constituents are identified for 2.5 bar. The vertical line indicates the 9ºC measurement temperature; the horizontal line, a threshold recoil energy of 8 keV.

This is then used in calculating the ion recoil energy, for pressures $\leq 2.20 \pm 0.05$ bar, the threshold recoil energy at 9ºC remains below 8.0 ± 0.3 keV for Cl and F nuclear recoils.

The double-validness of the α curves results from the Bragg peak in the energy loss by ionizing electrons along its path, as shown in Figure 6.2.
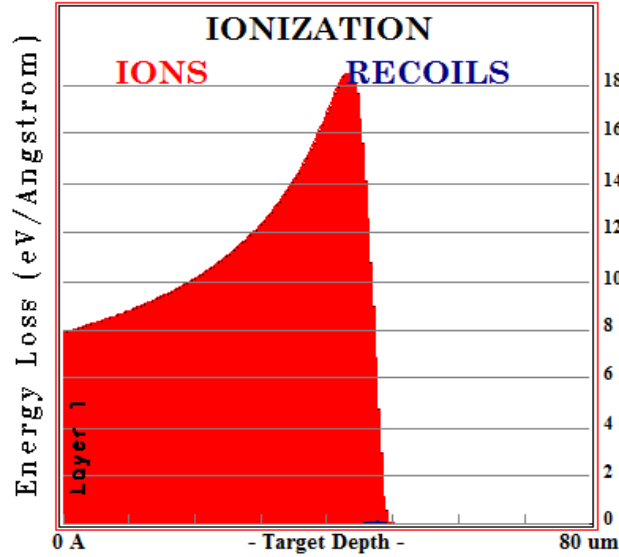
Figure 6.2: α energy loss in C_2ClF_5, for a [241]Am α.

The energy loss of α's and neutrons in a droplet is not entirely different. For neutrons, the main mechanism is elastic scattering on one of the target nuclei, providing a maximum energy for the incident neutron energy to the recoiling nucleus [127]. In contrast, α's may in fact be considered as recoiling [4]He nuclei, the difference being the significantly larger kinetic energy as a result of their decay origin.

For neutrons, there is a further contribution in C_2ClF_5 from the Cl(n,p) S reaction by thermal neutrons, with ~10 x less probability and yielding a S recoil with maximum 17 keV recoil energy by the stopping power of each element.

6.3 Bubble Nucleation Efficiency

The bubble nucleation efficiency of an ion of mass A recoiling with energy E_{dep} is given by the theoretical superheat factor [101]:

$$\eta^A(E) = 1 - E_{thr}^A / E_{dep} \qquad (6.3)$$

E_{thr}^A can be set as low as 6.5 keV before onset of the Cl sensitivity at ~15ºC. As evident from Figure 6.1, at temperatures above ~ 13ºC, the E_{thr}^A and η^A are the same for fluorine, carbon and chlorine;

whenever all recording ions stop within a pressure- and temperature-dependent critical distance, E_{thr}^{A} and $\eta^{A}(E)$ do not depend on A.

The nucleation efficiency however depends on the statistical nature of the energy deposition and its conversion into heat. Recent results of the PICASSO experiment [102], based on the extensive neutron irradiations and Monte Carlo simulations, and refined reanalysis from SIMPLE have indicated a nucleation efficiency of the form:

$$\eta^{'}(E) = 1 - \exp\left[-\Gamma(E/E_{thr} - 1)\right] \tag{6.4}$$

with $\Gamma = 2.5 \pm 0.2$.

A careful reanalysis was made of Phase I [68] monochromatic neutron (24 and 149 keV) irradiation data taken as a function of temperature, using both efficiencies. As expected, this yielded results in a better agreement with Equation 6.4 than 6.3, with $\Gamma_{SIMPLE} = 4.2 \pm 0.3$. Figure 6.3 shows the reanalysis of the previous monochromatic neutron irradiations.
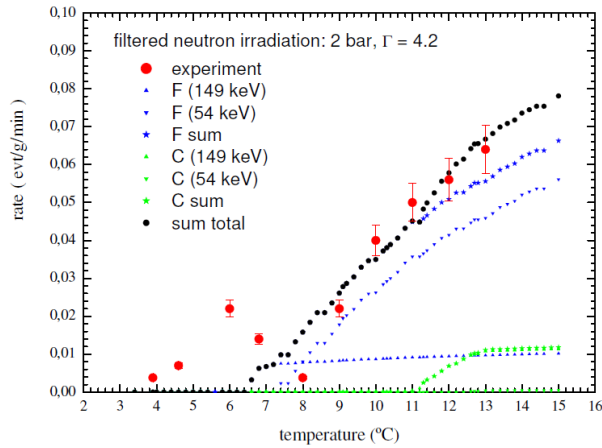
Figure 6.3: new nucleation efficiencies for SIMPLE with $\Gamma_{SIMPLE} = 4.2 \pm 0.3$.

Γ is a detector-dependent parameter, essentially characterizing the slope of the curve above the threshold recoil energy. The differences observed between PICASSO and SIMPLE are related to the nature of the detector fabrication materials. The effect of the difference is seen in Figure 6.4.
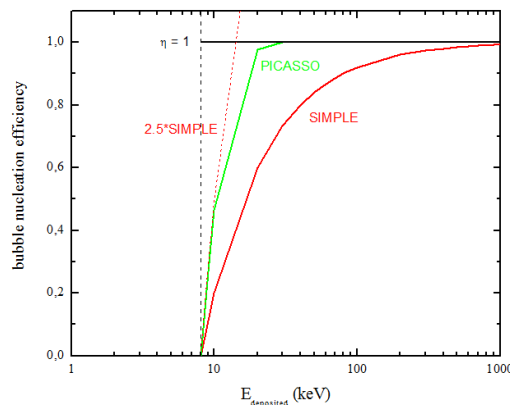
Figure 6.4: comparison of the nucleation efficiencies given by Equations 6.3 and 6.4, as described in the text.

6.4 SDD Longevity

The Phase I SDDs were only stable over ~ 40 days of continuous exposure, which was however conservatively adopted for devices without PVP in the fabrication on the basis of signal avalanches which began to appear in the detectors after 40 days, essentially due to fractures and their propagation which the earlier instrumentation was unable to discriminate from bubble nucleations.

The "rapid aging" process is slowed by the addition of PVP which increases the required gel fracturing energy and viscosity, strengthening the gel matrix while further reducing the already low solubility of the C_2ClF_5. Studies on the increase of SDD lifetime and fracture reduction via use of PVP of various polimerization indices, and other additives have been conducted [77,78]. These studies included numerous neutron irradiations, which later were extended to include weak sources in the development of gel recipes for long-lived SDDs based on refrigerants other than C_2ClF_5 [100]; while not directly examining the SDD longevity, these explored the rate of fracture occurrence with recipe variations.

The SDD lifetime is naturally increased if the device is only weakly irradiated [78, 79], i.e. the number of bubbles which can grow into fractures is small (it is in fact for just this reason that the SDDs are not irradiated before or during DM measurements, but rather monitor the state of the each SDD electronically). Prior to Phase II of SIMPLE, all SDD fabrications were made in a Paris laboratory, which engendered the overland transportation of the SDDs to the underground experimental site in a state of "suspended animation". Analysis of this transport, indicated deleterious effects on the fabrications, to include installation in less than pristine condition (ie. with fractures, bubbles), and the formation of clathrate hydrates [1] which provide surfaces for bubble formation when being warmed to the device operating temperature of $9°$ C: Since the 210 mwe underground clean room within the LSBB was constructed, and the SDD fabrications relocated, substantial subsequent changes in the detector performances, including the absence of clathrate hydrates have been achieved. Just previous to Phase II, a run of 109 days with the C_2ClF_5 SDD fabricated with the standard protocol and submerged to the centre of the water-pool at 1500 mwe, resulted in a loss of detection stability only in the last two weeks of the run, and an operational lifetime increase of ~ 2x. Naturally, fractures resulted from the Ostwald ripening of the bubbles, ultimately led to the performance degradation but at a significantly reduced rate.

Naturally, the SDDs are inspected at the end of their runs, and have shown no increased transparency nor change in gel coloration, thus not suffering from any active volume depletion.

6.5 Particle Discrimination

In calibrating SDDs, important and applicable results were found. A patent discrimination is seen between neutron and α particles through calibrations. For comparison purposes in what follows, the results displayed in Figure 6.5 with *A* being the pulse amplitudes in mV. These were obtained at 2 bar and 9ºC using two different, standard versions of the SIMPLE SDD, each identical in composition but differing in volume. The neutron calibrations were obtained with a large (900 ml), run version SDD exposed to a weak source of Am/Be neutrons at a distance of 15 cm in a water bath. The α calibrations were made with a similar but with a smaller volume (150 ml) device, injected with a dilute solution of U_3O_8.
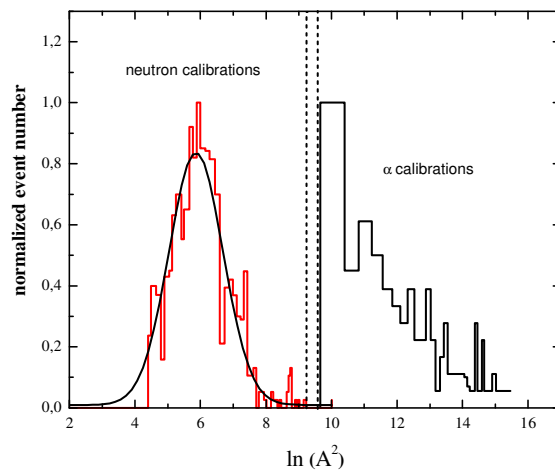
Figure 6.5: initial neutron – α discrimination as reported in Ref. [103].

The acceptance windows for nuclear recoils and α events are determined from the observed device responses. As seen in Figure 6.6 the recoil response is Gaussian with σ = FWHM/2.355 = 0.80, so that an acceptance cutoff $ln(A^2)$ = 9.4 lies 4.4σ above the distribution's mean. The α-acceptance is similarly defined as $9.5 \leq ln(A^2)$, which is separated from the recoil window by 30 mV, or 15σ with respect to the DAQ resolution (0.3mV).

The distribution of recoil window event amplitudes is fundamentally connected to the distribution of freon droplet sizes in the SDD, since the nucleation of a bubble provides the acoustic pressure wave signifying its occurrence. The size distribution is a function of the fabrication protocol, and depends on the ingredients, the amount of injected Freon, fractionating time and speed. The standard fabrication protocol results in a typical distribution of droplet sizes shown in Figure 3.4. The distribution is approximately Gaussian (mean=31 μm, sigma=11), and > 5σ contained below radii of 86 μm.
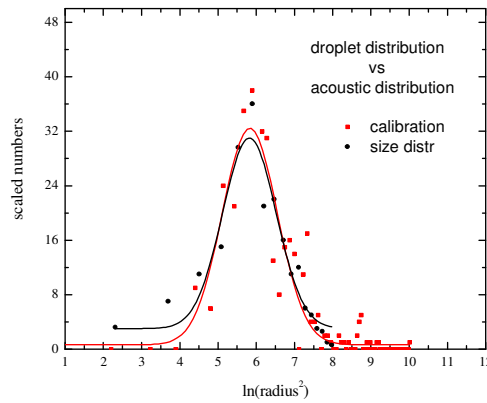
Figure 6.6: overlay of the droplet size distribution with the observed recoil event distribution of Figure 6.5, assuming radius ⇔ amplitude and with adjustments only in the numbers and location of the mean.

The droplet radius, perhaps coincidentally, mirrors the signal amplitudes. Rescaling only the event numbers and shifting the distribution mean by 0.91 yields Figure 6.6, overlaid with the recoil distribution amplitude distribution of Figure 6.5.

6.5.1 Experimental Disposition

All detectors in these calibrations were 1/6 volume versions of the standard SDD utilized for the dark matter search experiments. Two were fabricated according to the "standard" fabrication protocols [129] with the chemistry scaled for detector volume to provide identical size (<r> ~ 30 μm) distributions and concentrations. A third SDD was fabricated with a droplet size distribution ~ twice larger (<r> ~ 60 μm) than "normal", and a fourth SDD 50% more gel (3.52% instead of 1.76%) to increase the gel's stiffness by a factor 100.

Each SDD was instrumented (surface mount display of the associated electronics and all system electromagnetic shielded yielding low noise) with the same PGA2500 preamp and the electret microphone (MCE-200). The acoustic instrumentation, with a timing resolution of 1.6×10^{-2} ms and voltage resolution of 2 mV, was operated at the same sampling rates as of the DM experiments (8kS/s) and had the same unit gain.

The first "standard" SDD was injected with the U_3O_8 solution and measured, then irradiated with neutrons from the reactor thermal column. The second, in contrast, was first neutron-irradiated, this time shielded by 2 mm cadmium to remove the thermal neutrons, and then injected with the U_3O_8 solution. Similarly, the "large droplet" SDD was first U_3O_8 injected, then neutron-irradiated; the sequence was reversed for the "stiff" detector.

The U_3O_8 injection quantity was 15.0 ± 0.5 ml in each case, corresponding to 9.37 ± 0.16 Bq/ml of α activity; detector responses were recorded for periods of up to ~24 hours, the exception being the "stiff" detector that lasted only 4 hours due to a massive nucleation rate which ruined the detector. Alphas measurements were made using a shielding cage (2 mm of cadmium, 10 cm paraffin

and 5 cm PE) surrounding the SDDs. The neutron irradiations (1 hour) were performed on the reactor thermal column, without filters and only a minimum water thickness required for detector cooling. All measurements were performed with the SDDs at 9ºC and 2 bar. The SDDs had 2.4 g (standard unshielded), 2.3 g (large drop), 2.3 g (standard shielded) and 2.3 g (stiff) grams of active mass.

Following each measurement, an initial data set was formed by passing the data files through the pulse validation routine which tagged signal events if their amplitude exceeded the noise level of the detector by 2 mV. All signals with less than five pulse spikes above threshold were rejected, since they do not form a pulse and are electromagnetic noise. The signal waveform, decay time constant and spectral density structure of the remaining single events were next inspected individually. As said before, a particle-induced nucleation event possesses a characteristic frequency response, with a time span of a few milliseconds, a decay constant of 5-40 ms, and a primary harmonic between 0.45-0.75 kHz; this response has been shown to differ significantly from gel-associated acoustic and local acoustic backgrounds.

6.5.2 Standard SDD Response

Figure 6.7 displays a histogram of the signal amplitudes for each of the identified particle-induced signal events in the case of the "standard" SDD with an unshielded experiment at the thermal column irradiation. The amplitude gap between the respective signals seen in Figure 6.5 is not apparent. Additionally, although the width of the neutron Gaussian is about the same as previous, its centroid has shifted upwards by ~ 1.8. The α distribution exhibits about the same form as in Figure 6.5, but the lower edge has shifted downward by ~ 1.5. The event calibration numbers were as follows: (2017 neutrons; 1262 alphas).
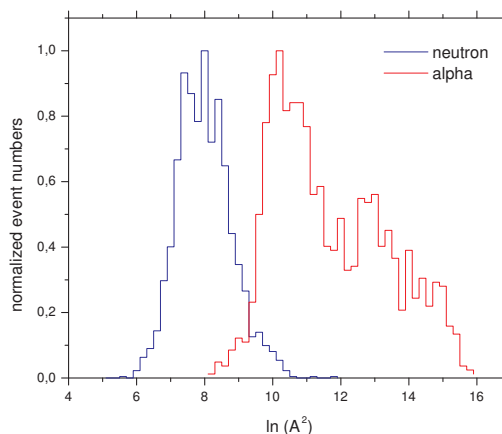
Figure 6.7: histogram of the squared amplitudes of the primary harmonic for neutron and α calibration events, showing no gap between the two measurement populations.

The results of the second "standard" detector irradiations, with the experiment cadmium-shielded at the thermal beam and reversed irradiation sequence, are shown in Figure 6.8. All neutron events are seen to occur with amplitudes ≤ 100 mV - there are two above, well below those of the α events as indicated in initial results of Figure 6.5. The width of the neutron Gaussian is decreased to ~0.8, but its centroid remains above seven, as in Figure 6.7. The alpha events in contrast exhibit the rapid low A cutoff, as in Figure 6.5.

The event calibration numbers were as follows: (1280 neutrons; 867 alphas).
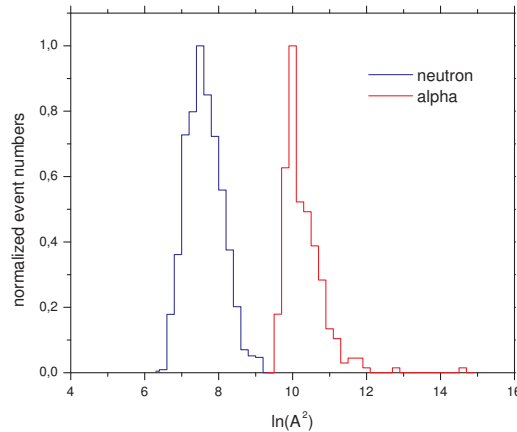
Figure 6.8: histogram of the squared amplitudes of the primary harmonic for neutron and α calibration events, with the thermal neutrons shielded by 2 mm of cadmium.

6.5.3 Large Droplet SDD Response

The histogram for the "large droplet" detector irradiations, with unshielded thermal neutrons following the U_3O_8 injection, is shown in Figure 6.9.
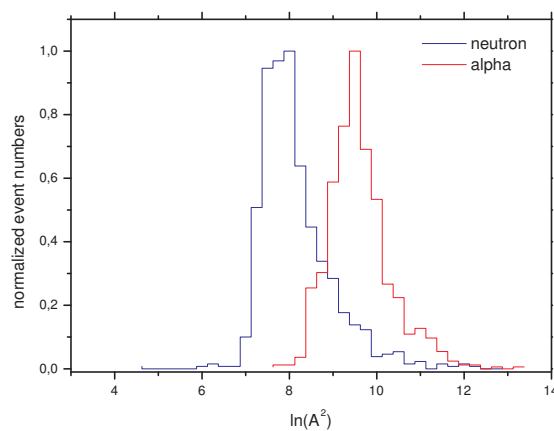
Figure 6.9: histogram of calibration neutron and α amplitudes, large droplet distribution.

As evident, there is no gap between the two distributions. The neutron distribution is moreover no longer well fit by a Gaussian: the "centroid" is now shifted to slightly above 8 with a truncated low amplitude tail, and a high amplitude tail well into the α distribution. The α distribution no longer manifests a sharp amplitude cutoff, but tails well into the low A neutron region in a Gaussian fashion. The event calibration numbers were as follows: (770 neutrons; 598 alphas).

6.5.4 Stiff SDD Response

Figure 6.10 shows the results of the irradiations of the SDD prepared with the stiffer gel. Both distributions are significantly shifted to higher amplitudes, and although possessing an initial well-described Gaussian, have large high A tails due to the massive nucleation events, that effectively destroyed the detector. The neutron events seem again to be truncated at lower amplitudes. The event calibration numbers were as follows: (803 neutrons; 367alphas).
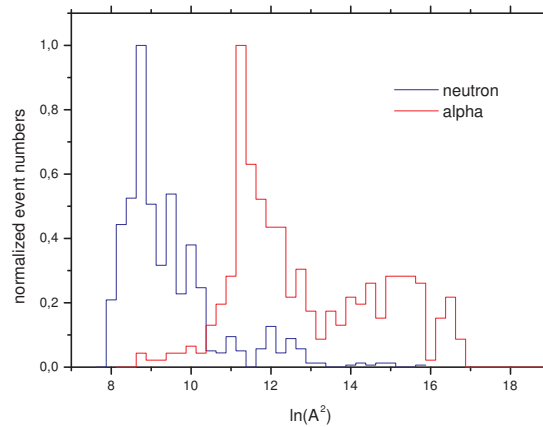
Figure 6.10: histogram of calibration neutron and α amplitudes, stiffer gel.

A summary of the results is shown in Table 6.1.

Table 6.1: Summery of results from the various calibrations.

Ref	peak - n	n - width	peak - α	α width
Fig. 6.5	5.9	1.0	10.0	-
Fig. 6.7	7.9	1.7	10.2	1.8
Fig. 6.8	7.5	1.0	10.0	-
Fig. 6.9	7.9	0.9	9.5	1.2
Fig. 6.10	8.7	0.7	11.2	0.7

The apparent shift of the neutron distribution in Figure 6.8 from that of Figure 6.5 is a result of the smaller SDD size, and pressure wave attenuation. The mean of the sound distance in the latter was ~5 cm, vs. the 4 cm of the former, yielding an amplitude increase of ~20% to a peak at 7.5.

The differences in Figures 6.7 and 6.8 with the "standard" detector irradiations reflects the prudence which must be respected in any such calibration experiments. In the case of Figure 6.7, the α measurements were performed in a pure unshielded surface location: during the measurements, any number of background neutrons were recorded which, if Figure 6.2 is to be believed, would provide a low amplitude contribution to the indicated "α distribution". During the neutron calibrations, the presence of the low activity U_3O_8 would continue to manifest itself in a higher α contribution to the "neutron distribution". This is not seen in Figure 6.8.

As evident, the previous "gap" results of Figure 6.5 are recovered when the neutron irradiation is predominantly non-thermal and the U_3O_8 injection performed afterwards. The sharp cutoff in the low-A α distribution, becomes Gaussian with increase in the droplet size distribution and which softens with the stiffer gel, is attributed to the Bragg peak in the α energy loss spectrum. Only the α's in the head of the peak are capable of stimulating a nucleation event, implying a minimum 40 μm distance within the droplet.

Following previous studies (which however had electronic gain - Chapter 5) with different size distributions, the amplitudes of the big droplet nucleations are generally larger than the normal sized distributions, with larger time constants. Similarly, signal amplitudes in more stiff gels [129] are significantly larger (1500 mV) than with the normal gel (~500 mV). The time constants are correspondingly smaller, with small shifts to higher frequencies.

The measurements with a larger droplet distribution and stiffer gel matrix were performed to observe the effects on the particle-discrimination response to detectors used like PICASSO [83] with a distribution of larger droplet sizes (<radius> ~ 100 μm) and a stiffer polyacrylamide gel than SIMPLE. The results confirm their previous outcomes and corroborate the reason being that the "standard" device <r=30> is near the Bragg peak of the α energy loss and yield a more clean division.

A neutron elastic scattering with one of the refrigerant nuclei yields a single proto-bubble, in contrast to the creation of multiple proto-bubbles by an α trajectory. Each proto-bubble is formed on time scales much less than for a complete nucleation event, each serving as an evaporation center for the bubble nucleation. The enthalpy released in a bubble nucleation triggered by α thus occurs on a time scale reduced relative to a neutron scattering by the number of proto-bubble formations. The increased power provided to the bubble expansion against the gel enhances both the frequency and amplitude of the associated pressure wave.

The power is $(P_w) \sim A^2$. For the same size droplet, the work done by bubble nucleation ($\Delta E = P_w \Delta t$) by either α or neutron inducement is the same, and $A^2_n \Delta t_n = A^2_\alpha \Delta t_\alpha$ where A_k is the respective signal amplitude and Δt_k the droplet evaporation time. Since the minimum distance over which the necessary dE/dx must occur is ~ 0.05 μm in C_2ClF_5, and the maximum width of the relevant α Bragg peak ~ 10 μm (Figure 6.2), ~ 200 proto-bubbles could be formed by an α interaction. Via the same considerations, a neutron-induced event is capable of ~ few proto-bubble formations per interaction (a

result of the significantly lower recoil energies of the C_2ClF_5 nuclei). Since each proto-bubble constitutes a "burn center" for the droplet evaporation, $t_\alpha < 0.01\ t_n$ and the power ratio $A^2_\alpha / A^2_n > 100$.

In summary, this series of measurements using calibrated α and neutron irradiations confirms the ability of the standard SIMPLE SDD to distinguish both event types acoustically. The droplet size distribution provides a natural lower cutoff to the α dE/dx, and is responsible both for the amplitude gap between the α and neutron populations, and the spectral asymmetry in the α power distribution.

When varying one or more of any parameter (gel, droplet size, stiffness, concentration, refrigerant, temperature, pressure, etc) of the SDD fabrication protocol it is clear that the distinct particle discrimination can, or is lost.

Chapter 7   The SIMPLE Phase II Experiment

_____

7.1 Introduction

SIMPLE is sited in the LSBB, located in Rustrel, a small village in the Pays d'Apt, east of Avignon, in the heart of Provence (southeast France). Marseille-Marignagne is the nearest international airport, roughly two hours from Rustrel.

The village is just south of the Plateau d'Albion, the former location for the ground-based component of the French nuclear strike command. The military selection of this location was due to the low density of population, good rock quality, and the existence of mountains for natural protection. Missile silos were spread over several kilometres, with two underground launch control sites on both sides of the Mount Ventoux.

One of these sites was spared from destruction and converted to a laboratory (LSBB), The LSBB consists of 3.2 km of reinforced concrete galleries with various halls (Figure 7.1).
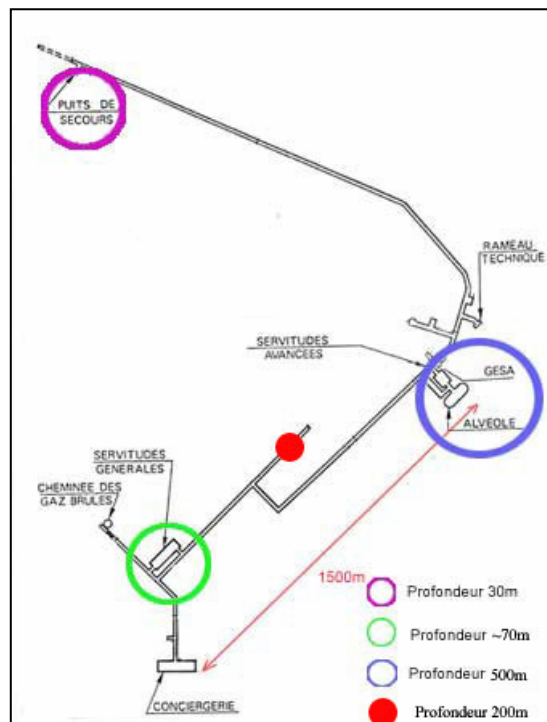
Figure 7.1: LSBB underground galleries [60].

Two major experimental halls are available; the shallowest, Servitudes Generales (350 m^2, 7 m ceiling height, 50 m rock overburden), is located 400 m from the entrance and is shielded in the same manner as the launch control room (1 km further down, protected by 500 m of calcite rock). The

shallowest hall hosts SIMPLE's clean room for detector production, and the deepest hall GESA, which is a Faraday cage, hosts the experiment.

There is also a control room in the second hall. The room is entirely surrounded by a horizontal steel capsule 28 m long, 8 m in diameter and 1 cm thick; entrance doors are clamped by electrical contacts to ensure the sealing of this second peculiar Faraday cage. External and internal steel doors can bear 20 bars of overpressure and emergency generators respond in a tenth of a second to energy supply perturbations.

The entire area is fully ventilated and local road traffic is rare in the vicinity of the laboratory. The geological area of Rustrel has been well-studied. It is at the center of a 30 km circle free of active faults.

7.2 Radiation and Natural Radioactivity

7.2.1 Neutrons

The depth in meters of water equivalent is roughly a factor 3 of the depth of any underground laboratory. GESA and the surrounding rooms are at a depth of ~1500 meters water equivalent (m.w.e.), not one of the deepest when compared to other underground laboratories in terms of muon attenuation. In Figure 7.2 one can see the reduction of the muon flux with depth.
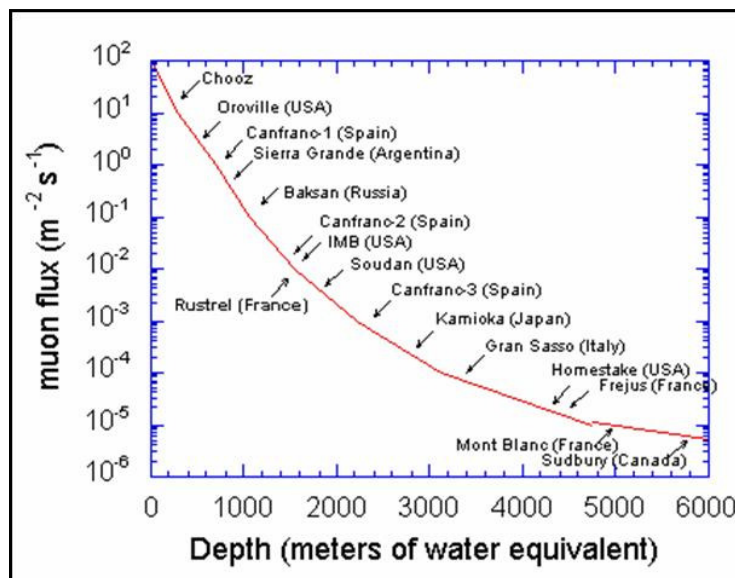
Figure 7.2: muon flux reduction with depth [91].

Nevertheless, this depth (1500 mwe) is more than enough to ensure vetoing of secondary cosmic neutrons and (μ,n) reactions in the surrounding rock (Figure 7.3).
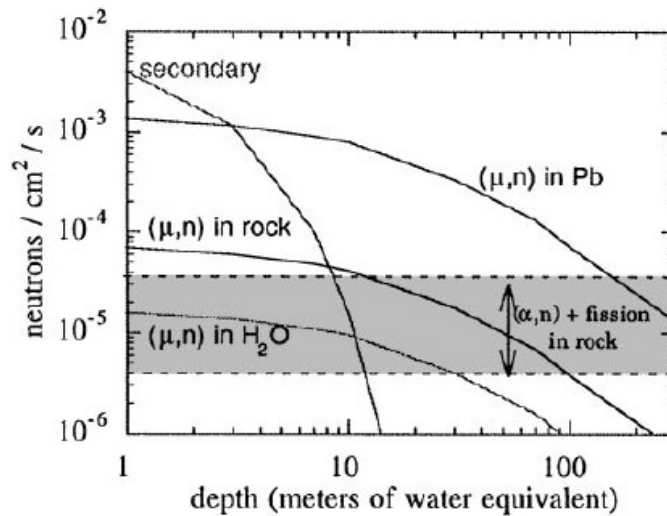
Figure 7.3: components of neutron flux as a function of underground depth [91].

The grayed band covers the typical contribution from natural radioactivity in rock, based on large-depth measurements and the average U and Th concentration in the Earth's crust. The contribution to the flux from muon interactions is derived from the systematics and measurements in Ref. [92].

Neutrons produced by natural radioactivity in the surrounding rocks are dominant below a few hundreds of m.w.e., independent of the nature of the shielding materials used in the experiments. An increased depth brings no further reduction in neutron flux [93]. The ambient neutron flux is primarily due to the surrounding calcite rock, estimated at well below 4×10^{-5} n/cm^{2}s [94]. The cavern is shielded from the rock environment by a 30–100 cm thickness of concrete, internally sheathed by a 1 cm thickness of iron. Radioassays of the concrete yielded 1.90 ± 0.05 ppm ^{232}Th and 0.850 ± 0.081 ppm ^{238}U, of the steel, 3.20 ± 0.25 ppb ^{232}Th and 2.9 ± 0.2 ppb ^{238}U [103,29]. The results are at the same level as those recorded in other near underground locations such as Canfranc, Modane, and Gran Sasso [95–97].

7.2.2 Muons

As seen in Figure 7.2 one can see that GESA has ~10^{-2} m^{-2}s^{-1} muon flux. At 1500 m.w.e. the muon flux becomes a secondary concern for the activities at GESA, and can be further suppressed with an active veto.

7.2.3 Airborne Radon

The circulation of air is obtained by the opening of the vertical escape chimney of the site, allowing for natural ventilation, and by having the ventilation system turned on.

The radon concentration in the atmosphere of the tunnel is measured during the entire year. The values oscillate between 60 Bq/m^3 in the Winter and 1000 Bq/m^3 in the Summer, as a result of the seasonal increase in water circulation within the mountain. Ventilation of the cavern air reduces this to ~ 100 Bq/m^3.

Radon measurements are continuously performed: the sensor and monitor of two Ramon 2.2 radon detectors are separated by 8 m and installed (one inside the inner shield the other in the outer shield described in section 7.4.2) for remote monitoring (Figure 7.4). The sufficient purging of the GESA atmosphere ~10 times per day, with a reduction in the radon level to ~100 Bq/m^3 was confirmed.
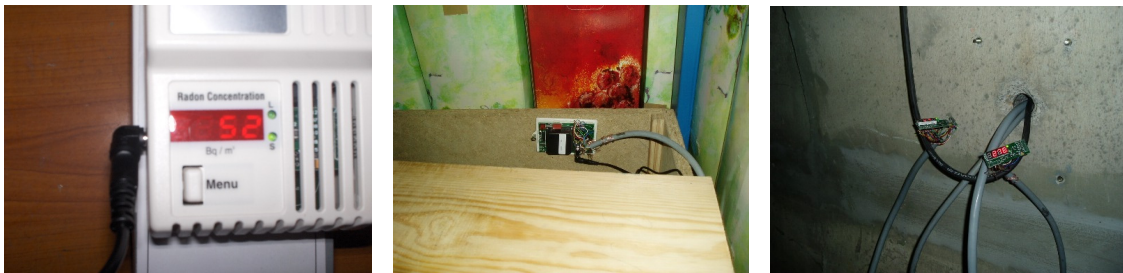
Figure 7.4: radon monitoring (L > R) monitor, sensor installation near the water pool, monitors outside GESA.

7.3 Experiment Execution

7.3.1 DAQ Installation

For the Phase II experiments 16 electronics channels were needed: 15 for the detectors and 1 for noise monitoring (via a freon-less device). Assembly of the 16 hand made channels of instrumentation amplification boards involved 16 PGA's (448 connections), 176 resistors (352 connections), 208 capacitors (416 connections), 80 LED's (160 connections), 16 Ferrites (32 connections), 16 female series (144 connections), 16 male series (288 connections), 16 caps, all with O'rings, swaglok fittings, microphone and microphone connectors (96 connections), 16 microphone cables, 32 sockets (96 connections), 48 female sockets for boards (144 connections), 16 sockets + cables for power supply + junction box (96 connections), 16 cables (15 m), sockets for I/O boards (96 connections) and pressure system (135 connections). Figure 7.5 shows the preamplifier core of the acoustic system and the caps with the associated pressure transducers.

Figure 7.5: DAQ system (L > R) preamplifier "core", SDD capping & pressure transducers.

Installation of the instrumentation cabling through the GESA walls, microphone connections and completion/testing of the inside 16 channels of signal and pressure DAQ, is shown in Figure 7.6.
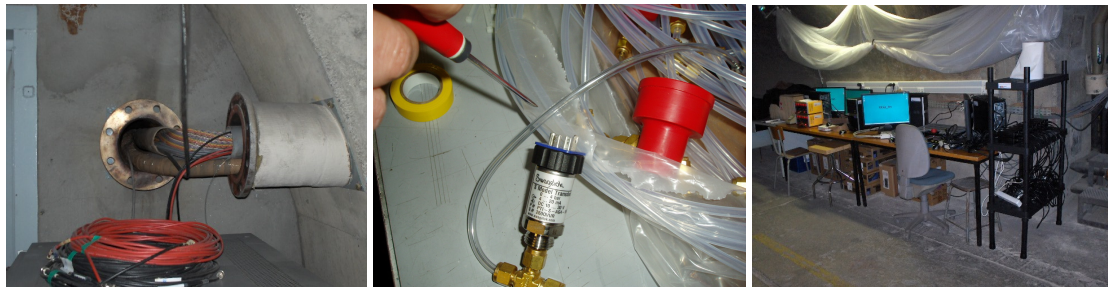
Figure 7.6: (L>R) cable insertion into GESA, testing of connections, completed DAQ station (outside GESA).

7.3.2 SDD Fabrication & Installation

The C_2ClF_5 SDDs were fabricated according to the standard protocol described in Chapter 3 at the underground 210 mwe clean room. The SIMPLE gel ingredients, all biologically-clean food products, were purified using actinide-specific ion-exchanging resins. The refrigerant was single distilled and the water double distilled.

The detectors were capped using a new mechanical construction which practically eliminates pressure microleaks. Each cap contains feedthroughs for pressure monitoring and the electret microphone encased in a latex sheath, which is immersed in a ~4 cm thick glycerin layer that covers the gel at the top of the detectors.

As a result of the fabrication protocol, the detectors were installed at the rate of one per day. In addition to the detectors, a freon-less but otherwise identical SDD was similarly installed: this unit served as an acoustic veto. The SDDs were immersed to a depth of 20 cm in a 700 liter water pool maintained by a water circulation cooler (Huber) at a bath temperature of 9.00 ± 0.10ºC and were pressurized to 2.00 ± 0.05 bar to reduce background sensitivity. Figure 7.7 shows the freon injection while the SDD is in fabrication in the clean room, the installation of the detectors in the 700 liter pool at GESA and the temperature control.

Figure 7.7: (L > R) SDD freon injection, SDDs being installed, and remote temperature monitoring.

The location of each detector in the water pool is shown in Figure 7.8. The exact location is important to the analysis of any anomaly or excessive nucleation rate registered by a SDD.
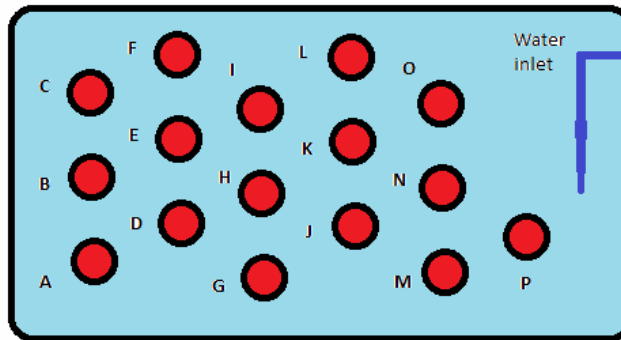
Figure 7.8: SDD disposition in the 700 liter water pool.

In Table 7.1 are presented the active masses for each individual detector for both stages of the Phase II SIMPLE Dark Matter Experiment.

Table 7.1: Installed detector and its active mass.

Channel	Board / Microphone	Active mass [g]	
		Stage 1	Stage 2
0	Charlie	11.3	15.9
1	Foxtrot	10.6	12.2
2	Bravo	12.0	18.6
3	Echo	21.2	13.7
4	Hotel	17.7	11.0
5	Alpha	13.2	12.8
6	Delta	12.0	14.1
7	Golf	18.8	12.9
8	Oscar	08.4	15.6
9	India	16.5	15.4
10	Lima	12.4	14.3
11	November	14.4	17.2
12	Kilo	12.3	11.5
13	Mike	10.1	15.2
14	Juliet	17.8	14.8
15	Papa	0.0	0.0

7.3.3 Signal Acquisition

The microphone outputs were processed (PGA-2500) with a unit gain, and recorded into two Terabyte computers. Each PC had a NI-PCI-6251 (16 An.In., 24 Dig.I/O, 2 An.Out.) I/O board, with a shielded cable (2m) SHC68-68-EPM linked to the connector block-screw terminal SCB-68 which

served to acquire the signals from the SDDs. The minimum voltage accuracy was 52 µV with a sensitivity of 6 µV. The acquisition rate (Fa) was set at 8 kSps in a differential mode.

Each microphone response was pre-amplified and recorded in a MATLAB platform in sequential files of 8 min duration and ~6 MB [99], with resolutions of 0.3 mV in amplitude, 1.6×10^{-2} ms in time and a frequency resolution of 0.01 Hz.

Each SDD had its own power supply (PCM5OUT03) with a noise stimulation of only 2% peak-peak.

The pressure readings were similarly recorded separately by the PTI-S-AG4-15-AQ transducer, and the time evolution of the device over-pressuring similarly recorded in a third 1 TB PC and NI-DAQ system.

7.3.4 Noise Channel Evaluation

The comprehensive noise channel evaluation consisted of measuring the noise level of each channel and pre-Amp board individually, and then repeating the measurements with the entire system functioning, as seen in Table 7.2.

Table 7.2: Comparison of noise level from each channel employed at the LSBB.

Channel	Board / Microphone	Noise of each chan. separately (mV)	Noise of all chan. running (mV)
0	Charlie	0.24	0.30
1	Foxtrot	0.26	0.28
2	Bravo	0.16	0.21
3	Echo	0.22	0.34
4	Hotel	0.26	0.30
5	Alpha	0.20	0.25
6	Delta	0.26	0.28
7	Golf	0.26	0.28
8	Oscar	0.23	0.25
9	India	0.26	0.27
10	Lima	0.26	0.26
11	November	0.20	0.26
12	Kilo	0.24	0.26
13	Mike	0.22	0.23
14	Juliet	0.22	0.23
15	Papa	0.30	0.34

The first item that is clearly noticed is that the same acoustic channels, when turned-on at the GESA, have around 1/3 of their noise value at the R&D laboratory (ITN), due to the reduction/elimination of all spurious electromagnetic noise. Obviously, when all channels are operational, they pick-up noise from each other. As seen from Table 7.2, the overall increase is ~15%. PC, monitor and power supply electromagnetic influences are all included in these measurements.

The electronics yielded a noise level of 0.28 ± 0.04 mV per device, in contrast to the ~ 1 mV in the R&D surface laboratory and a factor ~ 50-100 of the previous Phase I SIMPLE instrumentation.

7.4 Acoustic Backgrounds

Several studies were performed at GESA in order to evaluate the possible acoustic backgrounds. These included: a comprehensive noise channel evaluation on the 16 channels utilized, a first SDD implementation with this new instrumentation at the LSBB for an absolute commissioning, and a thorough noise environment evaluation to map all possible external noise that could obstruct a clear assessment of the science data.

7.4.1 Test SDD Implementation

The intent of these studies was to examine the performance of the new instrumentation in the underground environment, and to commission the equipment and experimental procedures. It also served to verify and compare the low noise rates, as well as the nucleation and SDD underground behaviour, with those at ITN.

A purified standard ~1 liter SDD, a uniform dispersion of ~ 10 g of C_2ClF_5, was made in the 70 m (210 mwe) deep clean room of the underground LSBB facility. It was then transported to the environmental low noise experimental area (GESA) at a depth of 500 m (1500 mwe), over-pressured to 2 bar, and installed in the 700 liter neutron moderating water pool at the normal operating temperature of 9ºC.

The detector named "Quebec" was installed on channel 2 ("Bravo") - since this channel had the lowest noise level. The temperature was established over a one hour period, and 8 min data files were acquired with a Fa = 8 kSps (the same acquisition rate for the science experiments). The noise level of the instrumentation with the SDD coupled in GESA site remains low (~0.17 mV).

The noise level was constant throughout the acquisition. In comparison with the results at sea level (ITN), the noise level was reduced by ~1/3.

The frequency response and respective time constants of the detector are shown in Figure 7.9. As before, the principal frequency and time constants observed are in the region of acceptance (box). No major variations are observed, since the temperature and pressure were maintained constant.
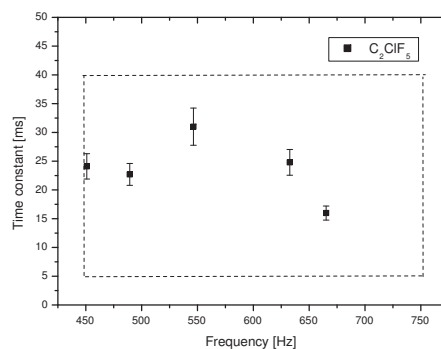
Figure 7.9: signal frequency and time constant variations throughout the preliminary measurements.

7.4.2 Noise Environment Evaluation

Numerous acoustic measurements were performed for identification and discrimination of any spurious acoustic background, and considered all possible environmental noise that might occur in or near GESA. The acoustic tests conducted with "Quebec" (~10 g) at 8 kSps on channel 2 were:

a) Normal tunnel noise (with the GESA door opened and closed).
b) Opening of the GESA door.
c) Fenwick (electric car) manoeuvring near GESA (with the door opened and closed).
d) Knocking on GESA's door.
e) Detector cable movements.
f) Detector cap tapping.
g) Human noise inside GESA.
h) Water cooler (HUBER) on - (with the GESA door opened and closed).
i) Circulation of water bubbles in the SDD bath.
j) Ventilation

a) Normal tunnel noise – with the GESA door closed and opened

With GESA's door closed, the noise is the same as before at 0.16 mV; opened, the noise rises to 0.22 mV, primarily due to the fact that nearby is LASA - the major power supply for the deepest part of the tunnel. There are no signals when all is maintained quiet, as shown in Figure 7.10. The 37% increase in noise simply indicates that the optimal condition for data acquisition is with the GESA door closed (Faraday Cage enabled).
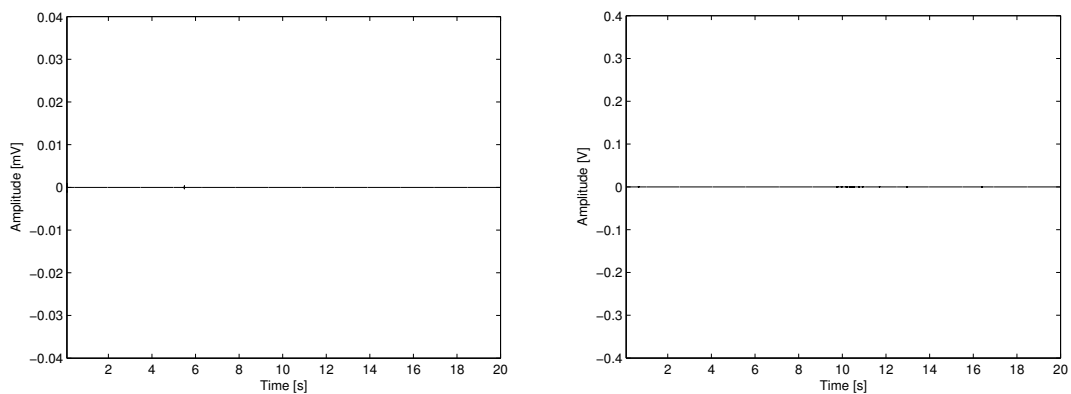
Figure 7.10: left, signal output with the Faraday cage closed and right, opened.

b) Opening of the GESA door

Emergency interventions in GESA require knowledge of the acoustic noise additions, in this case beginning with the opening of the door. The door opening takes roughly 10 s, as seen in Figure 7.11 (a) where a registered spike appears in coincidence. This process provokes an increase in the noise level to 0.18 mV. The FFT of the door opening, with signal slightly above the 450-750 Hz range of bubble nucleations, is shown in Figure 7.11 (b), showing no resemblance from a true bubble nucleation.

(a)   (b)
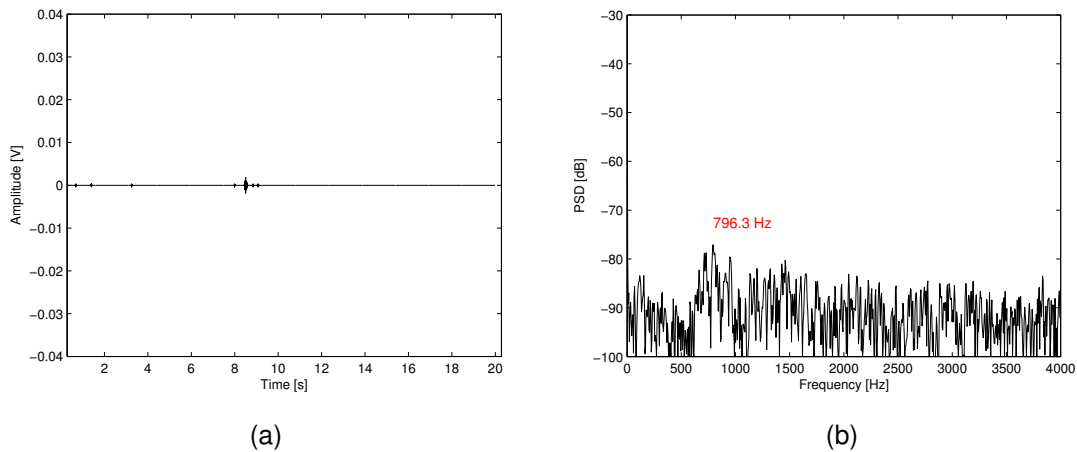
Figure 7.11: (a) signal output of the Faraday cage opening and (b) its FFT.

c) Fenwick (electric car) manoeuvring at GESA (door opened and closed)

Local Fenwick movement near GESA, due to tunnel maintenance and laboratory tours, is common in the LSBB. With the door opened and a Fenwick in motion nearby, the noise level increases to 0.43 mV, as shown in Figure 7.12 (a). The sound produced by these electric cars is registered at 2.35 kHz, well above the frequency window of a bubble nucleation, Figure 7.12 (b).

(a)   (b)
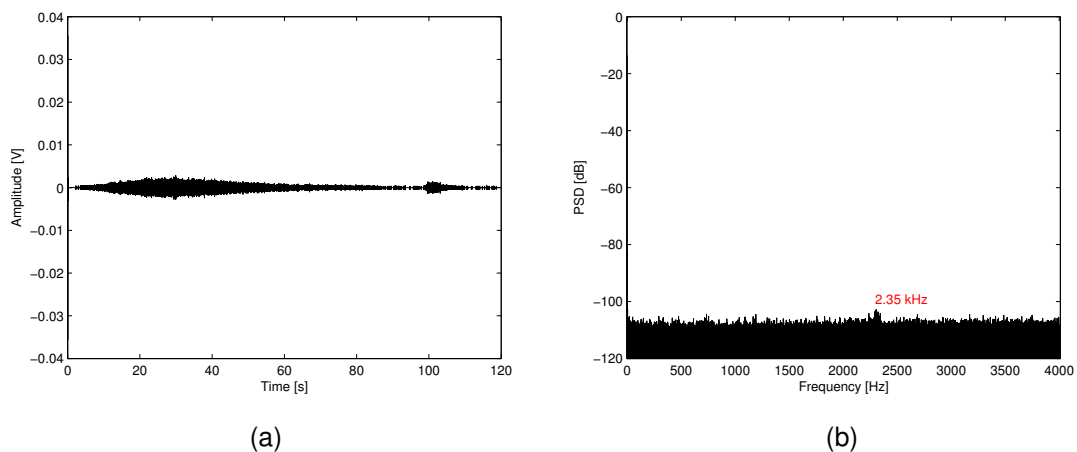
Figure 7.12: (a) signal output car manoeuvring with door opened and (b) its FFT.

If the door is however closed, the effect practically vanishes despite an increase in noise level. In this case the noise level was 0.29 mV and continues negligible in the frequency domain (Figure 7.13).

(a)   (b)
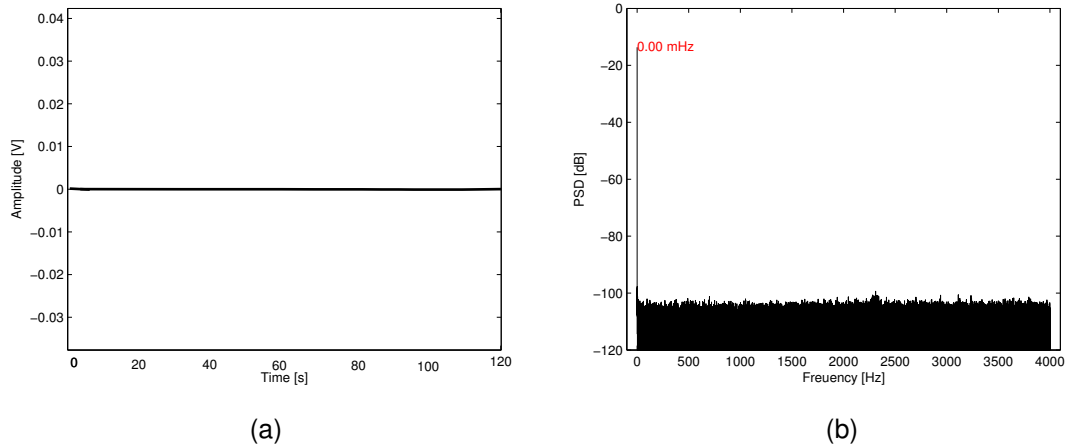
Figure 7.13: (a) signal output car manoeuvring with door closed and (b) its FFT.

d) Knocking on GESA's door

Accidental Fenwick or people contacts with the GESA door might not be uncommon, with a potential impact on the signal acquisitions. Door contacts were stimulated by knocking on it. With the door closed, the noise level was 0.16 mV. As seen from Figure 7.14, there is no signal registration of any kind, independently of the nature of the contact.
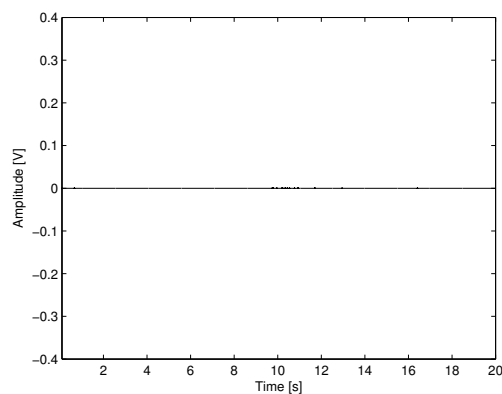
Figure 7.14: signal output on knocking at the door.

e) Detector cable movements

The detector cabling is prone to mechanical displacements resulting from interventions and intrinsic laboratory vibrations. Similar to the previous case, the intent was simply to see if any effect was captured in the recorded signal. As before, the GESA door was closed and a 0.16 mV noise level was recorded. Mechanical displacements were induced by moving and stepping on the cables. As seen in Figure 7.15, again no registration of any signal is noticed.
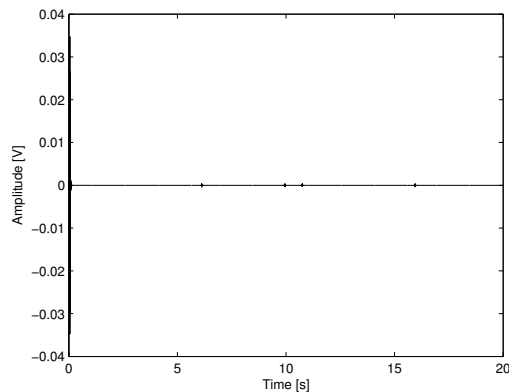
Figure 7.15: signal output on knocking on the cable.

f) Detector cap tapping

If not well secured, a signal cable or pressure line may move and impact with the SDD caps, producing an acoustic signal. This was reproduced by tapping on the caps. The noise level here was 0.20 mV. As seen from Figure 7.16 (a), there are many signals: after isolating them and performing the same analysis as for a true bubble nucleation, their principal frequencies are at the border line of the highest frequencies allowed for SDD nucleations, as seen in Figure 7.16 (b), with time constants of 13.67 ± 3.78 ms. This suggests that all SDDs, cables and pressure lines in the science runs should be in fastened positions to avoid this signal.

(a)   (b)
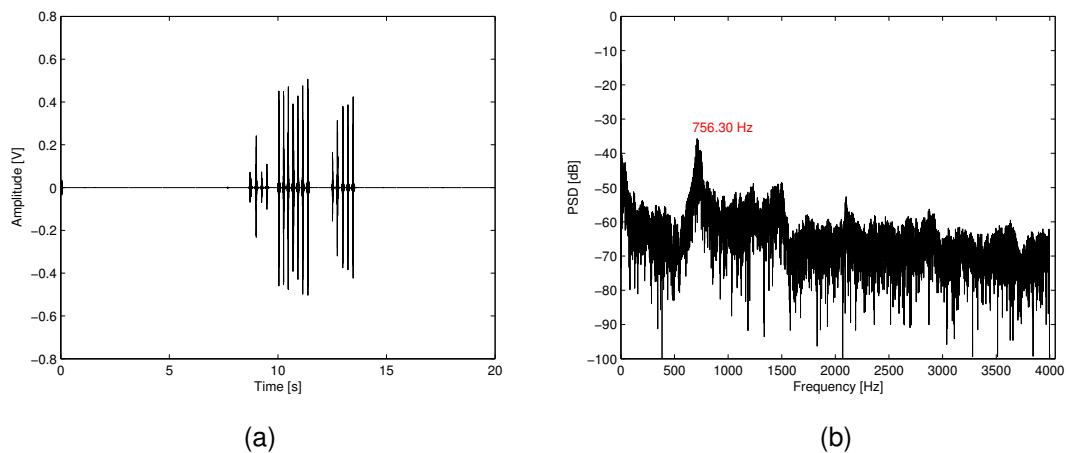
Figure 7.16: (a) signal output when knocking on detector caps and (b) its FFT.

g) Human noise inside GESA

Acoustic noise produced by human interventions inside GESA may be recorded by the detector electronics.

Such noise was generated by reading normal work activity in GESA, the door closed with one person inside with a flashlight, given that there is no electricity inside GESA. The electronic noise level remained at 0.17 mV.

As seen from Figure 7.17, the movement of boxes and tools in GESA is easily registered by the acoustic system. The time constants are 28.50 ± 4.12 ms. which is also in the same range of true bubble nucleations. Although the FFT is different, when SIMPLE is acquiring, all interventions inside the room should be avoided, data acquisition paused, or the precise time of interventions recorded.

(a)   (b)
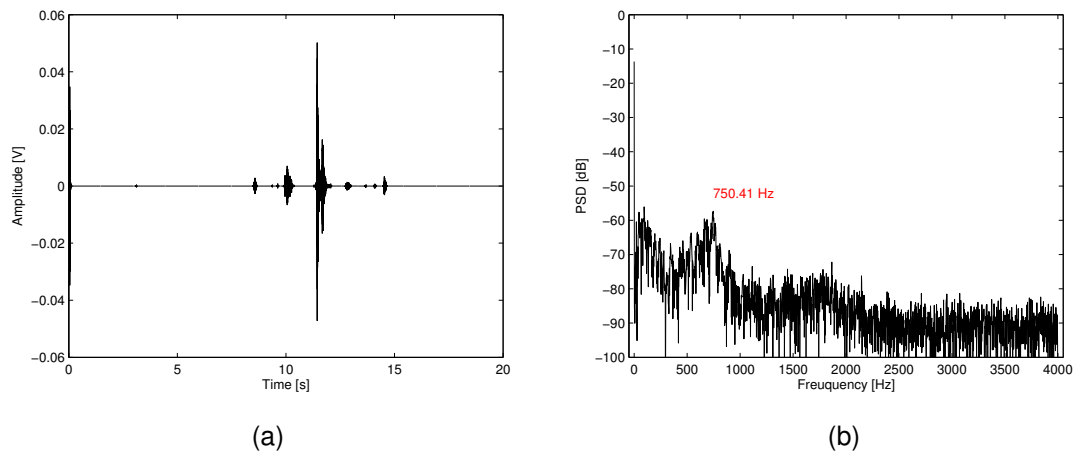
Figure 7.17: (a) signal output with human noise inside GESA and (b) its FFT.

h) Water cooler (HUBER) on – with the GESA door opened and closed

The operation of the HUBER cryothermostat, located outside GESA and used to control the 700 liter water tank temperature, generates the largest power consumption of the SIMPLE measurements and requires examination.

Two situations were investigated: the GESA door closed, and opened, Figure 7.18 shows both cases, neither of which have events, but with increased noise levels in both cases. With the door closed the noise level is 0.19 mV; opened, with the HUBER running, it rises to 0.23 mV.
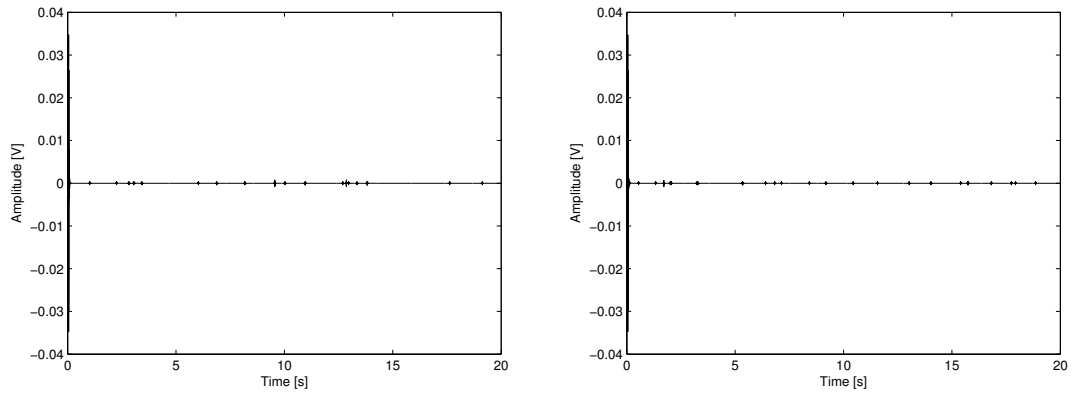
Figure 7.18: left, signal output with the GESA closed and right, opened.

i) Water bubbles in the SDD bath

The SDDs are immersed in a 700 liter water tank: the circulation of water to and from the HUBER can create water bubbles that are registered acoustically. While this is reduced by reducing the water flow and using a water inlet filter, here the water bubble creation was exaggerated.

The noise level measured was 0.17 mV. The events seen in Figure 7.19, have a time constant of 8.4 ± 1.19 ms, but possesses a FFT with a peak maximum at ~1.5 kHz, twice as large as a bubble nucleation and clearly discriminated.

(a)   (b)
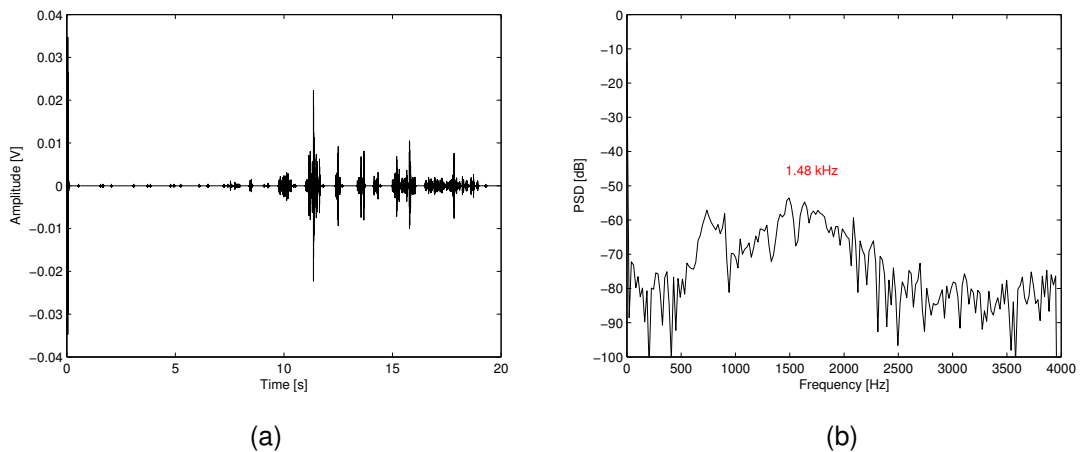
Figure 7.19: (a) signal output from water bubbles in the water tank and (b) its FFT.

j) Ventilation

The air flow passes through GESA at a rate of 0.2 ms^{-1} and requires evaluation. A photo of the ventilation duct system is shown in Figure 7.20 (a). The frequency spectrum with the ventilation on is shown in Figure 7.20 (b): the frequency of the acoustic signal lies far above the region of true bubble nucleations. The signal is highly attenuated with an acoustic protective foam inserted and water shielding.

<div style="text-align:center">(a)   (b)</div>
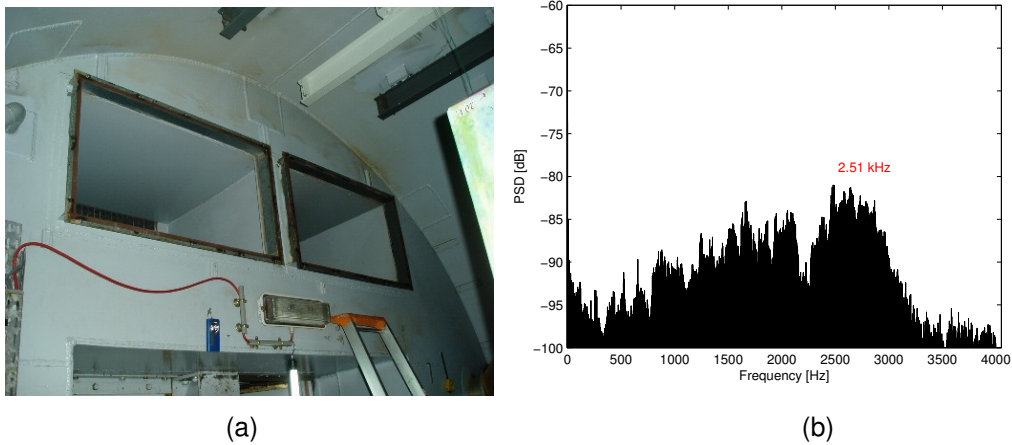
Figure 7.20: (a) photo of the ventilation shafts and (b) a FFT of the system.

The majority of the acoustic backgrounds are perfectly discriminated from true nucleation events by the analysing parameters, although it is of importance that entry into GESA is to be avoided during science runs, unless the data acquisition is stopped for short periods of time, or is time registered for a more rigorous cross-correlation.

7.5 Shielding Disposition and Estimates

7.5.1 Outer Shielding

The unique shielding of the main experimental halls was designed with the intention of protecting electronic equipment from the huge electromagnetic pulse created by nuclear explosion: instead of a conventional Faraday cage made of thin copper, a 1 cm thick iron shielding was employed. These large cages attenuate not only high-frequency electromagnetic waves but also low-frequency and even DC (e.g., the magnetic field of the Earth).

7.5.2 Inner Shielding - Stage 1

The construction of a 50-75cm thick water shield surrounding the detector water bath (comprising 8 ton in total), is shown in Figure 7.21 below.

Figure 7.21: water shield (L > R) before, during, and after construction.

The presence of U/Th contaminations in the gel, measured at ~0.1 ppb by low-level α and γ spectroscopy of the production gel by the PNNL (Pacific Northwest National Laboratory - USA) collaborators, yields an overall alpha background level of <0.5 evt/kg freon/d. A similar level is measured for the detector containment materials.

The water pool rests on a dual vibration absorber placed atop a 20 cm thick wood platform resting on a 50 cm thick concrete floor. The pool is surrounded by three layers of sound and thermal insulation. An additional 50–75 cm thick water shielding surrounds the insulated pool and pedestal, with a 75 cm water thickness overhead; 50 cm of water separates the pool bottom from the SDD bases. Figure 7.22 presents a schematic view of the room, with a concrete thickness varying between 30-100 cm. Some structures are removed from the figure for clarity (rock, left concrete wall, front water shield and tank water above and around the detectors).
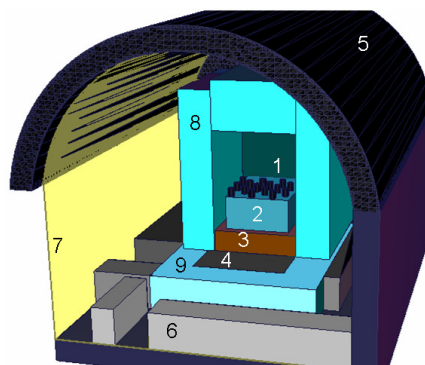
Figure 7.22: schematic view of the room and experimental set-up. 1: Detectors; 2: Tank (water below the detectors); 3: Wood support; 4: Tank pedestal; 5: Room ceiling, walls and floor; 6: Concrete floor structures defining the cable conduits; 7: Steel lining; 8: Water shield around and above the detectors; 9: Water shield around the tank pedestal.

Monte Carlo simulations of the on-detector neutron field, which include all shielding materials and account for spontaneous fission plus decay-induced (α, n) reactions, show negligible variations for concrete thicknesses $\geq$ 20 cm, and yield an expected neutron background of 1.09 $\pm$ 0.02 (stat) $\pm$

0.07(syst) evt/kgd. Figure 7.23 represents the majority of interactions from the simulations, where the most stronger contribution came from the concrete floor.
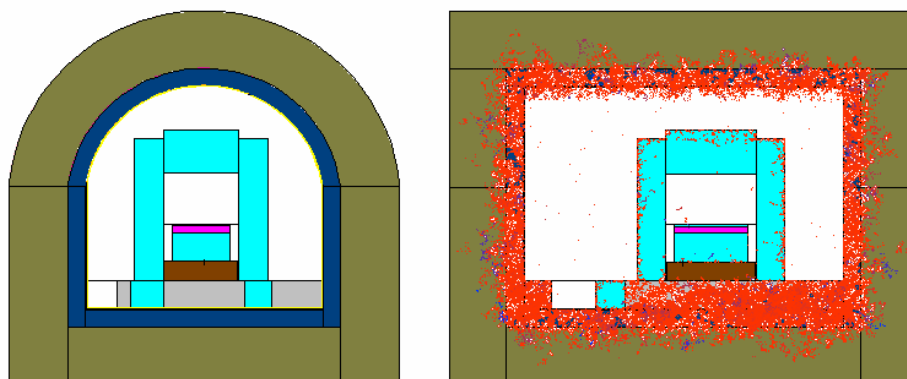
Figure 7.23: model used in the MCNP simulations. (L>R) vertical front view; vertical side view, with the representation of interactions of neutrons emitted from concrete.

As said before, the ambient radon level varies seasonally between 28–1000 Bq/m^3 as a result of water circulation in the mountain. Diffusion of the environmental radon into a detector is further limited by the surrounding water, which covered the detectors to just above their glycerin levels, and is circulated at 25 liter/min (equivalent to replacing the top 1 cm water layer each minute). The radon contribution is also low because of the short radon diffusion lengths of the SDD construction materials (glass, plastic, metal), the N_2 over-pressuring which inhibits the advective influx of Rn (via stiffening of the gel), and the glycerin layer covering the gel. The reduction in the overall radon contribution to the measurement, including its progeny, is estimated at $\sim10^5$, with the overall α contribution to the measurement (including the detector contribution) estimated to be 3.26 $\pm$ 0.08(stat) $\pm$ 0.76(syst) evt/kgd.

7.5.3 Inner Shielding - Stage 2

Following Stage 1 and MCNP guidance, the shielding was modified to include an additional 10 cm of wood and paraffin, and 10 cm of polyethylene below the water pool, with the surrounding water shield (Figure 7.24) rebuilt to eliminate neutron path ways.

As a result of the seasonal increase in water circulation within the mountain, the ambient radon level increased to $\sim$ 1000 Bq/m^3; continued purging of the cavern air reduced this to $\sim$ 100 Bq/m^3, and circulation of the pool water in combination with radio-assays of the detector construction materials, yielded a Stage 2 α-background estimate, including both progenitor and daughter decays, of 5.72 $\pm$ 0.12 (stat) $\pm$ 0.29 (syst) evt/kgd.
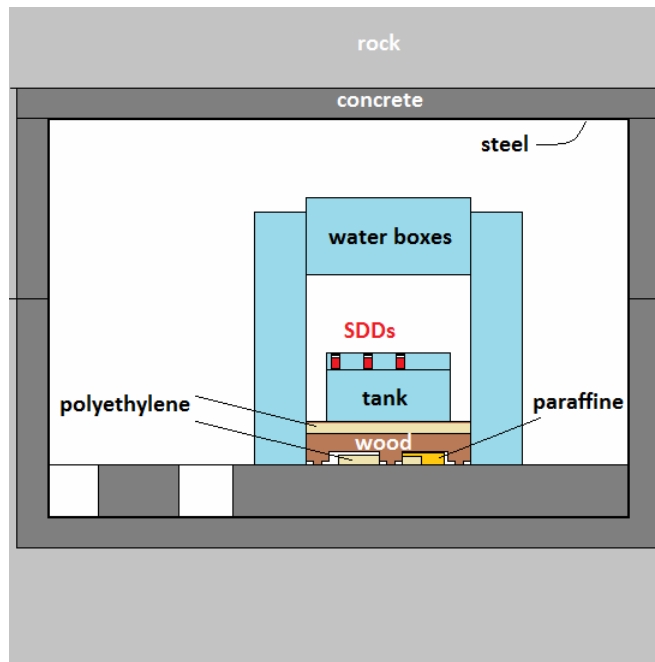
Figure 7.24: Stage 2 new set-up of the shielding after Stage 1 evaluation.

Extensive Monte-Carlo estimates of the expected neutron background, which accounted for spontaneous fission plus decay-induced (α,n) reactions, and included the increased below-pool shielding and new materials radioassays, yielded a reduced rate of 0.333 ± 0.001 (stat) ± 0.038 (syst) evt/kgd; recalculation of the Stage 1 disposition with new radio-assays yielded a revised background rate of 0.976 ± 0.004 (stat) ± 0.042 (syst) evt/kgd, with the primary contribution being the concrete. For the improved shielding of Stage 2, background neutrons originate mainly from the glass detector containment and shield water.

A full neutron characterization of the GESA measurement site was intended to be conducted, first by using 4 tubes 1m long by 3 cm of cross section filled with He+Ar to characterize the neutron flux in GESA, as shown in Figure 7.25. Only a short measurement was performed, owing to a power supply failure no major result was obtained.
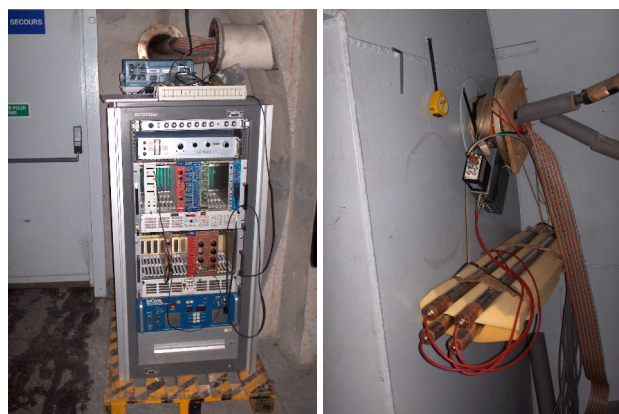
Figure 7.25: characterization of the GESA measurement site with He^3 tubes.

A complete Bonner sphere spectrometer system from the IRSN partner has been implemented in the entire LSBB, as shown in Figure 7.26. The measurements have been conducted with several locations and configurations throughout the tunnel. Preliminary projections (with and without shielding) appear to corroborate the estimates, but the measurements remain in progress.

Figure 7.26: characterization of the GESA measurement site with Bonner spheres.

Chapter 8   SIMPLE Dark Matter Analysis and Results

_____

8.1 Signal Analysis

All the previous analyses routines were developed and adjusted for each detector based on their noise levels and behaviour. The SDD identification, discrimination filter and validation analysis routine is presented on the design scheme in Figure 8.1.
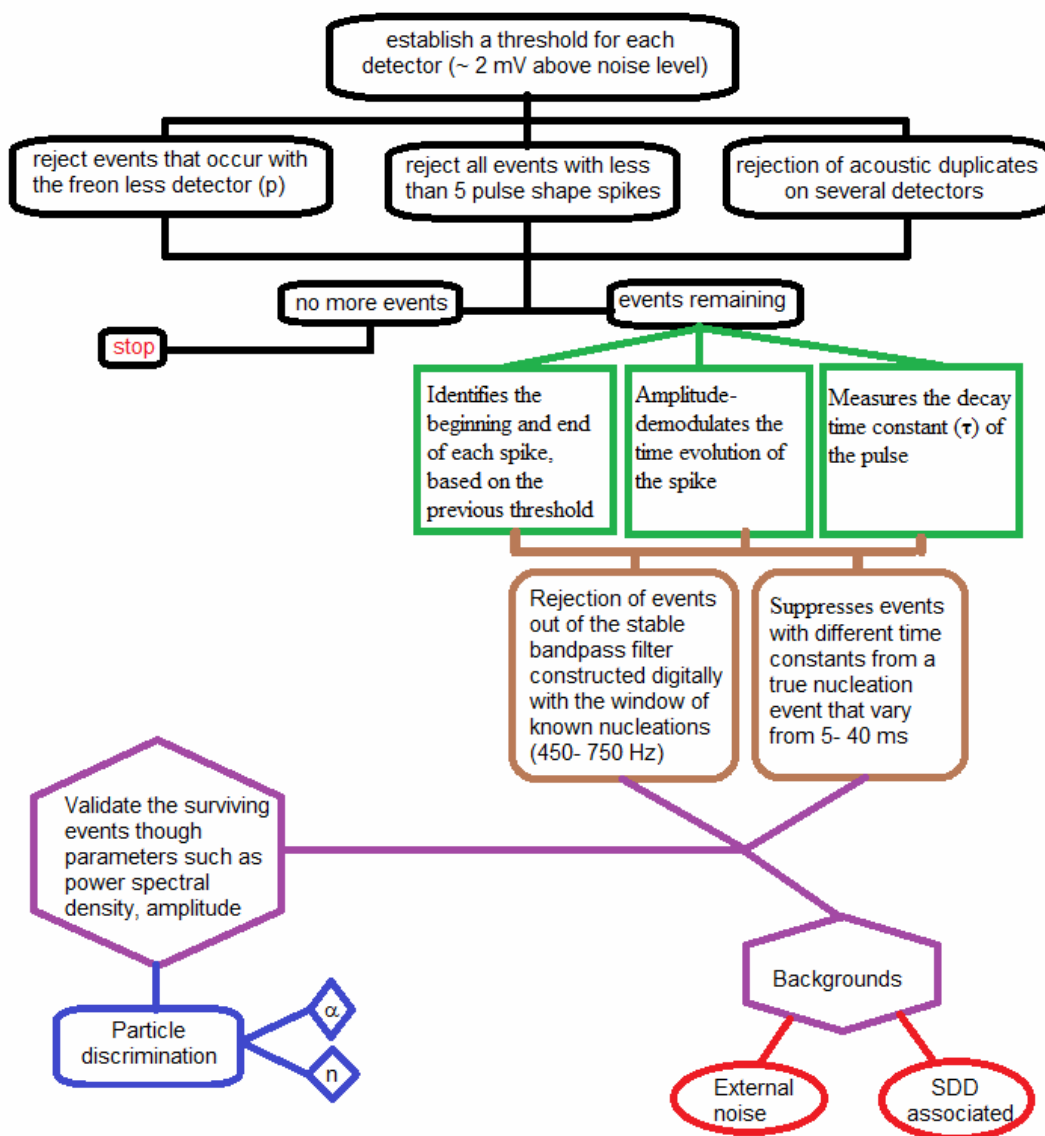
Figure 8.1: organogram of the SDD identification, discrimination filter and validation analysis routines.

The SDD signals, pressures, and temperature were monitored continuously during operation, as also the radon level.

Each detector was first inspected for raw signal rate and pressure evolution over the measurement period. An initial data set (4056 and 1997 events of Stage 1 and 2 respectively) was then formed by passing the data files through the pulse validation routine described in Chapter 4 [99] which tagged signal events if their amplitude exceeded the noise level of the detector by 2 mV. Tagged signals in coincidence with the freon-less device were next rejected, as also all candidate signals with less than five pulse spikes above threshold; the remaining set was then cross-correlated in time between all SDDs, and coincidences rejected as local noise events and that a WIMP interacts with no more than one of the in-bath detectors.

The signal waveform, decay time constant, and spectral density structure of the remaining [(1828-Stage 1) and (826-Stage 2)]) single events were next inspected individually. As earlier stated, a particle-induced nucleation event possesses a characteristic frequency response, with a time span of a few milliseconds, a decay constant of 5–40 ms, and a primary harmonic between 0.45–0.75 kHz [99]. This response differs significantly from those of gel associated acoustic backgrounds such as trapped N_2 gas (3.4-3.9% of the total), gas escape (0.008%), and gel fractures (4.4-8%) which appear at lower frequencies, as well as local acoustic backgrounds (81-88%) such as vibrational contact with their support or water bubbles which differ in power spectra. This event-by-event analysis permitted isolation of the true nucleation events with an efficiency (E_f=(1-CL)$^{1/N}$) of better than 97% at 95% C.L.

8.2 Stage 1

Data was obtained between 27 October 2009 and 08 February 2010, comprising an effective exposure of 13.47 $\pm$ 0.01 kgd, with a "loss" of 7.27 kgd from weather-induced power failures during the period and the fact that the detectors were introduced at one device per day over the period 27 October-14 November (once installed data acquisition was turned on).

8.2.1 Pressure Analysis

As seen in Figure 8.2, the pressure of all detectors remained below 2.2 bar, guarantying a threshold recoil energy of 8 keV as described in Chapter 6. The minor increase up to 2.2 bar during the 70 days is normal and due to all the SDD intrinsic behaviour (N2 gas release, fractures and nucleation events).
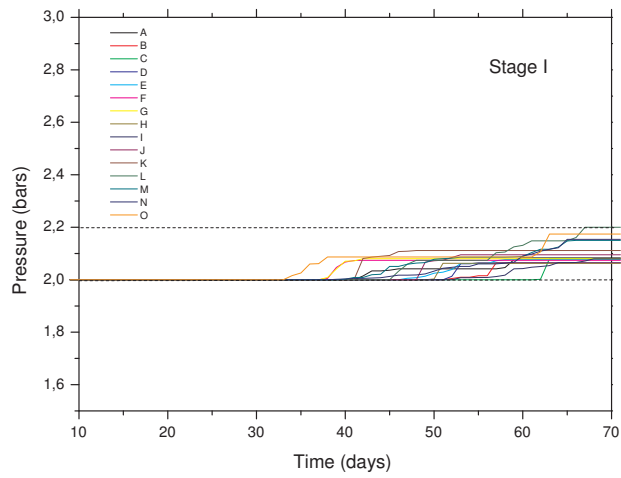
Figure 8.2: pressure evolution of the various SDDs on Stage 1.

8.2.2 Signal Analysis

Each signal was individually analyzed with respect to the organogram of Figure 8.1. Figure 8.3 displays the signal time constants with frequency for the uncorrelated signal events. The highlighted red box within the graph represents the particle window.
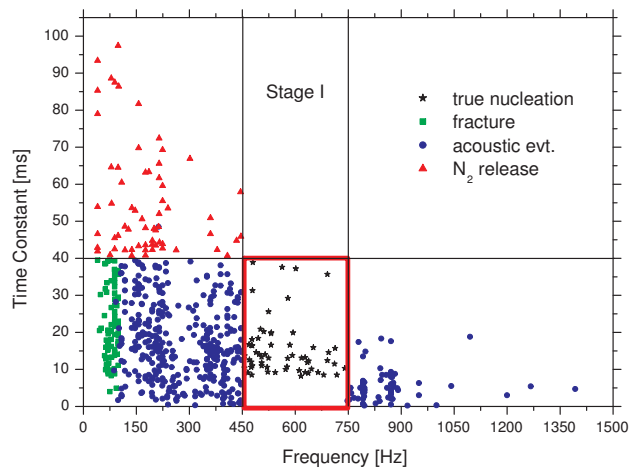
Figure 8.3: scatter plot of the time constant of Stage 1 single event signals with respect to their frequencies.

A total of 4056 signals were recorded, of which 1828 were uncorrelated single events (only these are shown in Figure 8.3). The signal waveform, decay time constant, and spectral density

structure of the 1828 single events were next inspected individually. Analysis of the signal parameters plus the FFT in each case identified 88% with various environmental acoustic noise events, 3.4% in trapped N_2 gas and 4.4% in fractures. Only 36 fracture events were recorded over the ~ 70 days of the 15 detector operation, or an average of 2.4 fractures per detector. More importantly perhaps, only 15 fractures were recorded by day 56 of the run, with only zero or one per SDD except in the case of two devices. This corroborates the longevity of the SDDs.

Figure 8.4 displays the signal amplitudes (A^2) with frequency for all events described before, with emphasis to each of the identified 56 particle-induced signal events, in which a gap corresponding to A = 100–130 mV is discernible.
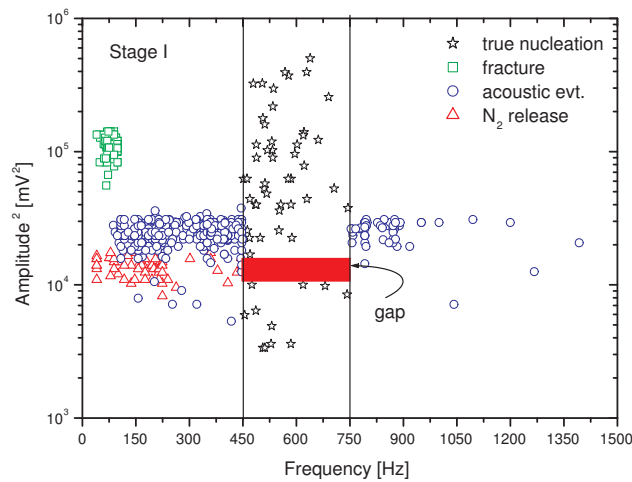
Figure 8.4: scatter plot of the amplitude of Stage 1 single event signals with respect to their frequencies.

8.2.3 Particle Event Result

The analysis of the recoil signals via the Hilbert transform-based demodulation identified 10 events, slightly below the estimated 13 ± 0.6 background neutrons. Figure 8.5 shows the logarithm of the squared signals amplitudes with respect to the calibrated separation between alpha and neutron recoils as seen in Figures 6.5 and 6.8 from the calibrations in Chapter 6.

Here one can clearly see that the separation is obvious and that 10 events are identified as nuclear recoils and the remaining as alpha induced. Only the former will be accounted for the interpretations, given that neutron recoils events are the ones that are mimicked by WIMPs.

Figure 8.5: scatter plot of the amplitude of Stage1 single recoil signals with respect to the calibrations.

8.3 Stage 2

Data was obtained between 12 April 2010 and 22 July 2010, comprising a total exposure of 13.67 ± 0.01 kgd, with a "loss" of 3.32 kgd from mechanical failure of 4 SDDs during the period run as a result of over-pressuring and that the DAQ was only enabled after the installation of half of the detector set.

The SDDs contained between 11 and 19 g of superheated liquid droplets for a total active mass of 0.215 kg; an additional, freon-less but otherwise identical, SDD again served as an acoustic veto.

The instrumentation was identical to that of Stage 1; in contrast to Stage 2 however, the SDD pressures were allowed to rise with time in order to obtain additional information and confirmation on the measurement sensitivity, seen in Chapter 6.

Again, each signal was individually analyzed with respect to the organogram of the SDD identification, discrimination and validation analysis routines presented in Figure 8.1.

8.3.1 Pressure Analysis

The pressure records (Figure 8.6) of all SDDs were inspected for evolution during the measurement, and correlated with the signal records. Data obtained at pressures greater than 2.20 bar were excluded (due to sensitivity and threshold recoil energy loss), reducing the Stage 2 exposure to 6.71 kgd.

Data at pressures ≥ 2.2 bar was used to confirm $\Lambda = 1.40 \pm 0.05$, yielding no α-sensitivity whatsoever above 2.30 bar as observed experimentally. For pressures ≤ 2.20 ± 0.05 bar, the threshold recoil energy at 9ºC remained below 8.0 ± 0.3 keV.
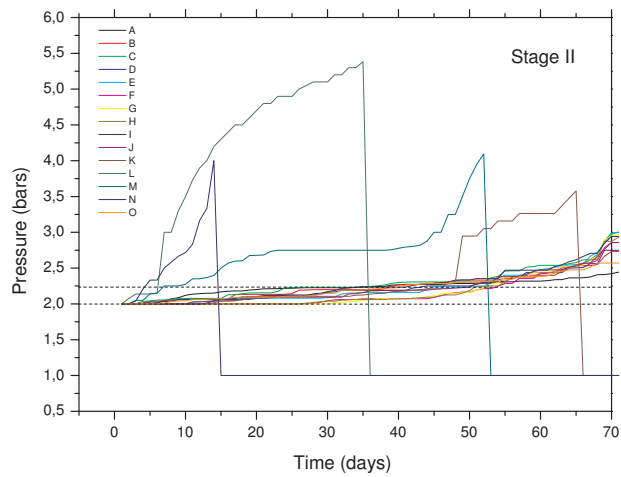
Figure 8.6: pressure evolution of the various SDDs on Stage 2.

8.3.2 Signal Analysis

Figure 8.7 shows the scatter plot of the event signals, where the total number of events is reduced to half, principally due to a half exposure and an increase shielding. In the figure the signal time constants with frequency for the uncorrelated signal events are displayed. Once more, the highlighted red box within the graph represents the particle window.
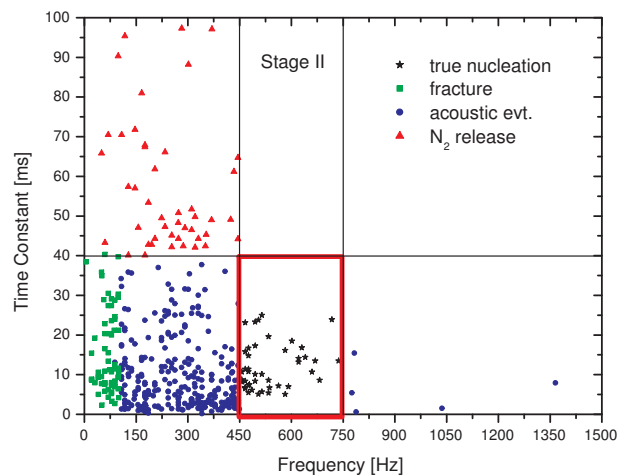
Figure 8.7: scatter plot of the time constant of Stage 2 single event signals with respect to their frequencies.

A total of 1997 signals were recorded, of which 826 (shown in Figure 8.7) were uncorrelated single events. Analysis of the signal parameters plus the power spectral density in each case identified 83%

with various environmental acoustic noise events, 3.9% in trapped N_2 gas and 8.0% in fractures. With the obtainable exposure, 67 fracture events were recorded over the ~45 days of the 15 detector operation, or an average of 4.4 fractures per detector. However ~50% of these fractures occurred in the 4 SDDs which failed: the event fracture rate is roughly consistent with Stage 1.

Figure 8.8 displays the signal amplitudes (A^2) with frequency for all events described before, with emphasis to each of the identified 41 particle-induced signal events, in which a gap corresponding to A = 100–130 mV is discernible. It is seen that the amplitude behaviour is essentially the same. For true bubble nucleation a clearer separation is enhanced between the lower 2 neutron recoil events from the α population.
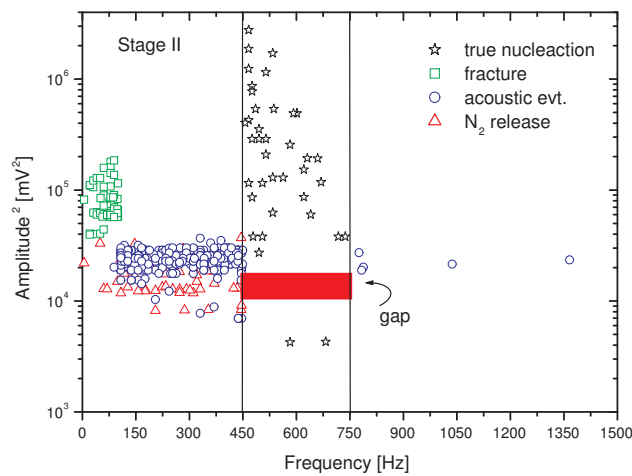
Figure 8.8: scatter plot of the amplitude of Stage 2 single event signals with respect to their frequencies.

8.3.3 Particle Event Result

As for Stage 1, Figure 8.9 shows the logarithm of the squared signals amplitudes for each of the identified 41 particle-induced signal events in Stage 2 with respect to the calibrated separation between alpha and neutron recoils as seen in Figures 6.5 and 6.8 from the calibration in Chapter 6.

As in Stage 1, the separation of the n,α events is once more obvious and consistent with the calibrations. A nuclear recoil discrimination cut at A ≤ 100 mV, a total of 2 events were recorded for the entire exposure. Correlation with the pressure records below 2.2 bar, yielded a signal record of only 1 recoil (the ~ 582 Hz in the previous figure or the lower event here) event consistent with the estimated 2.2 ± 0.3 background neutrons.
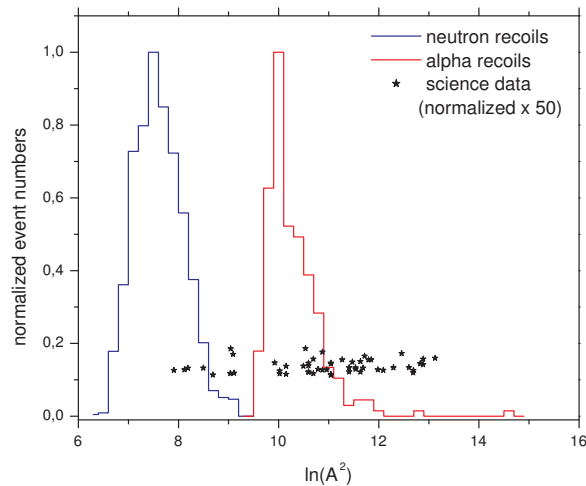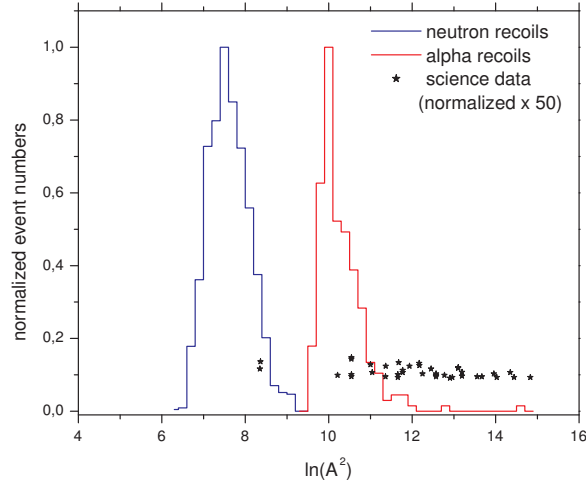
Figure 8.9: scatter plot of the amplitude of Stage 2 single recoil signals with respect to the calibrations.

8.4 Data Interpretations

8.4.1 WIMP Scattering Rates and Cross Sections

The differential energy spectrum of nuclear recoils is expressed in the form:

$$\frac{dR}{dE} = \frac{\rho}{2M_w}\frac{\sigma}{\mu^2}F(E)\varepsilon(E)\int_{v_{min}}^{v^{max}}\frac{f(v)}{v}dv\,,$$

(8.1)

where *dR/dE* is the rate per unit target mass and recoil energy, ρ is the local halo mass density, M_w the WIMP mass, σ the zero momentum transfer cross section, *u* the WIMP nucleus reduced mass, F(E) the nucleus Helm FF, ε(E) the detection efficiency, f(v) the halo velocity distribution relative to the detector, v_{min} the minimum velocity an incident WIMP needs to have in order to produce a recoil of energy E and v_{max} the local galactic escape velocity relative to the detector (maximum WIMP velocity in the halo). The total cross section is the sum of two components, spin-dependent (SD) and spin-independent (SI).

Spin-dependent scattering

The SD cross section is given by [113]:

$$\sigma_{SD} = \frac{32m_r^2G_F^2}{\pi}\frac{J+1}{J}\left[a_p<S_p>+a_n<S_n>\right]^2,$$

(8.2)

where G_F is the Fermi coupling constant and *J* is the total angular momentum of the nucleus, $a_{p,n}$ are the effective couplings of WIMP-proton and WIMP-neutron interaction and $<S_{p,n}>$ are the expectation values for the spin content for protons and neutrons in the nucleus.

110

The $S_{p,n}$ are obtained from nuclear structure calculations within a given model for individual targets.

The standard approach (the Odd Group Approximation) assumes that the spin is carried principally by the valence nucleons, either n or p, with the others only spectators. In the case of ^{19}F, the spin is mainly in the proton sector: setting $a_n = 0$, $a_p = 1$ then yields

$$\sigma_{SD} = \frac{32m_r^2 G_F^2}{\pi} \frac{J+1}{J} \left[<S_p> \right]^2,$$

(8.3)

with $<S_p^F>$ = 0.441 [112]; for $<S_p^{Cl}>$ = spin values are from [113], while for ^{13}C they were estimated using the odd group approximation.

Spin-independent scattering

A spin-independent WIMP-nucleon interaction corresponds to a coupling to the nucleon density operators, characterized by coupling constants f_p and f_n to protons and neutrons, respectively. The spin-independent WIMP-nucleus cross section is obtained by:

$$\sigma_{SI} = \frac{4m_r^2}{\pi} \left[Zf_p + (A-Z)f_n \right]^2,$$

(8.4)

where $f_{p,n}$ are the effective couplings to protons and neutrons, Z is the number of protons and (A – Z) is the number of neutrons. Most calculations assume that fp = fn, reducing the calculation to a single parameter; for this case there is an A^2 enhancement. From eq. 8.4, $[Z+(A-Z)]^2 = A^2$. This then yields

$$\sigma_{SI} = \frac{4m_r^2}{\pi} f^2 A^2.$$

(8.5)

8.4.2 Exclusion Limits

8.4.2.1 Spin-Dependent

The impact of the results from Stage 1 and 2 are shown in Figure 8.10 on SD WIMP- proton scattering, together with the competitive results of other direct (PICASSO, COUPP and KIMS) [104–106] and indirect (IceCube and SuperK) [107, 108] experiments. The contours are calculated using the Feldman-Cousins (since both rates were non-zero but consistent with the background estimates) approach [103, 109] based on observing n events against a background one systematic uncertainty below the estimated neutron-generated recoil background, η' with Γ=3.6, the standard isothermal halo of Lewin and Smith and a WIMP scattering rate [111] with zero momentum transfer, spin-dependent cross section σ_p^{SD} for elastic scattering. The form factors of J. D. Lewin and P. F. Smith [111] have been used for all odd-A nuclei, with the spin values of A. F. Pacheco and D. Strottman [112] used for ^{19}F; for ^{35}Cl and ^{37}Cl, the spin values are from F. Giuliani [113], while for ^{13}C they were estimated using the odd group approximation. The Stage 2 result is seen to nearly equal the Stage 1 result with its minimum of σ_p = 9.2 x 10^{-3} pb at 35 GeV/c^2, despite half the exposure.
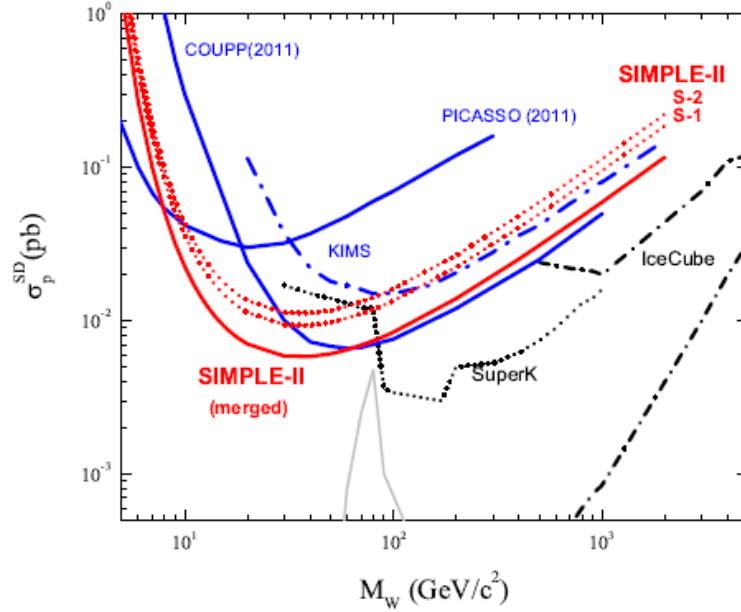
Figure 8.10: various spin-dependent WIMP-proton exclusion contours for Phase II, together with the leading direct [104–106] and indirect SuperK [107], IceCube [108] search results; shown are the Stage 1 and 2 results and a merging of the two. The region outlined in grey is preferred by cMSSM [110].

8.4.2.2 Spin-Independent

The impact of the results in the SI sector is shown in Figure 8.11 in comparison with results from other leading search efforts [105, 106, 114–124], again calculated with the standard isothermal halo and WIMP elastic scattering rate of Ref. [111] using Feldman-Cousins, a Helm nuclear form factor, and η'. Again, the Stage 2 contour is nearly equal to the revised Stage 1 contour with its contour minimum of 7.6 x 10^{-6} pb at 35 GeV/c^2. Owing to the low recoil energy threshold, both results enter the possible light mass WIMP region recently suggested by CoGeNT [124] and CRESST-II [122].

A straightforward combination of the two results using the Feldman-Cousins approach, based on the 11 candidates with an assumed background 1 σ (syst) below the expected total background, yields the "merged" contours indicated in each of Figures 8.10 and 8.11; in the SI case, the contour minimum is 4.7 x 10^{-6} pb and the result is in some tension with the recent reports of CoGeNT [124], DAMA/LIBRA [123] and CRESST [122] regarding light mass WIMPs, nevertheless the result is confirmed by the remaining leading SI search efforts (XENON, CDMS, EDELWEISS, ZEPLIN, COUPP and KIMS) [105, 106, 114–124]. For the case of SD interactions, the contour minimum is 5.7 x 10^{-3} pb, constituting the most restrictive direct search limit on SD WIMP-proton scattering for $M_W \leq 60$ GeV/c^2 to date, and beginning to complement the more sensitive results obtained by indirect detection measurements.
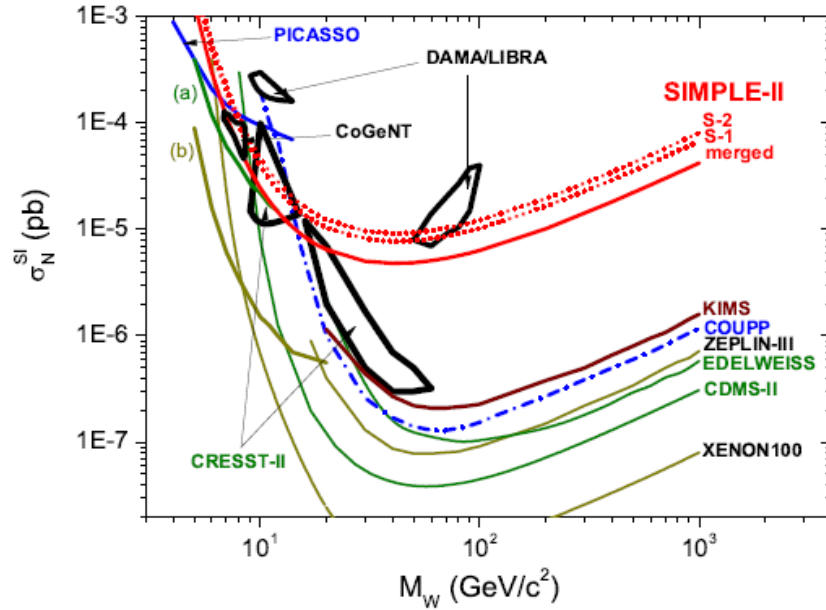
Figure 8.11: various spin-independent contours for Phase II, together with those of the leading [105, 106, 114–121] spin-independent search results; shown are the Stage 2 result, the reanalyzed Stage 1 result, and a merging of the two. The partial contours (a) and (b) are taken from [118] and [26], respectively. The closed areas identified as either CRESST-II [122], DAMA/LIBRA [123] or CoGeNT [124] represent the regions in which possible light mass WIMPS have been respectively reported.

The improved restrictions of both Stage 1 and 2 contours are a direct result of the new implemented instrumentation (with all its findings and indications), more detailed signal analysis, improved radio-assays of the shielding materials, and the revised nucleation efficiency in the analysis: Stage 2, with the additional benefit of its improved neutron shielding, provides an almost identical sensitivity with half the Stage 1 exposure. The results are sufficient motivation for a larger exposure measurement with further neutron background reduction, and variation of the SDD operating temperature/pressure to provide a lower recoil energy threshold, towards clarifying the DM situation.

Chapter 9 SIMPLE Phase III Big Droplet Chamber

_____

The results of Chapter 8, providing the most restrictive results in the spin-dependent sector, as well as motivating challenges in the spin-independent, demonstrate the competitively of the technique in dark matter searches. They however also clearly identify several drawbacks to the SDD approach; the most notable being the need for a significant increase in the experimental active mass. For 1 kg of active mass, ~75 SDDs would be needed. As each SDD is done and installed in a daily fashion, and more DAQ systems and space would be needed, this would mean a longer preparation time than the effective exposure time.

This suggests the use of a bubble chamber, which unlike a SDD involves no distribution of superheated liquid droplets in a gel matrix, so that the active mass ~ the device volume-fiducial volume. However, this raises two problems: following on the results of COUPP, the loss of the viscoelastic gel matrix as the response medium precludes the use of the previous low frequency instrumentation (the signal of which derives from the gel response to a bubble nucleation event). Second, the chamber requires recompression after each nucleation event.

In an attempt to circumvent the first, SIMPLE has embarked on the R&D of a bubble chamber variant. The so-called "big droplet chamber" (BDC) consists of a large volume superheated liquid droplet immersed in a glycerine bath sheathed by gel which coats the containment surface. A 300 g BDC was prototyped by SIMPLE in 2010, of approximately the same size as a single Phase II SDD. The use of a purified food-gel based-sheathing of the containment provides the same smooth gel-freon interface as with the SDDs (to reduce the probability of spontaneous nucleation: recompression times of up to ~ 12 h have been observed [79]) while maintaining the containment radio-purity (α-induced events < 0.5 evt/kgd), and preserving the reduced cost of detector fabrication.

9.1 BDC Prototype Construction

The prototype was constructed from a "home water filter" than can stand pressures up to 10 bar. The cap was simply coupled to the refrigerant injection and pressure control systems.

The containment vessel was sheathed with the purified food-based SDD gel. While the gel was still hot, a U-tube was introduced so that a hole was made for the injection of liquid Freon. After the gel solidified, the U-tube was removed without compromising the smoothness of the surface by inserting hot water in it and waiting ~10 min. Since the hole presented some imperfections that could trigger an event, hot glycerin was then inserted into the hole, smoothing all the imperfections.

Several CCD pictures (Figure 9.1) were taken throughout this process and the container permits distinguishing small bubbles, implying that an optical system could be implemented.

Figure 9.1: (L>R) evolution of gel introduction and construction of the BC prototype.

9.2 BDC Recompression Electronics

The assembled circuit was tested as well as the chamber in the clean room area at LSBB, France. The device is to be pressurized at a pressure P1 shown in Figure 9.2, slightly above the vapour pressure of the Freon to be used. When the Freon is injected all valves are closed. Once injected, then both valves are opened so that a pressure of P1+P2 is achieved.
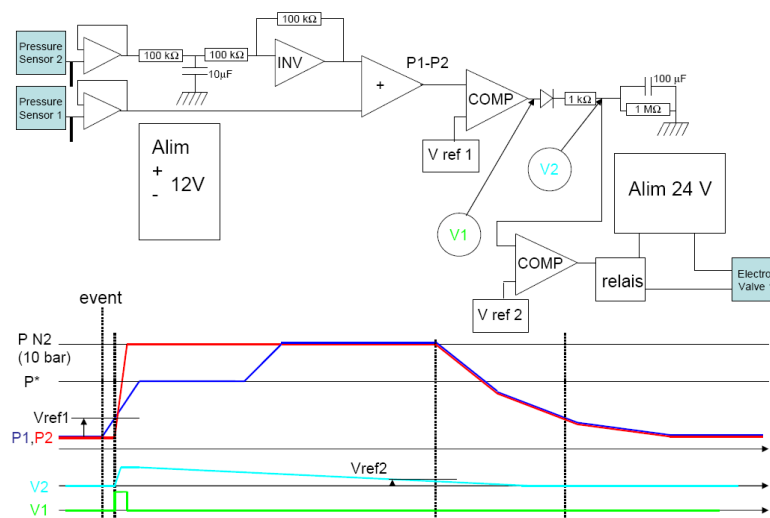
Figure 9.2: schematic of the acquisition, control and operating diagram circuit for the BDC.

To activate the detector, valve (V2) is opened, meaning that there is an increase of pressure, P* (~1 min), and one waits for an event to occur. Once an event is registered, the hydrostatic pressure of the glycerin is increased (~5 bar) in the big droplet chamber until the saturation of the Freon. The command pressure in the device is defined at 6 bar so that the bubble created can shrink immediately (roughly around 1 second), implying that this step has to be automatic.

The activation of the device happens by an interactive choice of the voltage references Vref1 and Vref2, so that comparator 1 triggers for a difference of pressure P1-P2 = 1bar, and comparator 2

triggers for a voltage V2 equal to ~1 volt for instance. Where P* is the saturating pressure, P1 and P2 are the pressures measured by sensors 1 and 2 (see electronic scheme).

At the Initial state the valve V2 is closed and valve V1 opened. The large droplet under pressure has roughly 10 bar > P*. Like this, the droplet is stable with P1 = P2 = 10 bar and V1 = V2 = 0.

When the device is activated, valve V2 is open as the controlled micro-leak occurs between pressure sensors 1 and 2. The pressure P2 slowly decreases and P1 "follows" P2 with a small delay (due to the micro-leak between pressure sensors 1 and 2). The pressure of P2 and P1 tend to 1 bar, but P1 at a much slower rate.

The new "superheated liquid chamber" (BDC) recompression electronics is shown in Figure 9.3.

Figure 9.3: (L>R) recompression electronics for the BDC; and the system in operation.

The initial "home water filter" prototype was recompressed using a pressure-activated system; a new piston-based recompression prototype (Figure 9.4) capable of providing the required long-term operational stability and to separate the recompression gas (N_2) from the gel and superheated liquid has been developed. The prototype scale-up to a larger liquid containment is still constrained by commercial plastics and their ability to sustain a 10 bar recompression. All of this apparatus of the recompression system as well as the acoustic instrumentation is mounted at opposing ends of the BDC.
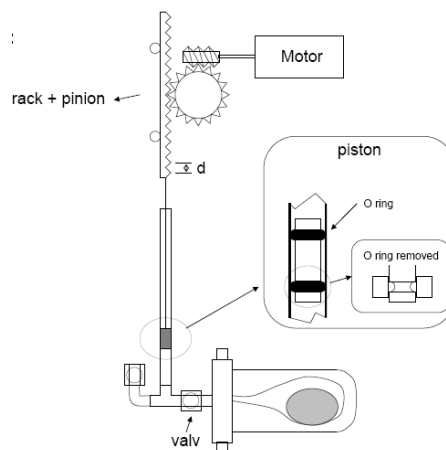

Figure 9.4: new piston-based recompression BDC prototype.

9.3 BDC Instrumentation

As recently demonstrated by COUPP [27], the primary particle-induced event signal emerges from the differing number of proto-bubbles formed in the superheated liquid. The proto-bubble signal however lies in the high frequency regime of ~130 kHz, requiring a replacement of the current sensors.

This was investigated with the prototype BDC using an externally-polarized condenser (CM16/CMPA40-5V from Avisoft-Bioacoustics) microphone with a flat response over 10 – 150 kHz. The digitizer NI-DAQ to meet the range of the microphone used was the NI PCI-6251 16-Bit, with at least 1.25 MSps for 1-Channel. The ultrasound microphone response over the 10 – 150 kHz range is shown in Figure 9.5.
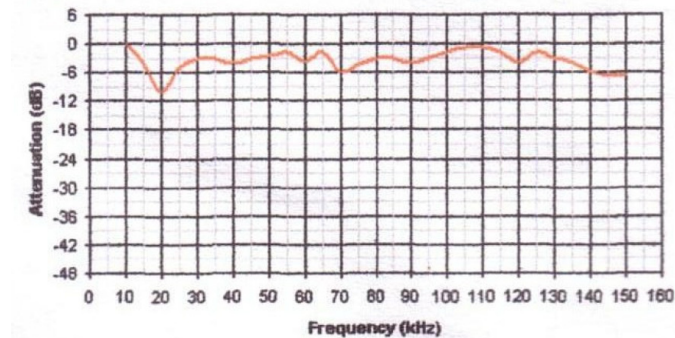
Figure 9.5: ultrasound microphone flat response over 10 – 150 kHz [130].

The condenser (CM16/CMPA40-5V) microphone, shown in Figure 9.6, consists of three components. The capsule (1) is connected to the cylindrical preamplifier module (2) by means of a 2.5 mm thread. This allows an easy replacement of the capsule. In favour of a proper operation, both this 2.5 mm thread and the 17 mm thread on the preamplifier module must be well fastened. Conversely, one should use only moderate forces when manoeuvring the microphone, in order to prevent mechanical damages. The polarization voltage supply and preamplifier unit (3) provides the polarization voltage for the microphone capsule and includes an adjustable 40 dB preamplifier with a balanced output. The CMPA module (2) can be attached either directly to the polarization module (3) or via a 5-pole XLR extension cable.

Figure 9.6: new condenser microphone.

The integrated preamplifier has an internal compensation circuit that slightly boosts frequencies above 50 kHz. The integrated polarization voltage generator will take up ~20 seconds after switched-on, until full voltage of 200 V and maximum sensitivity is reached.

One should be careful not to damage the protective grid, since the frequency response may be degraded. Another concern is the deterioration of the diaphragm, when used under heavy humid conditions.

9.3.1 Initial Test Trials

While the BDC construction and adjustments to the electronic procedure were being conducted an effortless test to confirm the practicality of the microphone was prepared, in which a dog whistle was blown. Figure 9.7 (a,b) shows the test results. As known, the response of the "unheard" sound had a frequency ~21.5 kHz.
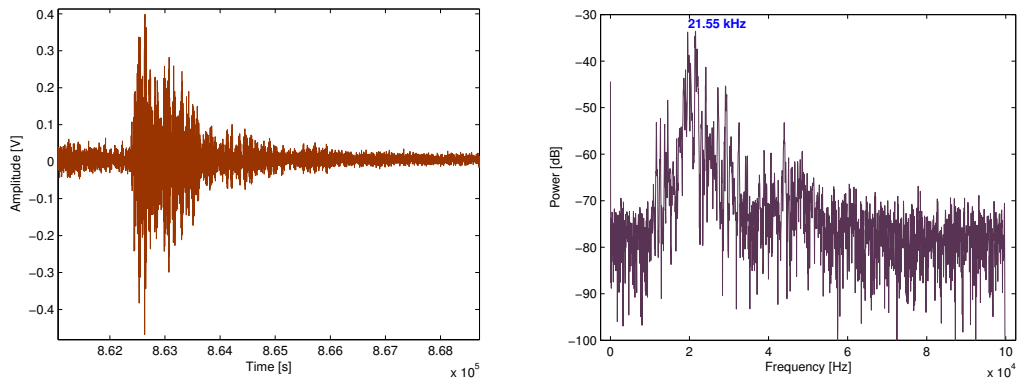
Figure 9.7: (L>R) first ultrasound recording and respective frequency spectrum.

9.3.2 BDC Nucleation Response

The set-up of the prototype constructed from a "home water filter" with the electronics, the instrumented microphone, the new piston based system and the C_2ClF_5 refrigerant was conducted at the LSBB in the vicinity of the clean room. In Figure 9.8, one can see the injection of the Freon into the BDC that has the SDD gel. The Freon (approximately 300 g) is introduced directly into the glycerin filling.

The new piston based system was coupled easily and the ultrasound microphone was set at one end of the bubble chamber. Here, one can see the big droplet resting at the lower part of the detector in a superheated state. The temperature of the entire process was also measured by means of a thermocouple type K - blue wire in the last photo of the figure.

Figure 9.8: (L>R) Freon injection, BDC coupling to piston and ultrasound microphone adjustment.

As seen in Figure 9.9, the clean room area has a lot of LSBB maintenance equipment, so it is expected to have some electronic noise pick-up. The overall noise evaluation is shown in the frequency spectrum. Raw signal was acquired at maximum rate 300kS/s and full span of the ultrasound microphone. As seen, several peaks are noticeable from all sorts of sources. Nevertheless, the intent was to observe the BDC's performance, register events and acquire any information if possible. The noise level throughout the trials was 7.56 ± 1.43 mV.
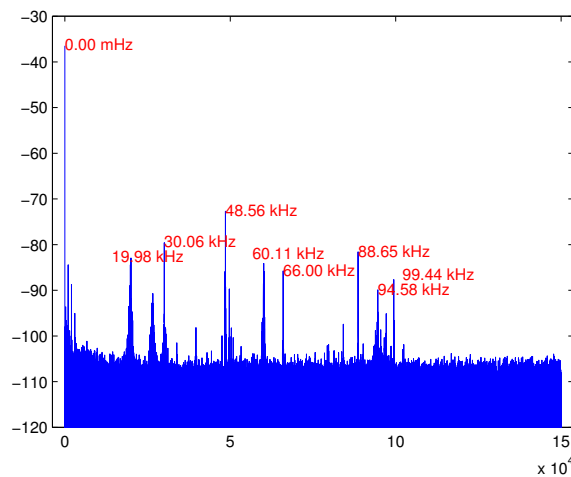
Figure 9.9: noise frequency spectrum.

Several nucleations events at different pressures were registered throughout the initial prototype SIMPLE BDC response. The investigation of the prototype BDC was performed at LSBB room temperature 16.0 ± 0.1ºC. The first event registered was at 5 bar. As shown in Figure 9.10, the event possesses a pulse shape similar to the true nucleation events from a SDD. This is even more obvious when the spike is zoomed. The recompression was a success, ~ 1 second. Here, the noise level rise (~25%) is perfectly observable. Once the event occurs, the recompression from the piston base system started and can clearly be seen. As all the apparatus was near each other, this is visible; in the future the recompression system must be isolated from the chamber.
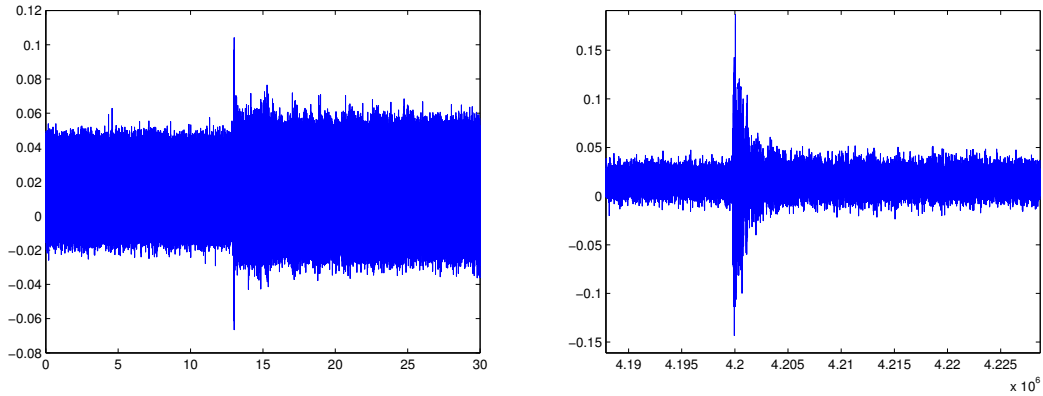
Figure 9.10: (L>R) nucleation event, zoom of the event in the left.

The frequency of the isolated event is shown in Figure 9.11. Surprisingly, the event possesses a primary frequency ~ 13 kHz, significantly different from those reported by COUPP [27]. Although the BDC is strictly-speaking a bubble chamber, its differences with the classic bubble chamber are probably significant in this aspect, the observed much lower frequency most likely due to the gel and glycerin surrounding the big droplet.
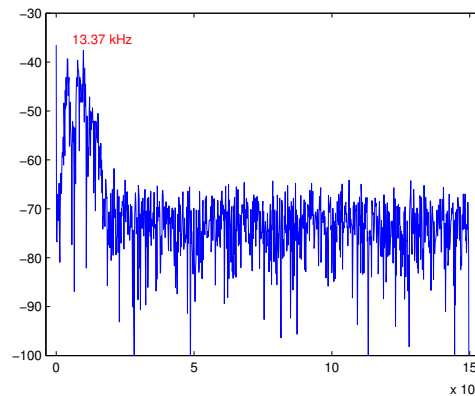
Figure 9.11: frequency spectrum of the nucleation event seen in Figure 9.10.

The time constant of the event is 0.32 ms, about ~ factor 100 less than events recorded in the SDD.

The following example of a nucleation event in the detector is shown in Figure 9.12, but this time occurred at a lower pressure (4 bar). As seen, the behavior, pulse shape and frequency spectrum remained the same as the previous events at 5 bar. The time constant of the decaying envelope was 0.23 ms.
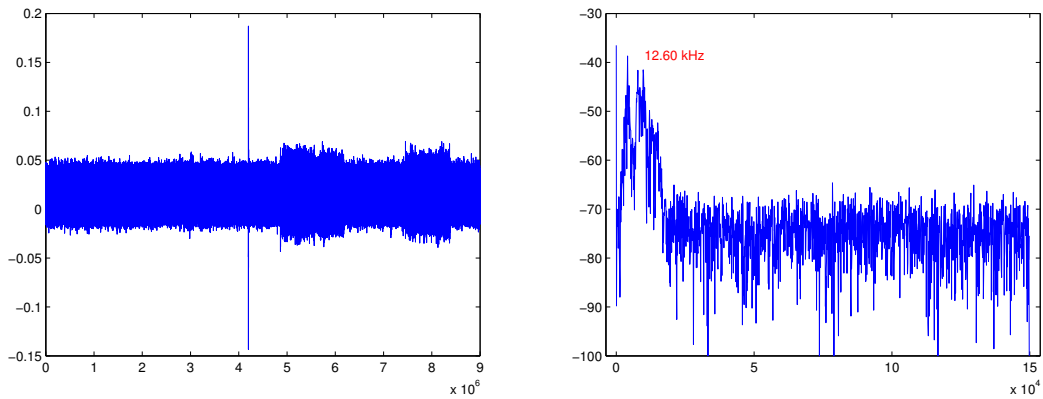
Figure 9.12: (L>R) nucleation event at 4 bar, and its FFT.

The last example of a nucleation event observed from the prototype bubble chamber is shown in Figure 9.13. The time constant of the event was 0.37 ms.
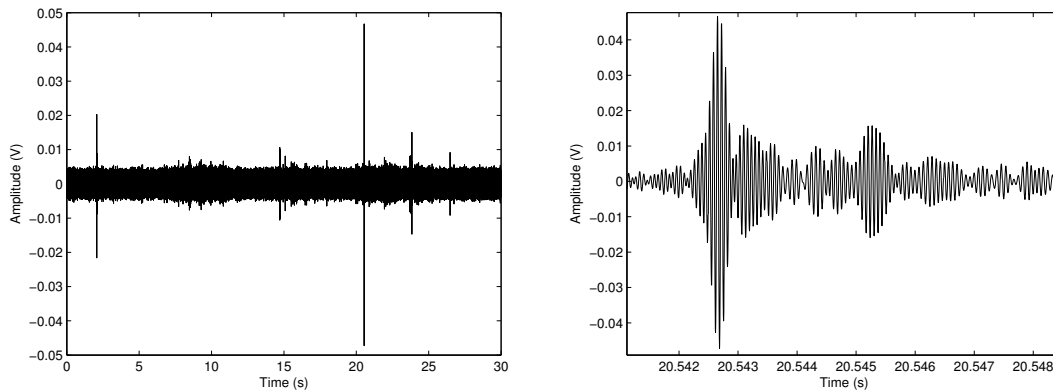
Figure 9.13: (L>R) nucleation event at 3 bar, zoom of the event in the left.

Several digital filters were applied to the data, sweeping the entire 10-150 kHz range of the ultrasound microphone. In this process, several regions of noise were eliminated but these preliminary results of the new SIMPLE BDC did not reveal any high nucleation frequency signals as reported by others [27], and attributed to proto-bubble formation. Nevertheless, the best filter implemented was a band-pass filter between 11-18 kHz guaranteeing the most optimal signal output. The frequency spectrum of the event is shown in Figure 9.14.
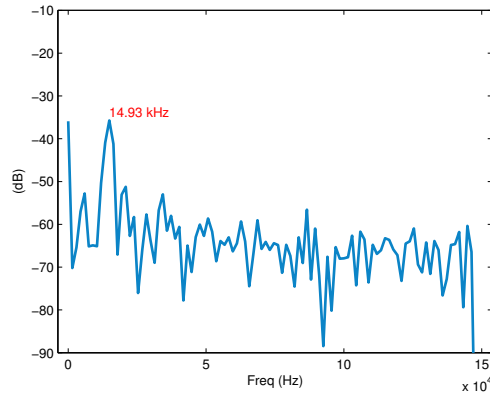
Figure 9.14: FFT of the nucleation event seen in Figure 9.13.

The overall nucleation frequency values of the events are 13.25 ± 1.76 kHz with time constants of 0.31 ± 0.05 ms

The BDC chamber prototype requires significant R&D prior its full implementation, in particular with respect to: a profound study of the glycerin-gel and gel-plastic barrier, noise evaluation, average time between nucleation events and establishment of neutron-α discrimination criteria comparable to Phase II.

Chapter 10 Conclusions and Future Work

_____

10.1 Conclusions

The experimental search for evidence of astroparticle dark matter has been a subject of intense international activity over the last decades. While the existence of dark matter is today well-established, its nature continues unknown and it remains often generically referred to as simply a WIMP (Weakly Interacting Massive Particle). The role of direct search experiments is its detection, from which its nature and properties may be studied.

One of the direct search techniques is the use of superheated liquids, which offers the advantage of an intrinsic insensitivity to the majority of particle backgrounds experienced in the more common techniques.

The instrumentation of superheated liquid detectors is generally acoustic. The implementation of a true microphone-based instrumentation, together with robust algorithms for the SDD identification, discrimination and validation filters and analysis of a bubble nucleation events, provides a means of discriminating nuclear recoil events from acoustic backgrounds associated with the gel dynamics and environmental noise, as well as α events.

In general, no significant variations in the instrumentation output were observed under the range of temperature and pressure conditions in which the SDDs are customarily applied, beyond signal frequency shifts that may be related to the gel as it approaches its melting point.

A new approach was explored: spatial localization of each event. This served three purposes: to corroborate the data of the nucleation detection; to make easier the identification of a phantom; and to determine the spatial density of the nucleations and through it the incidence of the energy source. The experimental results are encouraging, yielding errors close to the mesh resolution. To improve the resolution and extend the results to 3D, a new heating probe design is required. A more complete model for sound propagation within the hydrogenated gel is also required, since the velocity was measured in gel and not gel+droplet suspension, together with inclusion of glass reflections, the temperature dependence of the sound speed, and finer mesh resolution.

The response of SDDs to variations in the standard chemistry of their fabrication which have impact on both the acoustic source and propagation medium, as well as on the SDD lifetime. The results are in general agreement with what might be expected from considerations of both the bubble nucleation and gel medium properties, and show that normal small fabrication variations have a relatively small influence on detector performance. In terms of detector design, a device providing a temperature-independent amplitude, fast-falling signal pulse with an essentially constant primary response frequency is to be desired. With these criteria, the results suggest that SDD fabrications other than the standard one are not to be preferred, although minor alterations can be consciously

made in order to achieve certain particular results. The storage of detectors below 0ºC following fabrications is clearly to be avoided.

A new bubble nucleation efficiency was drawn out and particle discrimination confirmed and determined throughout *α-n* calibrations. These series of measurements using calibrated α and neutron irradiations confirmed the ability of the standard SIMPLE SDD to distinguish both event types acoustically. The droplet size distribution provides a natural lower cutoff to the α dE/dx, and is responsible both for the amplitude gap between the α and neutron populations, and the spectral asymmetry in the α power distribution. When varying one or more of any parameter (gel, droplet size, stiffness, concentration, refrigerant, temperature, pressure, etc) of the SDD fabrication protocol it is clear that the distinct particle discrimination can be lost.

The final results of the Phase II SIMPLE measurements, comprising two run stages of 15 superheated droplet detectors each overlapped for the first time results previously obtained only indirectly, and provide the current most sensitive limits against a spin-dependent WIMP-proton interaction. In the spin-independent sector, the exclusion contour challenges a significant part of the light mass WIMP region of current interest.

11.2 Future Work

This thesis presents an advanced SDD instrumentation and methods for identification and signal discrimination of true bubble nucleation events. The spatial identification results presented in this work clearly have room for improvement, especially regarding a better model for sound propagation within the hydrogenated gel and glass reflections, the temperature dependence of the sound speed, and finer mesh resolution. The technique also needs further validation of phantom suppression and a better understanding of the spatial distribution of the nucleations.

Restrictions on the applications of these SIMPLE SDDs beyond dark matter searches should be eliminated. The instrumentation and techniques investigated in this work can be carried over to new approaches to an industry solution for alpha contamination assays in ultra-low activity-grade Integrated Circuits.

With regard to background discrimination, there is at least one open issue to be investigated: the detection of the 3rd stage of bubble nucleation associated with the proto-bubble formation, which depends on the nature of the incident radiation. Given that this stage is fast, ultrasound techniques now obtained can be implemented to the SDDs.

Insofar as dark matter searches are concerned, the new SIMPLE approach – the *big droplet chamber* - has recently been introduced towards addressing the problem of the low 1-2% active mass concentration of the SDDs. The physics underlying their functioning is identical, although BCs must be recompressed following each bubble nucleation. Detection of the nucleation events in this case might be accomplished using both acoustic and optical techniques such as developed herein for only the acoustic, and requires significant R&D before its full implementation.

On a more broader perspective on the future, SIMPLE's Phase III is envisioned to increase its sensitivity levels in the two search sectors with exposures by initially using two 5 kg BDCs. Assuming the same particle-induced event discrimination as in Phase II with zero candidate events, it is expected to provide more than a factor 10 improvement in current results as seen in Figure 10.1.
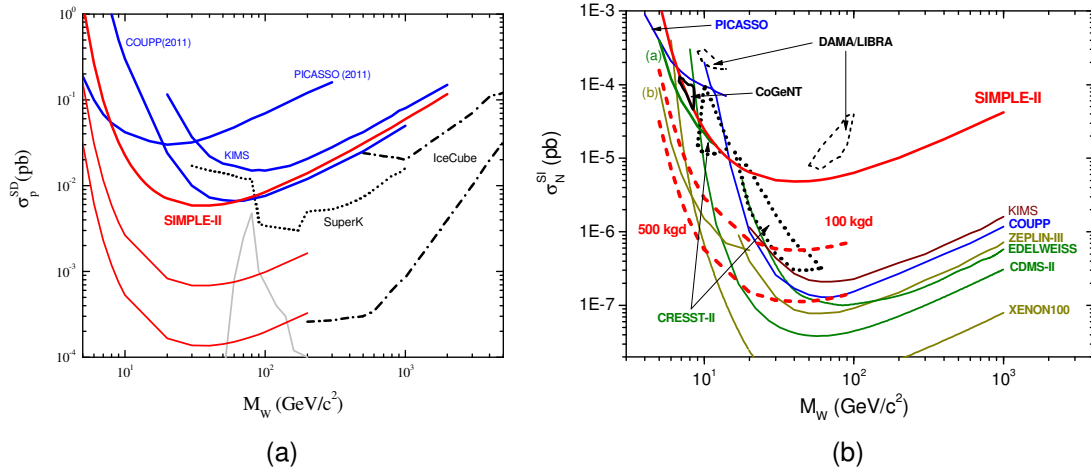

Figure 10.1: current results and Phase III sensitivity levels in the spin-dependent (a) and spin-independent (b) sectors.

References

_____

[1] T.A. Girard, et al., Physics Letters B 621 (2005) 233-238.

[2] G. Bertone, Particle Dark Matter (Cambridge University Press, 2010).

[3] G. Bertone, et al., Phys. Rep. 405, 279 (2005).

[4] B. Paczynski, Astrophys. J. 304, 1 (1986); K. Griest, Astrophys. J. 366, 412 (1991).

[5] F. De Paolis et al., Phys. Rev. Lett. 74, 14 (1995).

[6] K. Zioutas *et al.* CAST Collaboration Phys. Rev. Lett. 94, 121301 (2005).

[7] DAMA/LIBRA http://people.roma2.infn.it/~dama/web/home.html

[8] KIMS http://q2c.snu.ac.kr/KIMS/KIMS index.htm

[9] CDMS http://cdms.berkeley.edu/

[10] EDELWEISS http://edelweiss.in2p3.fr/

[11] CREST http://www.cresst.de/darkmatter.php

[12] COGENT http://cogent.pnnl.gov/

[13] XENON http://xenon.astro.columbia.edu/

[14] ZEPLIN http://www.hep.ph.ic.ac.uk/ZEPLIN-III-Project/

[15] COUPP http://www-coupp.fnal.gov/

[16] PICASSO http://www.picassoexperiment.ca/dm.php

[17] SIMPLE http://sites.google.com/site/dm2011simple/

[18] R. Bernabei et al., Eur. Phys. J. C67, 39 (2010).

[19] S.K. Kim: talk at TAUP-2011 Workshop, Munich, Germany, Sept. 5-9, (2011).

[20] C.E. Aalseth et al., Phys. Rev. Lett. 106, 131301 (2011).

[21] Z. Ahmed et al., Science 327, 1619 (2010); Z. Ahmed et al., Phys. Rev. Lett. 06, 131302 (2011).

[22] E. Armengaud et al., Phys. Lett. B702, 329 (2011).

[23] Z. Ahmed et al., Phys. Rev. 84, 011102 (2011).

[24] G. Angloher et al., arXiv:1109.0702 [astro-ph.CO].

[25] E. Aprile et al., arXiv:1104.2549, [astro-ph.CO].

[26] V.N. Lebedenko et. al., Phys. Rev. D80, 052010 (2009).

[27] E. Behnke et al., Phys. Rev. Lett. 106, 021303 (2011).

[28] S. Archambault et al., Phys. Lett. B682, 185 (2009).

[29] M. Felizardo et al., Phys. Rev. Lett. 108, 201302 (2012).

[30] R. Abbasi et al., Phys. Rev. Lett. 102, 201302 (2009).

[31] AMANDA http://amanda.uci.edu/

[32] ANTARES http://antares.in2p3.fr/

[33] S. Desai et al., Phys. Rev. D70, 083523 (2004).

[34] D'Errico F., et al., Nucl. Instrum. Methods. A 505 (2003) 50-53.

[35] D'Errico, F., Nucl. Instrum. Methods. B 184 (2001) 229-254.

[36] Roy, B. et al., Radiat. Phys. Chem. 61 (2001) 509-510.

[37] Seitz, F., Phys. Fluids 1 (1958) 2-13.

[38] Skripov, V.P., New York, John Wiley & Sons (1974).

[39] Bell, C.R., et al., Nucl. Sci. Eng. 53 (1974) 458-465.

[40] Sun, Y.Y., et al., J. Comp. Phys. 103 (1992) 116-140.

[41] Apfel, R.E., et al., Phys. Rev. A 31 (1985) 3194-3198.

[42] D'Errico, F., Radiat. Prot. Dosim. 84 (1999) 55-62.

[43] Apfel, R.E., Roy, S.C., Nucl. Instrum. Methods. 219 (1984) 582-587.

[44] Apfel, R.E., Lo, Y.-C., Health Physics 56 (1989) 79-83.

[45] Mala Das et al, Nucl. Instrum. Methods. A 543 (2005) 570-576.

[46] L. Hamel, et al., Nucl Instrum. & Methods A 388 (1997) 91.

[47] d'Errico, F. et al, Radiat. Prot. Dosim. 61 (1995) 159-162.

[48] Ing, H., et al., Radiat. Meas. 27 (1997) 1-11.

[49] Das, Mala et al., Nucl. Instrum. Methods. A 452 (2000) 273-279.

[50] d'Errico, F., Alberts, W.G., Radiat. Prot. Dosim. 54 (1994) 357-360.

[51] d'Errico et al., Nucl. Instrum. Methods. A 476 (2002) 113-118.

[52] d'Errico, et al., Nucl. Instrum. Methods. A 476 (2002) 277-290.

[53] Sawamura, T et al., Nucl. Instrum. Methoda. A 505 (2003) 29-32.

[54] S.-L Guo et al., Radiation Measurements 31 (1999) 167-172.

[55] S.-L Guo et al., Radiation Measurements 34 (2001) 269-272.

[56] S.-L Guo et al., Radiation Measurements 36 (2003) 183-187.

[57] D'Errico, Nucl. Instrum. Methods. B 184 (2001) 229-254.

[58] Collar, J. I., et al., Phys. Rev. Lett. 85, 3083-3086 (2000).

[59] Collar, J. I., et al., New Journ. Phys. 2, 14.1-14.14 (2000).

[60] LSBB - Laboratoire Souterrain Bas Bruit de Rustrel Pays-d'Apt: http://lsbb.oca.fr; an electromagnetically shielded underground laboratory 60 km east of Avignon. The main experimental area at 1500 mwe constitutes a Faraday cage isolated from mechanical vibrations: the shielding reduces the magnetic field to less than 6 µT, with a long time stability of better than 20 nT and fluctuations below 2.5 fTpHz. The radioactivity of the rock due to 136Cs is less than 0.437 Bq; to 226Ra, less than 0.645 Bq, with a radon average of 50 Bq/m^3.

[61] Donald A. Glaser, Physical Review 87 (4): 665–665 (1952).

[62] R.E. Apfel and S.C. Roy, Rev. Sci. Instrum., 54(10), 1397-1400 (1983).

[63] Panasonic MCE-200 data specs: http://monacor.no/go/?p=MCE-200

[64] Texas Instruments PGA2500 data specs: http://www.ti.com/

[65] M. Felizardo, et al., Nucl. Instrum. Methods A, 585 (2008) 61.

[66] J.I. Collar, et al., New Journ. Phys. 2 (2000) 14.1.

[67] F. d'Errico, Nucl. Instrum. Methods B184 (2001) 229.

[68] F. Giuliani, et al., Nucl. Instrum. Methods A 526 (2004) 348.

[69] C. H. Knapp and G. C. Carter, IEEE Trans. on Acoustics, Speech and Signal Processing, vol. 24, no. 4, 320 (1976).

[70] J. C. Chen, et al, IEEE Transactions of Signal Processing, vol. 50, no. 8, (2002).

[71] B. B. Hubbard, The World According to Wavelets: The story of a Mathematical Technique in the Making (A. K. Peters, London, 1998).

[72] L. R. Rabiner, B. Gold, Theory and Application of Digital Signal Processing (Englewood Cliffs, Prentice-Hall, 1975).

[73] G. Waysand, private communication.

[74] F. Giuliani, et al., Nucl. Instrum. Methods A526 (2004) 348.

[75] M.I. Prudêncio, et al., Journal of Archaeological Science (2011), doi:10.1016/j.jas.2011.11.010.

[76] R.Sarkar, et al.: Rad. Phys. & Chem. 71 (2004) 735.

[77] T. Morlat, et al.: Nucl. Instrum. Meth. A560 (2006) 339.

[78] T. Morlat, PhD thesis, University of Paris 6, 2004 (unpublished).

[79] J. Puibasset, PhD thesis, University of Paris 6, 2000 (unpublished).

[80] C. Joly-Duhamel, et al.: Langmuir 18 (2002) 7158.

[81] J.I. Collar, et. al.: New Journ. Phys. 2 (2000) 14.1.

[82] M. Felizardo, et.al.: Nucl. Instrum. Meth. A599 (2009) 93.

[83] F Aubin, et. al.: New Journ. Phys. 10 (2008) 103017.

[84] F. d'Errico: Nucl. Instr. & Meth. vol. B184 (1-2). pp. 229-254. 2001.

[85] J.I. Collar, et al.: New Journ. Phys. 2 (2000) 14.1.

[86] D'Errico: Nucl. Instrum. Methods. B 184 (2001) 229-254.

[87] F. Giuliani, et al.: Nucl. Instrum. Methods A 526 (2004) 348.

[88] R. E. Apfel et al.: Rev. Sci. Instrum. 54, 1397 (1983).

[89] R. E. Apfel et al.: Phys. Rev. A 31, 3194 (1985).

[90] D'Errico: Nucl. Instrum. Methods. B 184 (2001) 229-254.

[91] G. Heusser, Nucl. Instr. and Meth. A 369 (1996) 539.

[92] G.V. Gorshov et al., Sov. J. Nucl. Phys. 13 (1971) 450.

[93] J.I. Collar, et al.: Proceedings of the First International Workshop on the Identification of Dark Matter (IDM96). Sheffield, UK, World Scientific, Singapore, 1996.

[94] G. Waysand et al., Nucl. Instrum. Methods Phys. Res., Sect. A 444, 336 (2000).

[95] J. Amare et al., J. Phys. Conf. Ser. 39, 151 (2006).

[96] V. Chazal et al., Astropart. Phys. 9, 163 (1998).

[97] H. Wulandari et al., Astropart. Phys. 22, 313 (2004).

[98] F. Giuliani et al.: Nuclear Physics B (Proc. Suppl.) 173 (2007) 129–132.

[99] M. Felizardo et al., Nucl. Instrum. Methods Phys. Res., Sect. A 589, 72 (2008).

[100] T. Morlat et. al.: Astrop. Phys. 30, 159 (2008).

[101] Y. C. Lo, R. E. Apfel: Phys. Rev. A38, 5260 (1988).

[102] M. Barnabé-Heider et. al., Nucl. Instr. & Meth. 555, 184 (2005).

[103] M. Felizardo et. al., Phys. Rev. Lett. 105, 211301 (2010).

[104] V. Zacek: talk at TAUP-2011 Workshop, Munich, Germany, Sept. 5-9, 2011.

[105] W.H. Lippincott: talk at TAUP-2011 Workshop, Munich, Germany, Sept. 5-9, 2011.

[106] S.K. Kim: talk at TAUP-2011 Workshop, Munich, Germany, Sept. 5-9, 2011.

[107] S. Desai et. al., Phys. Rev. D70, 083523 (2004).

[108] R. Abbasi et. al., Phys. Rev. Lett. 102, 201302 (2009).

[109] G. J. Feldman, R. D. Cousins: Phys. Rev. D57, 3873 (1998).

[110] L. Roszkowski et. al., J. High Energy Phys 07, 075 (2007).

[111] J. D. Lewin and P. F. Smith, Astrop. Phys. 6, 87(1996).

[112] A. F. Pacheco and D. Strottman, Phys. Rev. D40, 2131(1989).

[113] F. Giuliani and TA Girard, Phys. Rev. D71, 123503(2005).

[114] J. Angle et. al., Phys. Rev. Lett. 100, 021303 (2008).

[115] J. Angle et. al., arxiv:1104.3088v1 [astro-ph.CO].

[116] E. Aprile et. al., arxiv:1104.2549v1 [astro-ph.CO].

[117] Z. Ahmed et. al., Science 327, 1619 (2010).

[118] Z. Ahmed et. al., Phys. Rev. Lett. 106, 131302 (2011).

[119] V.N. Lebedenko et. al., Phys. Rev. D80, 052010 (2009).

[120] E. Armengaud et. al., Phys. Lett. B687, 294 (2010).

[121] S. Archambault et. al., arXiv:1202.1240v1 [hep-ex].

[122] G. Angloher et. al., arXiv:1109.0702v1 [astro-ph.CO].

[123] C. Savage et. al., JCAP 0904, 010 (2009).

[124] C.E. Aalseth et. al., Phys. Rev. Lett. 106, 131301 (2011).

[125] J.I. Collar: arxiv:1106.0653v1 [astro-ph.CO]. (2011).

[126] J.I. Collar: arxiv:1103.3481v1 [astro-ph.CO]. (2011).

[127] Yu.N. Martynyuk and N.S. Smirnov: Sov. Phys. Acoust. 37 (1991) 376.

[128] MS Plesset and SA Zwick: J. Appl. Phys. 23 (1952) 95.

[129] M. Felizardo, et.al.: Nucl. Instrum. & Meth. A614 (2010) 278.

[130] http://www.avisoft.com/